

A New Upper Limit for the Tau-Neutrino Magnetic Moment

Reinhard Heinrich Schwienhorst

May 2000

Supported in part by:

The Department of Energy

School of Physics and Astronomy

Tate Laboratory of Physics

116 Church Street S.E.

Minneapolis, MN 55455

A New Upper Limit for the Tau-Neutrino Magnetic Moment

A THESIS

SUBMITTED TO THE FACULTY OF THE GRADUATE SCHOOL
OF THE UNIVERSITY OF MINNESOTA

BY

Reinhard Heinrich Schwienhorst

IN PARTIAL FULFILLMENT OF THE REQUIREMENTS
FOR THE DEGREE OF
DOCTOR OF PHILOSOPHY

Professor Roger Rusack, Adviser

May, 2000

© Reinhard Heinrich Schwienhorst 2000

A New Upper Limit for the Tau-Neutrino Magnetic Moment

by Reinhard Heinrich Schwienhorst

Under the supervision of Professor R. Rusack

Abstract

The tau-neutrino enriched neutrino beam in the Fermilab experiment E872 (DONUT) provides a unique opportunity to study tau neutrino properties. A non-vanishing tau-neutrino magnetic moment is consistent with the recent observation of neutrino mass and gives rise to electromagnetic interactions between neutrinos and charged particles. The resulting increase in the neutrino-electron scattering cross-section can be detected experimentally.

This thesis presents a search for an excess of neutrino-electron scattering events in the DONUT data set. The analysis of 6,000,000 recorded triggers yielded two candidate events with 4.4 expected background events from Standard Model processes. No evidence for non-Standard Model interactions has therefore been found, and the new upper limit for the tau-neutrino magnetic moment is $\mu_{\nu_\tau} \leq 4.2 \times 10^{-7} \mu_B$.

Acknowledgments

Many people have supported me during the completion of this thesis and naming them all would fill a book. First and foremost, my wife Jan has been very supportive of me during my years in graduate school. She encouraged me when I couldn't see the light at the end of the tunnel and she filled my life with many beautiful things outside of Physics.

My advisor Roger Rusack has given me a lot of input and guidance in writing this thesis. I am grateful for his many suggestions and his patience and encouragement while I was learning the details of the English language. He has also given me the freedom to pursue my own research goals and provided me with the tools to achieve them.

Experiments of this magnitude can never be accomplished by one person alone and I am grateful to the DONUT collaboration for allowing me to join them when the data run was almost over. I would like to thank Byron Lundberg and Gina Rameika in particular because they have helped me get my research started and they have guided me through the analysis process. I would also like to thank Jason Sielaff and Carolyn Erickson who I have had many discussions with at the University of Minnesota. Both have always had time to answer my questions. I would furthermore like to thank Ken Heller for his suggestions and ideas that have helped me in the data analysis.

Before joining DONUT, I gained a lot of experience by working on the MINOS experiment, and I would like to thank Keith Ruddick for guiding me through my first steps of research in experimental Physics.

Meinen Eltern möchte ich für Ihre andauernde Unterstützung danken. Ohne ihre Hilfe hätte ich nicht Physik studieren können und wäre auch nicht in die USA gekommen. Sie haben mir ermöglicht, meine Träume zu erfüllen.

Dedication

This thesis is dedicated to my wife, Jan.

Table of Contents

Abstract	i
Acknowledgments	ii
Dedication	iii
List of Figures	vii
List of Tables	xii
Chapter 1 Introduction	1
Chapter 2 Phenomenology	3
2.1 Neutrinos in the Standard Model	3
2.2 Extensions to the Standard Model	5
The Neutrino Magnetic Moment	6
2.3 Neutrino Interactions	10
Chapter 3 Experimental Setup	15
3.1 The Neutrino Beam	15
3.2 The Emulsion Target	18
3.3 The Spectrometer	20
The Trigger Counters	23
The Scintillating Fiber Tracking System	24
Downstream Tracking	28
The Electromagnetic Calorimeter	29
Muon Identification	30
Alignment	30
Data Acquisition	32
Chapter 4 Analysis	33
4.1 The Hardware Event Selection	33
4.2 The Data Set	35
The Data Periods	35
4.3 Event Reconstruction	36
The Scintillating Fiber System	36
Downstream Tracking	38
4.4 The Neutrino Data Filter	39
Software Neutrino Event Selection	39
Interactive Event Selection	39
Vertex Prediction	40
4.5 The Emulsion Data Analysis	41
Emulsion Scanning	41

Emulsion Analysis	42
4.6 Magnetic Moment Event Selection	42
Step One.	49
Step Two	54
Step Three	61
Step Four	70
Step Five	73
Chapter 5 Simulation.	81
5.1 The Neutrino Event Generator.	81
5.2 Neutrino Interactions	82
5.3 The Hybrid Emulsion Spectrometer Simulation	83
The Emulsion Targets	83
The Scintillating Fiber Tracker	83
Downstream Tracking	83
The Electromagnetic Calorimeter	84
5.4 Calibration of the Monte Carlo	84
5.5 Monte Carlo Results	85
Magnetic Moment Interactions	85
Neutrino-Nucleon Interactions.	92
The Selection Uncertainty	99
Chapter 6 Results.	100
6.1 The Candidate Events	101
6.2 Calculation of the Magnetic Moment	104
The Magnetic Moment.	104
The Total Cross Section.	105
Event Selection	105
Background Correction	106
6.3 Collection of Experimental Parameters.	106
The Event Selection Efficiency	106
The Expected Number of Background Events.	107
The Neutrino Flux	107
6.4 Statistical Analysis.	108
The Strict Classical Evaluation	109
Including Systematic Uncertainties	113
6.5 Analysis of Visually Selected Events	116
The Candidate Events	117
The Number of Background Events	120
Statistical Analysis.	121
Chapter 7 Conclusions.	122
Appendix A Neutrino Beam	124

A.1	The D Production Cross Section	124
A.2	The D_s Production Cross Section	132
A.3	The Nuclear Dependence of the Production Cross Section	135
A.4	The xF and pT Dependence of the Production Cross Section	136
A.5	The D Decay	143
A.6	The D_s Decay	144
A.7	The Tau Decay	146
A.8	Prompt Neutrino Rates	147
A.9	The Target Acceptance	148
A.10	The Interaction Probability	149
A.11	Other Sources of Neutrinos	151
	Other Sources of Prompt Neutrinos	151
	Nonprompt Neutrinos	152
A.12	The Expected Number of Interactions	152
A.13	Neutrino-Flux Check	154
Appendix B The Control Events		157
B.1	The Event samples	157
	Muon Neutrino Charged Current Interactions	158
	Electromagnetic Showers Produced by Muons	158
B.2	Comparison between Data and Monte Carlo	161
Bibliography		163

List of Figures

Figure 2-1. Magnetic moment interaction vertex of an electron and a neutrino. Which particles participate in the neutrino loop depends on the model, in this example leptons and gauge bosons j comprise the loop.	8
Figure 2-2. Feynman diagram showing two weak interactions of neutrinos (ν) with an electron (e). The left hand side shows a charged-current interaction (exchange of a W boson); the right-hand side shows a neutral-current interaction (exchange of a Z boson).	10
Figure 2-3. Feynman diagram of a neutrino-electron magnetic moment interaction. The arrow next to a particle symbol represents the helicity.	11
Figure 2-4. Differential cross section for neutrino-electron scattering. The dashed line shows the y -dependence due to a magnetic moment of μ . The solid line shows the differential cross section for neutrino-electron neutral-current scattering (σ_{NC} or σ_{CC}). A neutrino energy of 50 GeV was used to generate this plot.	13
Figure 3-1. Layout of the proton beam target. The proton beam is incident from the left.	16
Figure 3-2. Neutrino beam active and passive shielding. The proton beam target is located on the left. The first magnet is encased in concrete on the left. Most of the shielding surrounding the target is not shown.	17
Figure 3-3. Design of emulsion modules: bulk and ECC.	19
Figure 3-4. Emulsion target and scintillating fiber tracker configuration. Several planes of scintillating fibers were mounted downstream of each of the four target stations. The fiber planes were arranged in three different orientations and the six image intensifiers and readout CCD modules underneath the target region are not shown.	20
Figure 3-5. Plan view of the spectrometer.	21
Figure 3-6. Top view of the emulsion target region. The shield was also installed on top and on the side of the target region.	22
Figure 3-7. View of the target stand (on the right) and the upstream veto trigger wall (on the left). The lead shield in between the veto wall and the target stand is also shown. The large tubes at the bottom of the target stand are the enclosures for the image intensifier modules.	22
Figure 3-8. Front view of the fiber layout of two different planes. Different sections of the vertical plane are connected to different image intensifiers (IIT).	25
Figure 3-9. One readout module, consisting of four image intensifiers and a readout CCD module.	26
Figure 3-10. CCD image of the fiducial fibers. A dark pixel has a lot of charge, a white pixel a small charge.	28
Figure 3-11. Histogram of the angle and position projection error from the SF system to changeable sheet CS5. The top row shows the difference between track angle determined in the SF system and track angle determined in the emulsion. The angle difference has a sigma of 3.3 mrad. The bottom row shows the difference between the track position determined in the SF system projected to the Z position of the changeable sheet and the track position found in the changeable sheet. The difference between projection and emulsion track position has a sigma of 0.35 mm. The data are from a cosmic ray run and the smooth line is a Gaussian fit to the data.	31
Figure 4-1. Illustration of the adjacency requirement. The figure shows only the trigger counters from figure 3-6. Two charged particles pass through the T2 and T3 trigger planes. The two trigger hits at the bottom are not next to each other and do not form an adjacency. Only the two trigger hits at the top form an adjacency.	34
Figure 4-2. Histogram of the number of charged particle tracks per event that passed through an emulsion module without interacting. The two data sets were generated by the Monte Carlo simulation and passed the trigger and software neutrino event selection cuts.	44
Figure 4-3. Stacked histogram of the electron energy and the angle between incoming neutrino and outgoing electron for simulated electron-neutrino-nucleon charged-current interactions (light shade) and neutrino-electron magnetic moment interactions (dark shade). The frequency is shown on a log scale.	45
Figure 4-4. Projections from figure 4-3, i.e. comparison of energy and angle between the incoming neutrino and the scattered electron for simulated magnetic moment interactions (solid line) and simulated neutrino-nucleon charged-current interactions (dashed line).	46
Figure 4-5. Muon hits for reconstructed tracks for period 4 neutrino candidates.	50

Figure 4-6. Number of muon ID hits for reconstructed tracks for Monte Carlo muon neutrino charged-current interactions only.	51
Figure 4-7. Histogram of the average scintillating fiber signal per event in the data control sample of period four.	54
Figure 4-8. Distribution of reconstructed vertex positions in the remaining data events. The solid line shows the location of the 0.5m wide emulsion modules. The dashed line shows the cut region. A large square means a large number of vertices are at that location.	56
Figure 4-9. Illustration of a backward adjacency. The figure shows only the trigger counters from figure 3-6. Two charged particles pass through the T2 and T3 trigger planes. The hits are consistent with a particle shower that started downstream of T3.	57
Figure 4-10. View of the target region for an event in which the reconstructed electron track did not produce a shower downstream of the next emulsion module. The vertex is shown as a small box and the track is shown as a line starting at the vertex. Filled boxes depict trigger counters that were hit.	58
Figure 4-11. Bethe-Bloch formula for energy loss in plastic scintillator.	60
Figure 4-12. Number of events remaining in the four control samples after each of the step one and step two cuts. The two lower lines (triangles) are for control set one of ν_m charged-current interactions and the two upper lines (circles) are for control set two of electromagnetic showers. Each line starts at the number of events remaining after the software selection.	61
Figure 4-13. View of the target region for a background event in which many tracks are coming from the side (the bottom of the figure).	62
Figure 4-14. Two orthogonal views of a background event. The reconstructed vertex is shown as a small shaded box.	64
Figure 4-15. Two orthogonal views of a background event.	65
Figure 4-16. Example of a charged particle track crossing the readout end of a plane. The particle does not pass through the plane of opposite orientation.	66
Figure 4-17. Target region view of an event with no reconstructed tracks behind the next module downstream of the vertex, shown as a small shaded box.	67
Figure 4-18. Number of events remaining in the control samples after each of the step three cuts. The two lower lines (triangles) are for control set one of ν_m charged-current interactions and the two upper lines (circles) are for control set two of electromagnetic showers. Each line starts at the number of events remaining after step two.	69
Figure 4-19. Target region view of an event with a long particle track that was found in the interactive analysis (dark line).	70
Figure 4-20. Histogram of the normalized time difference between a hit in trigger plane T3 and a hit in trigger plane T1 for penetrating muons from the muon calibration file.	71
Figure 4-21. View of the target region for an event with a large pulseheight track (hits inside the oval) that was not reconstructed properly in the scintillating fiber planes. The box on the right-hand side shows a close-up view of the track hits.	73
Figure 4-22. View of the target region for an event with two reconstructed tracks connected to the vertex.	74
Figure 4-23. View of the target region for an event with two reconstructed tracks upstream of the interaction vertex.	75
Figure 4-24. View of the target region for an event with a single reconstructed charged particle track downstream of emulsion module four.	76
Figure 4-25. View of the target region and the downstream spectrometer elements for the event shown in figure 4-24.	76
Figure 4-26. Maximum angle of a vertex track for events with five or less vertex tracks for magnetic moment events (upper histogram) and neutral-current events (lower histogram) for Monte Carlo events in period four.	78
Figure 4-27. Target region view of an event with a reconstructed track connected to the vertex that passed through several emulsion modules.	79
Figure 4-28. Number of events remaining in the control samples after step four and each of the step five	

cuts. The two lower lines (triangles) are for control set one of ν_m charged-current interactions and the two upper lines (circles) are for control set two of electromagnetic showers. Each line starts at the number of events remaining after step three.	80
Figure 5-1. Typical simulated magnetic moment interaction. The left hand side shows a view of the entire spectrometer; the right hand side shows a close-up view of the target region.	82
Figure 5-2. Trigger, pass 1, and visual selection efficiency for neutrino-electron magnetic moment interactions. Each plot shows the fraction of events remaining after the cut, starting at one. The second mark shows the trigger efficiency, the third mark the software selection efficiency. The visual selection efficiency is given by the fourth point.	86
Figure 5-3. Distribution of electron energies for magnetic moment scattering. The solid histogram shows the spectrum of electron energies in neutrino-electron magnetic moment interactions. The shaded area shows the spectrum after trigger and software neutrino interaction selection.	87
Figure 5-4. Step one selection efficiency for neutrino-electron magnetic moment interactions. Each line shows the fraction of events remaining after each of the cuts in step one, sorted by run period and target module. Each line starts at the fraction of events that is in the software event selection file (continuation of the plot from figure 5-2). The second point shows the fraction remaining after the muon cut, the third point shows the fraction remaining after the calorimeter energy cut, the fourth point shows the fraction remaining after the hadron cut, the fifth point shows the fraction remaining after the vertex reconstruction cut, and the last point shows the fraction of events remaining after all of the step one cuts.	88
Figure 5-5. Step two selection efficiency for neutrino-electron magnetic moment interactions. Each plot shows the fraction of events remaining after the cut. The points show the fraction of events remaining after each of the cuts in step two. Each line starts at the fraction of events remaining after step one (each line is continued from figure 5-4). The second point shows the fraction of events remaining after the out-of-time cut, the third point shows the fraction remaining after the vertex location cut, the fourth and fifth points show the fraction remaining after the two trigger cuts, and the sixth point shows the fraction remaining after all of the pass two cuts.	89
Figure 5-6. Step three selection efficiency for neutrino-nucleon interactions. Each plot shows the fraction of events remaining after the cut. The points show the fraction of events remaining after each of the cuts in step three. Each line starts at the fraction of events remaining after step two (each line is continued from figure 5-5). The second point shows the fraction of events remaining after the vertex track cut, the third point shows the fraction remaining after the single view track cut, the fourth point shows the fraction remaining after the downstream track cut, and the fifth point shows the fraction remaining after all of the pass three cuts.	90
Figure 5-7. Histogram of the electron energy for magnetic moment events. The solid line shows the events selected by the neutrino interaction cuts (same as the shaded area in figure 5-3), the dashed line shows the energy distribution after the step three selection cuts.	91
Figure 5-8. Trigger, software, and visual selection efficiency for neutrino-nucleon interactions. Each plot shows the fraction of events remaining after the cut; each line starts at one. The second mark shows the trigger efficiency, the third mark the software selection efficiency. The visual selection efficiency is given by the fourth point. Each line shows the efficiency for one emulsion module; the legend is shown in figure 5-2.	93
Figure 5-9. Step one selection efficiency for neutrino-nucleon interactions. Each line shows the fraction of events remaining after each of the cuts in step one, sorted by run period and target module. Each line starts at the fraction of events that is in the software selection event file (continuation of the plot from figure 5-8). The second point shows the fraction remaining after the muon cut, the third point shows the fraction remaining after the calorimeter cut, the fourth point shows the fraction remaining after the hadron cut, the fifth point shows the fraction remaining after the vertex track cut, and the last point shows the fraction of events remaining after all of the step one cuts. Each line shows the efficiency for one emulsion module; the legend is shown in figure 5-2.	95
Figure 5-10. Step two selection efficiency for neutrino-nucleon interactions. Each plot shows the fraction of events remaining after the cut. The points show the fraction of events remaining after each of the cuts in step two. Each line starts at the fraction of events remaining after step one (each line is continued from figure 5-9). The second point shows the fraction of events remaining after the out-of-time cut, the third point shows the fraction remaining after the vertex location cut, the fourth and fifth points show the fraction remaining	

after the two trigger cuts, and the sixth point shows the fraction remaining after all of the pass two cuts. Each line shows the efficiency for one emulsion module; the legend is shown in figure 5-2.	96
Figure 5-11. Step three selection efficiency for neutrino-nucleon interactions. Each plot shows the fraction of events remaining after the cut. The points show the fraction of events remaining after each of the cuts in step three. Each line starts at the fraction of events remaining after step two (each line is continued from figure 5-10). The second point shows the fraction of events remaining after the vertex track cut, the third point shows the fraction remaining after the single view track cut, the fourth point shows the fraction remaining after the downstream track cut, and the fifth point shows the fraction remaining after all of the pass three cuts. Each line shows the efficiency for one emulsion module; the legend is shown in figure 5-2.	97
Figure 6-1. Three view of the first magnetic moment candidate event (run 3138, event 7918). Each dark line corresponds to a reconstructed track. The size of a hit in the SF planes indicates its pulseheight.	101
Figure 6-2. Three view of the second candidate event (run 3273, event 10082). Each dark line corresponds to a final track. The size of a hit in the SF planes is proportional to the fiber light signal.	103
Figure 6-3. Confidence belt for equation 6-10 with $n_{bg}=4.4$. Each horizontal line corresponds to an acceptance interval.	110
Figure 6-4. Probability distribution from equation 6-13 for α and β . The stars show α , the triangles show β , and the squares show R	112
Figure 6-5. Posterior pdf from equation 6-15 for α	116
Figure 6-6. Three views of the first candidate event (run 2907, event 12929) in the visually selected sample. Each dark line corresponds to a final track. The size of a hit in the SF planes indicates its pulseheight.	117
Figure 6-7. Same as figure 6-6 for the second candidate event (run 3024, event 11173) of the visually selected event sample.	118
Figure 6-8. Same as figure 6-6 for the third candidate event (run 3138, event 3097) in the visually selected event sample.	119
Figure 6-9. Same as figure 6-6 for the fourth candidate event (run 3273, event 10082) in the visually selected event sample.	120
Figure A-1. $\sigma_{\pi\pi}$ production cross section for several different energies. The QCD prediction is from reference [68]. The theoretical error band is an underestimate of the actual theoretical uncertainty. It is obtained by varying the normalization scale [74].	127
Figure A-2. Same as figure A-1, but for σ_{pp} production cross section. The prediction from data is explained in the text.	128
Figure A-3. Ratio of the production cross sections for $\pi\pi$ and pp	129
Figure A-4. J/ψ production cross section for pion and proton beams.	131
Figure A-5. Measured $\sigma_{\pi\pi}/\sigma_{pp}$ production cross section ratio from various experiments. The kaon data was not used to calculate the mean.	132
Figure A-6. $\sigma_{\pi\pi}/\sigma_{pp}$ production cross section ratio from various experiments. The kaon data was not used to calculate the mean.	133
Figure A-7. $\sigma_{\pi\pi}$ production cross section for a proton beam of 800GeV. The $\sigma_{\pi\pi}$ value was found using only the experimental data for $\pi\pi$ production, the σ_{pp} value was found using the predicted value for $\pi\pi$ production from data.	134
Figure A-8. $\sigma_{\pi\pi}$ production cross section for a pion beam of 800GeV.	135
Figure A-9. $\sigma_{\pi\pi}$ and σ_{pp} dependence of the differential cross section for charm production. The solid line is from a Pythia Monte Carlo run, the dashed line is from equation A-5 with $n=4.5$ and $b=0.86$. The data points are from experiment WA 92 [70].	138
Figure A-10. Parameter n from equation A-5 versus beam energy for several different fixed target charm production experiments. The NLO QCD calculation is given by the short dashes. The solid line is the Pythia calculation for charm quarks. The dashed line on the right hand side of the figure shows the variation in n when the charm quark mass is changed between 1.2GeV and 1.8GeV in the Pythia calculation.	139
Figure A-11. Same as figure A-10, but for the parameter b	140
Figure A-12. Same as figure A-10. The lines show results for a Pythia calculation. The solid line shows the Pythia result for $\pi\pi$ and pp production. The long dashes are for $\pi\pi$ production. The short dashes give the result for a pion beam. The proton mean is explained in the text. The pion data points have been corrected for different	

fit intervals in	141
Figure A-13. Same as figure A-12 for the parameter b . The data points have been adjusted for different intervals.	142
Figure A-14. Feynman diagram for the leptonic decay. l stands for tau, muon, or electron.	144
Figure A-15. Energy dependence of the kinematic factor KF from equation A-8 [100]. The solid line shows K_F for neutrinos; the dashed line shows KF for anti-neutrinos.	150
Figure A-16. Interacted prompt neutrino spectrum.	151
Figure A-17. Number of neutrino interaction events with a muon identified in the muon ID. Comparison of data and Monte Carlo.	155
Figure B-1. Histogram of the electromagnetic energy of knock-on electron events selected from muons passing through the spectrometer.	160
Figure B-2. Plot of the fraction of events removed from control sample one by each of the magnetic moment selection cuts. In the step one cuts, the first point is for the muon identification, the second point for the electromagnetic energy, the third point for vertex tracks, and the fourth point for non-showering tracks. In the step two cuts, the first point is for out-of-time events, the second point for vertex location, the third point for backwards triggers, the fourth point for trigger hits, and the fifth point for slow hadrons. In the step three cuts, the first point is for tracks from the side, the second point is for tracks in one view, the third point is for downstream tracks, and the fourth point is for track angles. In the step five cuts, the first point is for slow hadrons, the second point for shower development, the third point for upstream tracks, the fourth point for single tracks, the fifth point for the shower profile, and the sixth point for non-showering tracks. The error bar next to the figure shows the typical statistical uncertainty in the data.	161
Figure B-3. Same as figure B-2 for the second control sample of electromagnetic showers.	162

List of Tables

Table 2-1. Current experimental limits for neutrino properties from reference [14].	4
Table 4-1. Number of protons on target, number of changeable sheets, and total target mass for all four target configurations. The target mass includes 292kg for the upstream lead veto wall.	35
Table 4-2. Target configuration and module mass. ECC modules had only ECC type emulsion and bulk module had only bulk type emulsion, see section 3.2. E/B modules had ECC type emulsion in the upstream part of the module and bulk type emulsion in the downstream part of the emulsion.	36
Table 5-1. Effect of step five cuts on tau neutrino-electron magnetic moment interactions in the four run periods. The cuts were done in series; events removed by the first cut were not analyzed with the second cut anymore. The last column shows the fraction of events that passed all of the cuts.	92
Table 5-2. Number of neutrino-nucleon Monte Carlo interactions after visual selection in step four, sorted by event type.	98
Table 5-3. Number of Monte Carlo neutrino-nucleon interactions remaining after step five, sorted by event type.	98
Table 6-1. Number of events remaining after each of the selection cuts. The cuts from step three and four were not applied to the visual selection data.	100
Table 6-2. Event selection efficiency E for all target stations and run periods. The different target configurations and neutrino fluxes have been taken into account.	106
Table 6-3. Number of Monte Carlo neutrino-nucleon interactions remaining after step five.	107
Table 6-4. Neutrino flux for the four run periods. The flux for all periods is averaged over the four periods, weighted by the total target mass in each period.	108
Table 6-5. Sources of systematic uncertainty.	114
Table A-1. Fixed target open charm production data. The cross section is given for the parameter range in the “condition” column. The variable is explained in section A.4.	124
Table A-2. Experimental values for the parameter from equation A-2.	136
Table A-3. Average fit parameters for 800GeV beams. The last row is obtained by multiplying the pion number by the ratio of the Pythia predictions for protons and pions at 800GeV.	143
Table A-4. decay modes that include a neutrino in the final state [14].	143
Table A-5. decay modes that include a neutrino in the final state [14].	144
Table A-6. decay constant measurements.	145
Table A-7. Tau decay modes that include an electron- or muon-neutrino in the final state [14].	146
Table A-8. Semileptonic τ branching ratios [14].	146
Table A-9. Target acceptance and interacted neutrino energy for the different neutrino types.	149
Table A-10. Number of charged current neutrino interactions from prompt neutrinos. The average neutrino energy is weighted by the energy.	150
Table A-11. Number of expected prompt electron-neutrino charged-current interactions.	153
Table A-12. Number of expected prompt muon-neutrino charged-current interactions.	153
Table A-13. Number of expected prompt tau-neutrino charged-current interactions.	153
Table A-14. Number of expected nonprompt muon-neutrino charged-current interactions.	154
Table A-15. Number of expected neutral-current neutrino interactions.	154

1 Introduction

The Standard Model of particle physics describes the fundamental components of matter and their interactions. The basic building blocks are three generations of two doublets of particles, one consisting of two massive quarks, the other consisting of a massive lepton and a massless neutrino. Bound states of quarks make up nuclei and together with the lightest lepton, the electron, they form atoms and molecules. Recent measurements of the neutrino flux from the sun and from the interactions of cosmic ray particles in the upper atmosphere have yielded unexpected results that are inconsistent with a massless neutrino [1], [2]. If these observations are confirmed, the Standard Model will have to be extended and one of the many consequences of this extension is the possibility of a non-zero neutrino magnetic moment.

Neutrinos are elusive to experimental physicists yet remain central to theoretical descriptions of the world around us. On the theoretical side, Pauli postulated the existence of neutral particles in a 1929 letter to a conference “...as a desperate remedy to save the principle of energy conservation in beta decay...”. On the experimental side, the electron neutrino was discovered first, in a 1956 nuclear reactor experiment by Reines and Cowan who searched for inverse beta decay [3]. The existence of a second type of neutrino, the muon neutrino, was established in 1962 [4], while the existence of the tau neutrino has only been established indirectly so far, through observation of the decay products in tau lepton decays [5]. Consequently, measurements of the tau neutrino mass or its magnetic moment in neutrino beam experiments have had to assume the existence of tau neutrinos. The results of these experiments are presented in references [6], [7], and [8].

Experiment E872 was designed to identify the tau lepton produced by the interaction of a tau neutrino with a nucleus [9]. High-energy proton interactions in a high-density target produce short-lived charm particles, some of which decay to tau leptons and the corre-

sponding tau neutrinos. The charged current weak interaction of tau neutrinos in the neutrino beam target produces tau leptons that can be identified in photographic emulsion through their short decay-length and their decay products. Once the existence of tau neutrinos in the neutrino beam is established, their properties can be investigated.

Tau neutrino interactions not expected within the Standard Model can be identified with two methods: through a larger than expected number of observed events or through their unique interaction features. A non-zero neutrino magnetic moment gives rise to electromagnetic interactions between neutrinos and electrons, producing only electromagnetic energy in the E872 detector. This signature is also produced by Standard Model neutrino-electron weak interactions, but the cross section is one thousand times smaller than the weak neutrino-nucleon interaction cross section, which makes a search for magnetic moment interactions essentially background-free.

This thesis presents a search for tau neutrino-electron magnetic moment interactions in the E872 data.

2 Phenomenology

2.1 Neutrinos in the Standard Model

The Standard Model of particle physics is the basis of our understanding of the world around us today. It has been successful in explaining many different phenomena in particle physics and astronomy.

The theoretical basis of the Standard Model was established by Glashow, Weinberg, and Salam in 1967 (see references [10] and [11]). The fundamental constituents of matter are organized by generation or family. Each of the three generations has two leptons and two quarks, and each of these exists as particle and as anti-particle. The particles that make up the world around us are from the first generation; they are the electron and the electron neutrino, the up and the down quark.

Interactions in the Standard Model are divided into three categories: strong interactions which occur only between quarks are mediated by gluons, electromagnetic interactions which occur only between charged particles are mediated by photons, and weak interactions which occur between all particles are mediated by the W and Z bosons. In composite particles, these interactions occur between the constituents, and in this way, neutral composite particles for example can interact electromagnetically through their dipole moments. The magnetic dipole moment μ of a charged particle is proportional to its spin,

$$\mu_e = g \frac{e}{m}, \tag{2-1}$$

where e is the electric charge and m the mass of the particle [13]. In this equation, the factor g accounts for the anomalous magnetic moment; it is equal to two for electrons in Dirac theory and slightly higher when all Standard Model effects are included [14]. As before,

neutral composite particles such as the neutron also have a magnetic moment, which is a combination of the magnetic moments of the constituent particles [12].

Neutrinos play a special role in the Standard Model in that they are the only particles that have zero mass and only interact via the weak interaction. However, recent experimental evidence indicates that neutrinos are massive as well and several experiments plan to address this specific question.

Since they are massless, neutrinos travel at the speed of light, and a change in the Lorentz frame of reference does not change their helicity¹; hence they only have one spin state. The neutrino exists only with left-handed chirality (ν_L) and the anti-neutrino exists only with right-handed chirality ($\bar{\nu}_R$). As a result, the total number of spin states is two² and the quantum mechanical description of a neutrino is a two-component wave function called Weyl spinor [12]. Since the neutrino is massless, its spin cannot be distinguished from its orbital angular momentum; both are parallel to the momentum vector and Standard Model neutrinos therefore have no magnetic dipole moment [15].

If neutrinos existed in two spin states, the second state should be produced in Z boson decays to two neutrinos. However, the number of neutrinos with a mass smaller than half the Z boson mass has been measured in Z decays to be three [16], which also limits the number of generations in the Standard Model to three. This holds true for all neutrinos that couple to the Z with the usual weak coupling strength.

The current experimental limits for a few neutrino properties are shown in table 2-1 [14].

neutrino	mass	mean life	magnetic moment
ν_e	$<15\text{eV}$	$> 7 \times 10^9 \text{s/eV}$	$< 1.8 \times 10^{-10} \mu_B$
ν_μ	$<0.17\text{MeV}$	$> 15.4\text{s/eV}$	$< 7.4 \times 10^{-10} \mu_B$
ν_τ	$<18.2 \text{ MeV}$	(no limit)	$< 5.4 \times 10^{-7} \mu_B$

Table 2-1. Current experimental limits for neutrino properties from reference [14].

-
1. The direction of the spin of massive particles depends on the frame of reference: A transformation to a frame moving faster than the particle changes the helicity (from left-handed to right-handed for example).
 2. Ordinary (massive) spin 1/2 particles have four states: left-handed and right-handed particle and left-handed and right-handed anti-particle.

2.2 Extensions to the Standard Model

There are several indications from experiments looking for neutrino oscillations that the Standard Model description of neutrinos is not complete and that the neutrino mass might not be exactly zero.

Neutrinos interact and are produced in flavor eigenstates. If they are massive, the mass eigenstates (free space wave function) might not be the same as the flavor eigenstates. The time-development of the original state then produces other flavor eigenstates as well. This process is known as neutrino oscillation. If a neutrino beam of one (known) flavor is produced and then observed far away from the production point, the other flavor eigenstates can be observed as well.

Neutrino oscillations have already been observed by the LSND collaboration [17]. The experiment detects neutrinos produced in the decay of pions, which is a well understood Standard Model process. The number of electron-neutrino interactions and the number of muon-neutrino interactions observed in a detector 30 meters from the neutrino source do not agree with expectations. The differences can be explained by oscillations from muon neutrinos to electron neutrinos on the path between the neutrino source and the detector. This result has not yet been confirmed by another experiment, instead other experiments that search for the same signal have ruled out most of the predicted parameter space [18].

Cosmic ray experiments observe neutrinos produced when cosmic ray particles hit the upper atmosphere [1]. The interaction produces many pions, which predominantly decay through the channel $\pi^+ \rightarrow \mu^+ \nu_\mu$. The muon itself decays according to $\mu^+ \rightarrow e^+ \nu_e \bar{\nu}_\mu$. As a result, underground detectors expect about twice as many muon neutrinos as electron neutrinos. Experiments observe as many muon neutrinos as electron neutrinos. The absolute number of observed electron neutrinos is consistent with the predicted flux, whereas the observed number of muon neutrinos is smaller than expected [20].

Neutrinos produced by the fusion process in the solar core have been observed by several experiments ([19], [21], [22], and [23]). The observed energy spectrum of electron neutri-

nos is not consistent with the expected spectrum, but can be explained by neutrino oscillations.

The three oscillation scenarios require three different oscillation channels: the LSND result can only be explained with a large $\nu_\mu - \nu_\tau$ mass difference, the atmospheric result can only be explained with a small $\nu_\mu - \nu_\tau$ mass difference, and the solar neutrino result can only be explained with a very small $\nu_e - \nu_\mu$ mass difference [21]. Since only two mass differences are independent in a model with three neutrino families, these results are mutually contradicting and at least one requires a different explanation.

The Neutrino Magnetic Moment

One possible explanation of the solar neutrino spectrum is that the electron-neutrino has a magnetic moment of the order of $10^{-11} \mu_B$ [24]. Left-handed neutrinos produced near the core of the sun would experience a spin flip to undetectable right-handed neutrinos as they travel through the magnetic field of the sun and earth-based experiments measure a smaller neutrino flux than expected.

The current upper limits for the neutrino magnetic moment given in table 2-1 were obtained in neutrino-electron scattering experiments that searched for an increase in the neutrino-electron scattering cross section. The limit for the electron-neutrino was obtained in an experiment with neutrinos from a nuclear reactor [25], while the limit for the muon-neutrino was obtained in an experiment with neutrinos from pion decay [26]. The limit for the tau-neutrino was obtained in the CERN BEBC beam dump experiment in an analysis similar to this thesis [8]. It was assumed that the interaction of protons with nucleons produced D_s mesons, which then decayed to tau-neutrinos. Neutrino interactions were recorded in a bubble chamber that provided good track resolution and electron identification. Direct evidence for the interaction of the tau-neutrinos with nuclei was not found, and the tau neutrino flux was based on D_s production and decay parameters measured in other experiments.

Astrophysical arguments lead to more stringent limits for the neutrino magnetic moment, but these depend on the model used and the values assumed for some of the parameters. For this reason only the direct measurements were included in table 2-1.

The nucleosynthesis that occurred at the early age of the universe is responsible for the primordial abundance of ^4He . A neutrino magnetic moment of more than about $1.5 \times 10^{-11} \mu_B$ would modify the process and create an overabundance of helium that is not observed today [27]. This limit should not be exceeded by more than two neutrino flavors. The cooling of helium stars also gives an upper limit. The decay of plasmons in these stars into pairs would accelerate the cooling process. Since no such acceleration has been observed, the largest neutrino magnetic moment has to be smaller than $1.1 \times 10^{-11} \mu_B$ [28]. The supernova explosion 1987A produced neutrinos, a few of which were observed by underground detectors. The length of the neutrino signal was about 10s, which implies an upper limit for the right-handed neutrino luminosity that in turn corresponds to an upper limit for the magnetic moment of $(0.2 - 0.8) \times 10^{-11} \mu_B$ [29]. This limit applies to all neutrino flavors.

Besides these astrophysical considerations, the detection of atmospheric neutrino interactions in underground detectors also leads to a limit [1]. The observation of neutrino oscillations implies that neutrinos have mass, see section 2.2 below. If oscillations occur between muon-neutrinos and tau-neutrinos, then the properties of these neutrinos can be investigated in atmospheric neutrino interactions. Since no evidence for neutrino-electron magnetic moment interactions has been found, the upper limit for the tau-neutrino magnetic moment is $1.3 \times 10^{-7} \mu_B$ [7].

Several experiments have measured a correlation between the flux of solar neutrinos and the number of sun-spots [30]. The flux decreases when there is a lot of sun-spot activity, which could be explained by a ν_e magnetic moment of the order of $(10^{-11} - 10^{-12}) \mu_B$. The neutrinos would undergo a spin-flip as they pass through the magnetic field associated with those spots, decreasing the number of neutrinos observed at the various detectors [31].

There are several different models that predict a non-zero magnetic moment for the neutrino. The simplest extension to the Standard Model shows how the neutrino magnetic moment scales with the neutrino mass. More complex models introduce additional particles to obtain a large magnetic moment while keeping the neutrino mass small at the same time. Some of the more relevant models are discussed in this section.

If neutrinos have a magnetic moment, then the right-handed chirality state must also exist. If the two spin states are simply combined (ν_R and $\bar{\nu}_L$), neutrinos become Dirac particles with four states [13]. Since the two additional states have never been observed, they can not participate in weak interactions, and they cannot contribute to the width of the Z boson as mentioned above.

The Majorana description of neutrinos does not include the two unobserved neutrino states, and the opposite spin partner of Majorana neutrinos are their anti-neutrinos [20]. Similarly to the Weyl description, a Majorana neutrino has only two states, ν_L and $\bar{\nu}_R$. The difference to the Standard Model is that this neutrino has mass, which means that a Lorentz transformation to a frame of reference moving faster than the neutrino will transform ν_L into $\bar{\nu}_R$. In the Majorana description neutrinos necessarily have no magnetic moment [20].

The Standard Model can be extended in a simple way by adding right-handed neutrinos and left-handed anti-neutrinos [20]. The neutrino magnetic moment in this model is produced when virtual charged bosons and fermions interact with the photon field, which is shown in figure 2-1.

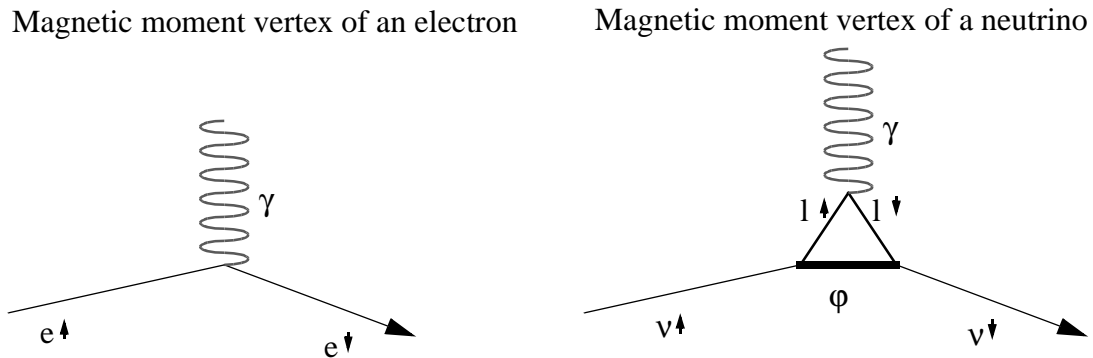


Figure 2-1. Magnetic moment interaction vertex of an electron and a neutrino. Which particles participate in the neutrino loop depends on the model, in this example leptons and gauge bosons ϕ comprise the loop.

The lowest order contribution to the magnetic moment interaction of a fermion is a simple tree diagram, shown on the left-hand side of figure 2-1. The charged fermion interacts with the photon field and changes its spin. The lowest order contribution to the magnetic moment interaction of a neutrino is a loop diagram, shown on the right-hand side of figure 2-1. The left-handed neutrino produces a pair of virtual particles that can also couple to the

right-handed neutrino. One of the virtual particles then interacts with the photon field and changes its spin as before. Afterwards the two particles re-combine to a right-handed neutrino.

A calculation of the neutrino magnetic moment at the lowest order involves loop diagrams as shown in figure 2-1 with quarks and leptons on the internal lines. The calculation gives a magnetic moment μ_ν that is proportional to the neutrino mass,

$$\mu_\nu = \frac{3eG_F}{8\sqrt{2}\pi}m_\nu, \quad (2-2)$$

where e is the electron charge, G_F the Fermi coupling constant, and m_ν the mass of the neutrino [20], and the numerical value for the neutrino magnetic moment is then

$$\mu_\nu = 3.1 \times 10^{-19} \mu_B \left(\frac{m_\nu}{1\text{eV}} \right). \quad (2-3)$$

A tau neutrino mass at the current limit of 18.2MeV would give a magnetic moment of $\mu_\nu = 6 \times 10^{-12} \mu_B$ [14].

Another model that includes Dirac neutrinos is the left-right symmetric model. The left and right-handed neutrino helicities play identical roles at very high energies, while the symmetry is broken at small energies [32]. The predicted neutrino magnetic moment is similar to equation 2-3.

In Grand Unified Theories (GUT) the neutrino magnetic moment is in general not zero [33]; it has been calculated for models that include leptons and quarks in the same sector [34].

Models can also be constructed in which the neutrino mass is small and the magnetic moment nevertheless large. In one such model, the interactions of ν_e and $\overline{N_{eL}}$ (the antiparticle of N_{eR} , the right-handed electron-neutrino) is considered to be symmetric under an $SU(2)_\nu$ symmetry transformation with ν_e and $\overline{N_{eL}}$ forming a doublet [24]. In this case the Dirac mass of ν_e is a triplet under $SU(2)_\nu$ whereas the magnetic moment term is a singlet. As a result, equation 2-3 is invalid and a large magnetic moment is possible.

2.3 Neutrino Interactions

Standard Model neutrinos interact only via the weak interaction, exchanging W bosons in charged-current interactions (CC) or Z bosons in neutral current interactions (NC) with other particles. Examples for the two types of interaction are shown in figure 2-2.

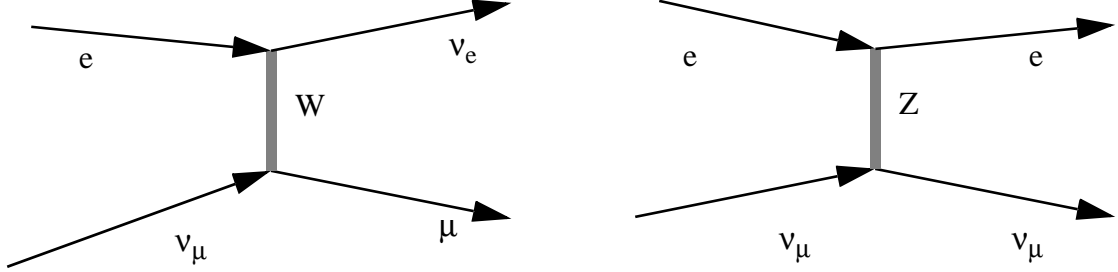


Figure 2-2. Feynman diagram showing two weak interactions of neutrinos (ν) with an electron (e). The left hand side shows a charged-current interaction (exchange of a W boson); the right-hand side shows a neutral-current interaction (exchange of a Z boson).

The differential cross section for a charged-current neutrino-electron interaction is given by

$$\frac{d\sigma^{\text{CC}}}{dy} = \frac{G_F^2 s}{\pi}, \quad (2-4)$$

where G_F is the Fermi coupling constant [12]. The fractional energy loss of the neutrino is given by $y = T/E_\nu$, where T is the outgoing electron energy and E_ν is the incoming neutrino energy. The square of the center-of-mass energy s is given in the laboratory frame (target electron at rest) by

$$s = m_e^2 + 2m_e E_\nu, \quad (2-5)$$

where m_e is the electron mass. The charged-current cross section is independent of y .

The differential cross section for a neutrino-electron neutral-current interaction is given by

$$\frac{d\sigma^{\text{NC}}}{dy} = \frac{G_F^2 m_e E_\nu}{2\pi} [(g_V^{\nu e} + g_A^{\nu e})^2 + (g_V^{\nu e} - g_A^{\nu e})^2 (1-y)^2], \quad (2-6)$$

where g_V is the vector coupling, and g_A the axial coupling. The couplings are given by

$$\begin{aligned} g_V^{ve} &= -0.5 \\ g_A^{ve} &= -0.5 + 2\sin^2\theta_W, \end{aligned} \quad (2-7)$$

where θ_W is the Weinberg angle with $\sin^2\theta_W = 0.223$.

The weak cross sections from equations 2-4 and 2-6 are also valid for the interaction between neutrinos and quarks. The neutrino-nucleon cross section is more complicated because it depends on the quark content of the nucleon and is modified by quark-quark interactions. Nevertheless, nucleons are about 2000 times heavier than electrons, and since the weak cross sections are proportional to the target particle mass, most of the events recorded in any neutrino-beam experiment are from neutrino-nucleon interactions.

Neutrino magnetic moment interactions can occur with any charged particle, electron or nucleon, and contrary to weak interactions, the interaction cross section is independent of the mass of the target particle.

The Feynman diagram for the magnetic moment interaction of an electron and a neutrino is shown in figure 2-3. The particles exchange a spin one photon and undergo a spin-flip in the interaction.

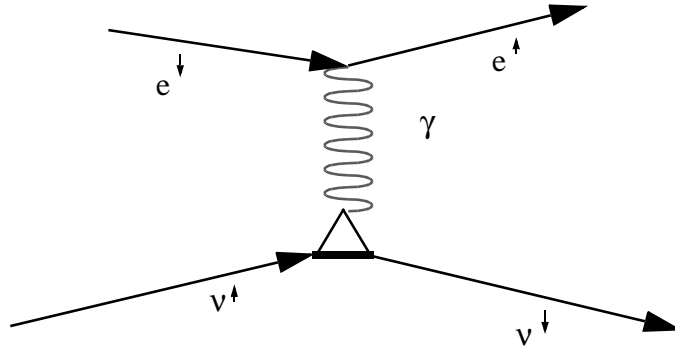


Figure 2-3. Feynman diagram of a neutrino-electron magnetic moment interaction. The arrow next to a particle symbol represents the helicity.

The interaction of the photon with the electron is an electromagnetic Standard Model process shown on the left-hand side of figure 2-1, while the interaction of the photon with the neutrino is shown on the right-hand side of figure 2-1. Since this coupling must include a

right-handed neutrino, the observation of magnetic moment interactions would establish its existence.

The differential cross section for the process shown in figure 2-3 is given in the lab frame by [35]

$$\frac{d\sigma^\mu}{dy} = f_\mu^2 \frac{\pi\alpha^2}{m_e^2} \left(\frac{1}{y} - 1 \right), \quad (2-8)$$

where $\alpha \cong 1/137$ is the fine structure constant and $f_\mu = \mu_\nu/\mu_B$ is the size of the neutrino magnetic moment relative to a Bohr magneton. Equation 2-8 is only valid in the high-energy approximation of $y \gg (m_\nu/E_\nu)$ and it should not be used near the divergence at $y \rightarrow 0$. However, since the neutrino mass is small, experiments are typically far away from this divergence. The lower limit for y is typically determined by the experimental sensitivity to low-energy electrons. Since the differential cross section increases as $1/y$, this limited sensitivity therefore also determines the size of the total cross section and the total number of events that could be observed.

The initial state and final state particles are identical between weak neutral current interactions and magnetic moment interactions, which could give rise to quantum interference effects between the two interactions. However, the magnetic moment process changes the spin of the neutrino and the electron, which means that no such interference can occur.

This y -dependence can in principle be used to distinguish magnetic moment and neutral-current neutrino-electron scattering processes. Both cross sections are compared in figure 2-4, and the magnetic moment cross section dominates at very small y .

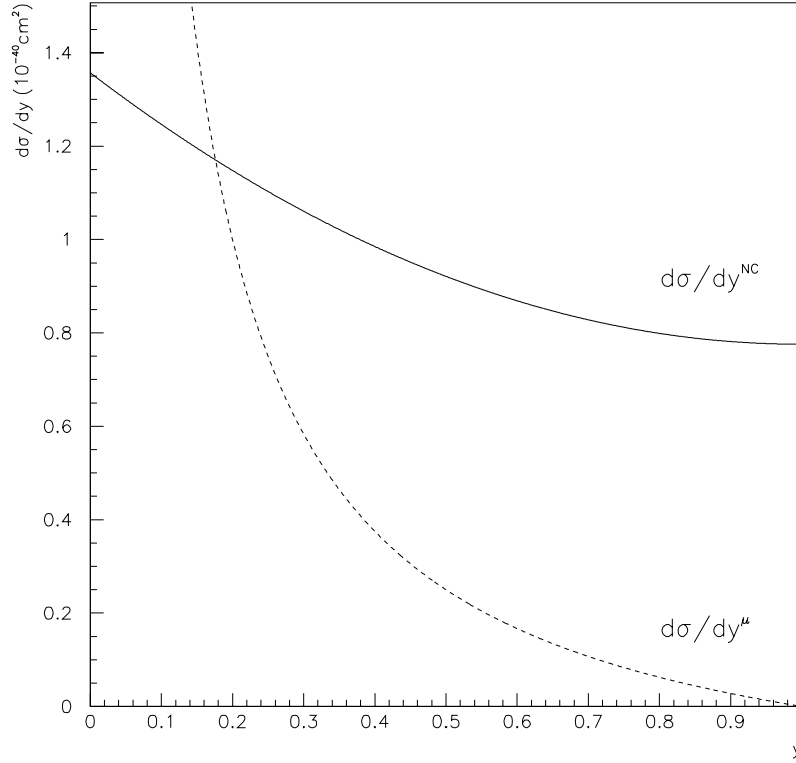


Figure 2-4. Differential cross section for neutrino-electron scattering. The dashed line shows the y -dependence due to a magnetic moment of $10^{-8} \mu_B$. The solid line shows the differential cross section for neutrino-electron neutral-current scattering (ν_μ or ν_τ). A neutrino energy of 50 GeV was used to generate this plot.

Thus any search for evidence of a neutrino magnetic moment is concentrated on detecting electrons with small kinetic energies. Due to the small experimental tau neutrino flux it is usually not possible to measure the differential cross. Rather, only the total cross section is measured, which is found for magnetic moment interactions by integrating equation 2-8:

$$\sigma_{\text{tot}}^{\mu} = \int_{y_{\min}}^1 \frac{d\sigma^{\mu}}{dy} dy = f_{\mu}^2 \frac{\pi \alpha^2}{m_e^2} [y_{\min} - \ln y_{\min} - 1] . \quad (2-9)$$

The lower integration limit is given by the low-energy cutoff $y_{\min} = T_{\min}/E_{\nu}$, where T_{\min} is the low-energy experimental detection limit for electrons. Since y is smaller than one, the

total cross section depends logarithmically on y_{min} . It also only increases logarithmically with the incoming neutrino energy.

The extensions to the Standard Model mentioned above indicate that neutrinos might possess a magnetic moment, and some of them predict values for the magnetic moment that are just below the current experimental sensitivity [24]. If the solar neutrino problem is indeed due to a ν_e magnetic moment, then the other two neutrino flavors should have magnetic moments of similar magnitude.

Neutrino-electron scattering provides a relatively background-free channel to detect magnetic moment interactions because the weak cross section for this interaction is small. Magnetic moment interactions would increase the number of scattered electrons, predominantly with small momentum. Measuring the number of neutrino-electron scattering events therefore yields an estimate for the tau neutrino magnetic moment.

3 Experimental Setup

The DONUT¹ experiment was designed to produce and identify tau neutrinos and to search for non-Standard Model interactions as described in chapter 2. A high-energy neutrino beam containing tau neutrinos was directed onto a neutrino interaction target in which the interactions of tau neutrinos and nuclei were recorded.

The identification of these interactions was based on the detection of the tau lepton and the high-momentum hadrons produced in the charged-current interaction of a neutrino and a nucleon. Since the tau lepton decays with a decay length of about 2mm in this experiment, a high-resolution detector was required. These short tau tracks were recorded with sheets of photographic emulsion interleaved with thin steel plates. Emulsion works as an integrating detector similarly to photographic film: charged particles passing through an emulsion sheet initiate a chemical process that modifies the molecular structure. This modification becomes visible after the emulsion is developed.

Hadrons and other leptons produced in neutrino-nucleon interactions were recorded with a conventional spectrometer, which was used to identify the neutrino interaction type, measure event parameters, and determine the location of the neutrino interaction vertex in the emulsion.

The individual components of the apparatus are discussed in this chapter.

3.1 The Neutrino Beam

The primary source of high energy particles was the Fermilab Tevatron, a superconducting synchrotron that accelerated protons to a maximum energy of 800GeV. To produce the neutrino beam for this experiment, 800GeV protons extracted from the Tevatron were steered

1. DONUT: Direct Observation of Nu Tau

onto a tungsten target, where the protons collided with target nucleons and generated many different final-state particles. Neutrinos from charm meson decays formed the prompt component of the neutrino beam. Most light long-lived particles such as pions and kaons interacted and lost energy in the target material before decaying. The decays of these particles produced a background of low-momentum non-prompt neutrinos. The computation of the neutrino beam composition and its energy-spectrum is outlined in appendix A.

The target was a 1m long, square (10cm by 10cm) tungsten block surrounded by a 10cm copper sheath that was water-cooled to remove the 25kW of power in the beam.

To understand the prompt and non-prompt components of the neutrino beam, the target was designed with half of the material cut out of half of the tungsten block to give an effective density of 0.5 with respect to the nuclear interaction length. The fraction of non-prompt neutrinos in the neutrino beam was obtained by comparing the number of muons produced in the two targets. The “full-density” side of the target was used during most of the data taking period.

The “half-density” target had 25mm wide strips of tungsten separated by 25mm of air. Figure 3-1 shows a schematic drawing of the proton beam target.

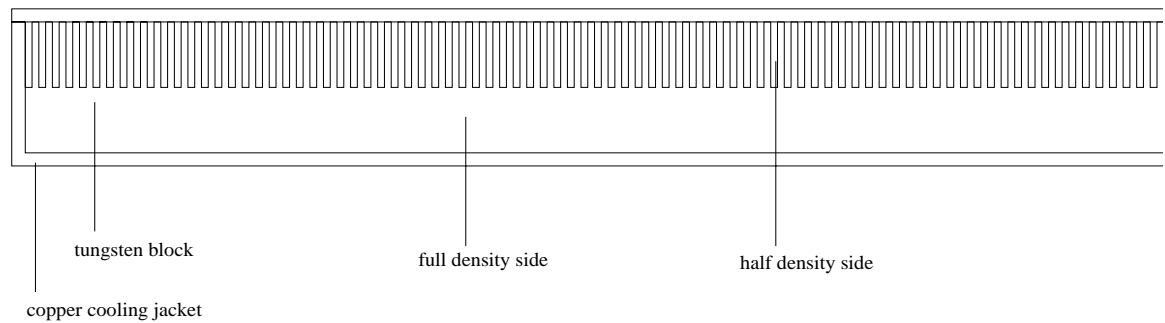


Figure 3-1. Layout of the proton beam target. The proton beam is incident from the left.

The nuclear interaction length of tungsten is 0.0959m, while the average decay length for pions at these energies is about 5×10^2 m. Thus only 0.1% of the pions produced in the target decayed to neutrinos before interacting. This number did not change significantly in the half-density target.

Charm particles have a life time of about 10^{-12} s and most of them decayed before they interacted. Each of these semi-leptonic charm decays produces a neutrino and a lepton of the same flavor. The tau lepton also has a short life time and its decay produces a second tau neutrino.

Since the neutrino interaction targets contained emulsion, which records every charged particle track passing through it, the total number of charged particles (mostly muons) in the neutrino target region had to be kept below about $10^5/\text{cm}^2$. Active shielding consisting of dipole magnets (shown in figure 3-2) was used to deflect the high-momentum muons away from the neutrino target. The first magnet downstream of the proton beam target was a 7m long aperture-less dipole operating in saturation at a field of 3.0T. The second magnet was a 5m long toroidal magnet operating at a field of 2.1T. Together, the two magnets divided the beam of high-energy muons into two “plumes” separated by about 2m at the emulsion target.

Most of the low-momentum muons produced in the proton beam target lost their energy through ionization and interactions in the 18 meters of steel shielding between the proton beam target and the emulsion target. Conversely, shielding material in the path of the high-energy muon plumes was removed to reduce the background from high-momentum muons interacting in the shielding. The complete configuration is shown in figure 3-2.

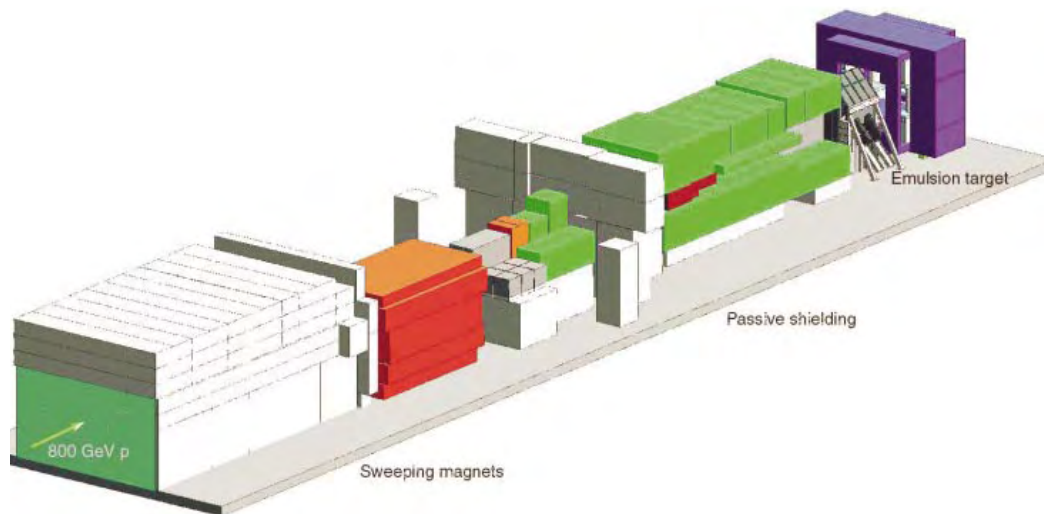


Figure 3-2. Neutrino beam active and passive shielding. The proton beam target is located on the left. The first magnet is encased in concrete on the left. Most of the shielding surrounding the target is not shown.

3.2 The Emulsion Target

Tau leptons produced in the charged-current interactions of tau neutrinos and nuclei decay with a half-life of 2.90×10^{-13} s. At the typical energy of 50 GeV this corresponds to a path length of approximately 2.5 mm. Since 80% of the taus decay to one charged particle and several neutral particles, the tau and its decay can be identified in the emulsion target as a short track and a “kink” produced in its decay.

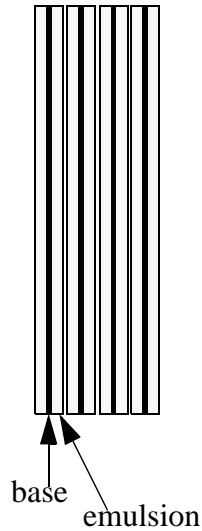
The emulsion consists of crystals of silver halide embedded in gelatin. Charged particles traversing the emulsion produce ionization that modifies the halide grains. These modified halides turn into small grains of silver with a diameter of about $1\mu\text{m}$ in the development process.

The emulsion was placed on 0.5 m by 0.5 m large plastic sheets to provide mechanical strength and improve ease of handling. Two types of emulsion configurations were used. The first type, called “bulk”, had a $90\mu\text{m}$ thick plastic base coated with $330\mu\text{m}$ thick emulsion. Many sheets were stacked to form 70 mm thick emulsion module as shown in figure 3-3. Nuclear emulsion constituted 95% of the mass of a bulk module. Emulsion used in this configuration is a volume tracking detector; the vertex and all of the charged particle tracks from a neutrino interaction are recorded in the emulsion.

The second type, called “ECC” (emulsion cloud chamber), had 1 mm thick stainless steel plates interleaved with emulsion sheets. An ECC module is shown on the right-hand side of figure 3-3. The emulsion sheet had a $200\mu\text{m}$ thick plastic base with coatings of $100\mu\text{m}$ emulsion on each side. Since emulsion contributes only 5% to the mass of a module, an ECC module is a sampling detector with very high resolution perpendicular to the beam direction. The vertex of a neutrino interaction will most likely not be visible in the emul-

sion, 95% of the time it will occur in the steel. The charged particle tracks are visible only as “track segments” in each emulsion layer.

bulk module (84 plates)



ECC module (54 plates)

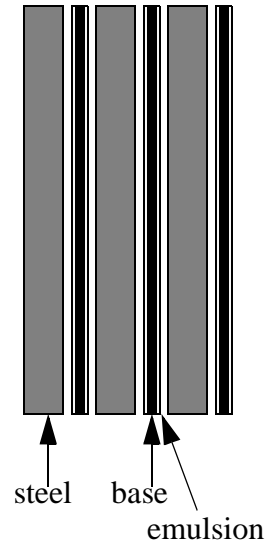


Figure 3-3. Design of emulsion modules: bulk and ECC.

Additional emulsion sheets were mounted on the front and back of every module. These sheets were replaced several times during one emulsion module exposure and are called “changeable sheets”. Due to the short exposure time, they had a much lower track density than the modules, making it easier to connect spectrometer tracks to emulsion tracks.

The emulsion modules were mounted in four different target stations, shown in figure 3-4.

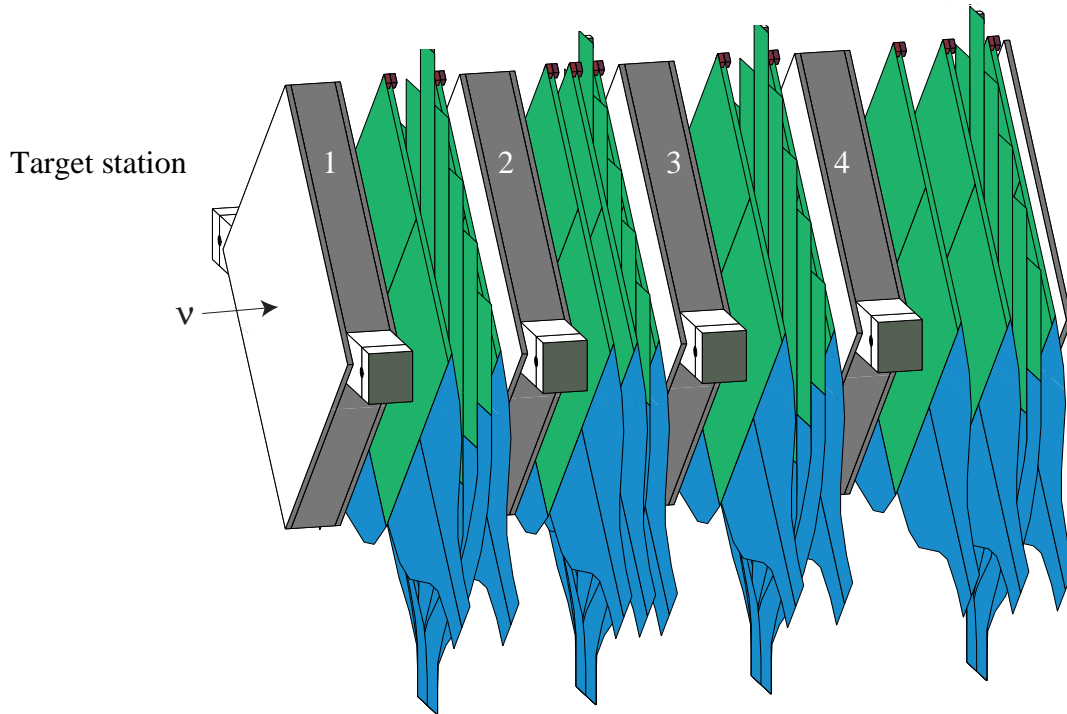


Figure 3-4. Emulsion target and scintillating fiber tracker configuration. Several planes of scintillating fibers were mounted downstream of each of the four target stations. The fiber planes were arranged in three different orientations and the six image intensifiers and readout CCD modules underneath the target region are not shown.

Each of the four stations was designed to hold one emulsion module, and the modules were exchanged several times during the data taking period.

3.3 The Spectrometer

The spectrometer was located 36 meters downstream of the proton beam target. Its main purpose included the identification of neutrino interactions, the measurement of event parameters, and the prediction of the neutrino interaction vertex location in the emulsion. A plan view of the components is shown in figure 3-5.

Neutrino interactions were selected by the trigger system, which required the production of several high-momentum particles in the spectrometer with no incoming charged particle track.

Event parameters were determined by three detector elements: the electromagnetic calorimeter was used to identify electron-neutrino interactions and to measure the electromagnetic energy, the muon ID system was used to identify muons produced in the neutrino interaction, and a combination of drift chambers and a magnetic field was used to measure the momentum of charged particles produced in the interaction.

Scanning all of the emulsion volume with the current setup would take 100 years [39], and the scanning time is proportional to the scan volume. To reduce the amount of emulsion that had to be scanned, the vertex location was estimated with the spectrometer to within about 2mm from reconstructed charged particle tracks.

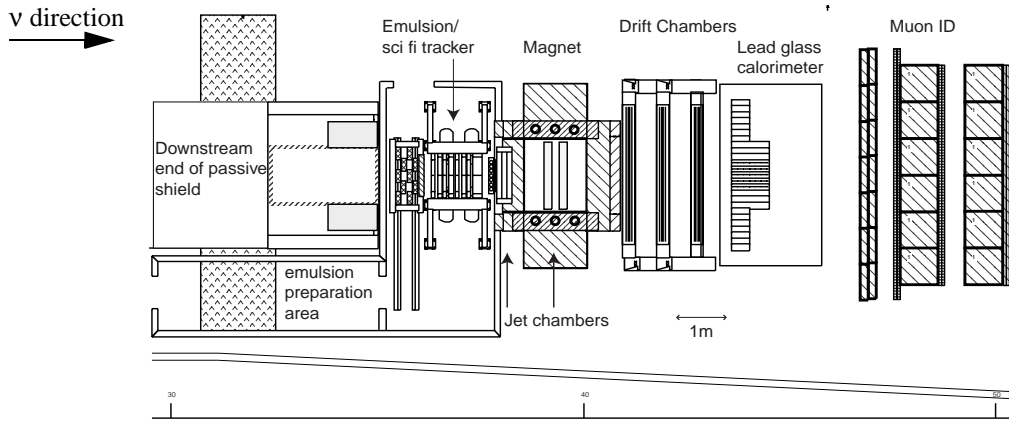


Figure 3-5. Plan view of the spectrometer.

A schematic view of the emulsion target region is shown in figure 3-6.

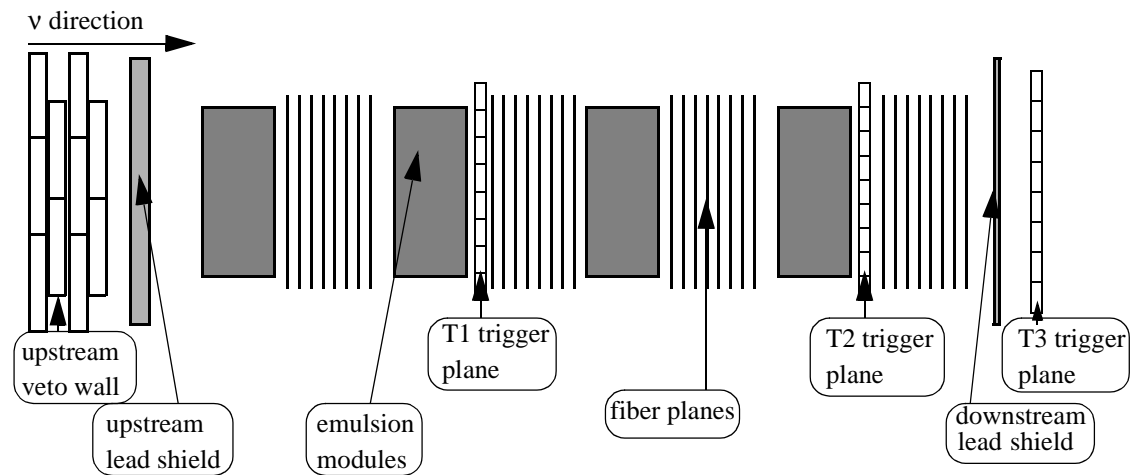


Figure 3-6. Top view of the emulsion target region. The shield was also installed on top and on the side of the target region.

The emulsion module and the scintillating fiber planes were mounted together on a steel frame, shown in figure 3-7.



Figure 3-7. View of the target stand (on the right) and the upstream veto trigger wall (on the left). The lead shield in between the veto wall and the target stand is also shown. The large tubes at the bottom of the target stand are the enclosures for the image intensifier modules.

The lead shield surrounded the target frame: a 20mm thick wall was placed between the upstream veto trigger wall and the first emulsion module, a 20mm thick layer covered the

top of the target frame, and a 6mm thick layer was placed between the last scintillating fiber plane and the downstream trigger plane T3.

The Trigger Counters

The trigger system was designed to select events that had the signature of a neutrino interaction in the emulsion. This was defined as at least two high-momentum charged particle tracks coming from the emulsion targets and no incoming charged particles.

Charged particles entering the upstream side were rejected by the veto wall. It consisted of two planes of 2.64m by 0.35m by 1.93m scintillator counters and each plane contained five counters. Photomultiplier tubes (PMT) mounted at both ends of the counters converted light from the scintillators into electronic signals [40]. Each of the counters had a detection efficiency for minimum ionizing particles of better than 95%, which gives a veto wall efficiency of better than 99%.

High-momentum particles coming from the emulsion were selected with three trigger planes that were interleaved with the emulsion modules. The first two planes were segmented into 0.0875m wide bundles of scintillating fibers and read out by Hamamatsu R5600 PMTs. The first trigger plane, T1, was located just downstream of the second emulsion module. It had eight segments and covered an area of 0.7m by 0.7 m, extending beyond the emulsion modules by 10cm on all sides. The second plane, T2, was located just downstream of the fourth emulsion module. It was built with nine of the same bundles as T1 and covered an area of 0.79m by 0.7m. The third trigger plane, T3, was located in the upstream aperture of the analysis magnet. T3 consisted of eight plastic scintillator counters, each 0.8m long, 0.1m wide, and 0.005m thick. The counters were attached to 0.49m long light guides and read out at both ends by Philips 2262B phototubes. The electronic signals from both ends were combined to give position-independent timing information.

Each of the trigger counters had an efficiency of better than 97% for minimum-ionizing particles.

The Scintillating Fiber Tracking System

A scintillating fiber detector was used to predict the position of the neutrino interaction vertex in the emulsion by recording the high-momentum charged particle tracks coming from the interaction vertex. The scintillating fiber planes provided position measurements for several sampling points along the track. Figure 3-4 shows the emulsion target and scintillating fiber system. The fiber planes were interleaved with the emulsion modules to provide at least four sampling points in two different orientations for each charged particle track.

A scintillating fiber is a plastic fiber with a polystyrene center (core) doped with 1% butyl-PBD¹ and 0.1% BDB² scintillator. When an ionizing particle traverses the fiber, light is produced in the scintillator material of the fiber core (luminescence). The center has a refractive index of 1.59 and is surrounded by a PMMA³ cladding with a refractive index of 1.49 and a thickness of 0.015mm for a total fiber thickness of 0.5mm. The difference in index of refraction traps about 4% of the light in the fiber, which acts as light guide.

Since aluminum was deposited on the end of the fiber opposite to the readout chain, the difference in light output due to ionization between the two ends was less than 10%.

The fibers were mounted in planes with three different orientations: vertically, and at +45° and -45°, see figure 3-4. The vertical planes had four layers of fibers while the diagonal planes had two layers. Each layer was coated with TiO₂ paint to increase the light output,

-
1. butyl-2-phenyl-5(4-biphenyl)-1-3-5-oxadiazole
 2. 4,4'-bis-(2,5-dimethylstyryl)-diphenyl
 3. polymethyl methacrylate

to eliminate cross-talk between two fibers, and to keep the fibers in place. The average distance between the center of a fiber plane and the readout system was 0.75m.

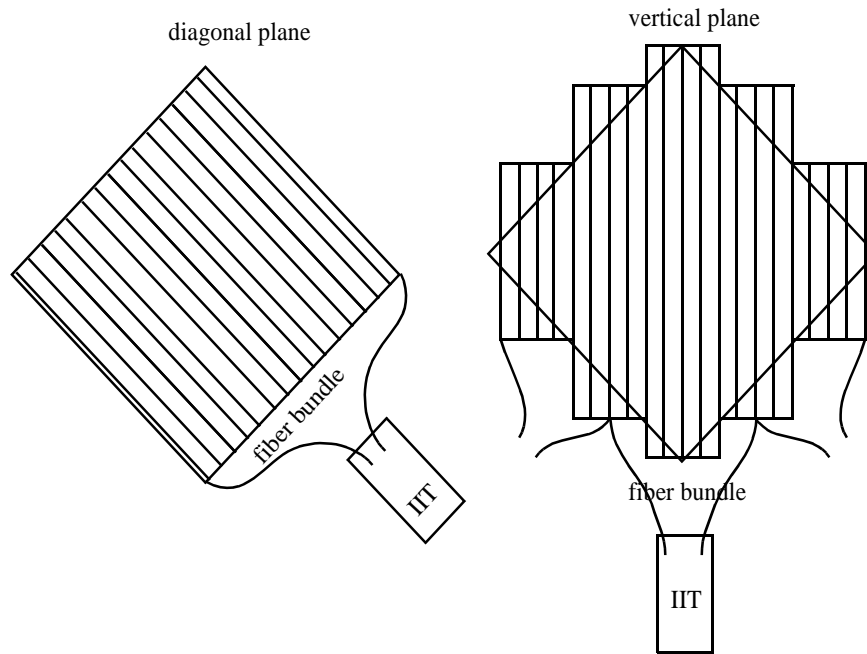


Figure 3-8. Front view of the fiber layout of two different planes. Different sections of the vertical plane are connected to different image intensifiers (IIT).

Light produced in the fibers was amplified by chains of image intensifiers (IIT)¹ and read out by CCD² modules. Light from the fibers entered the image intensifier chain and produced electrons in the photocathode of the entrance window (see figure 3-9). Each image intensifier accelerated the electrons by a potential difference of a few thousand volts and focussed the electrons to reduce the image size. A phosphor screen at the output window of each stage converted the electrons back into photons, which were transferred to the input window of the next stage through a fiber optic window.

The phosphor screens were also used to delay the scintillating fiber signal from neutrino interactions until a trigger pulse was received. It took about 20 μ s for the light intensity in each screen to drop to 10% of the initial value. The third image intensifier module was

1. Image Intensifier type IC-5502X made by Hamamatsu Photonics, Japan

2. Charge-Coupled Device, light-sensitive semiconductor that is also used in video cameras.

therefore used as a gate; its potential difference was kept at 3kV and increased to 9kV only when a trigger condition was generated.

Due to the decay time of the phosphor screen, the signal at the output of the fourth module also had a different time structure than the light signal from the fibers. When the IIT output image was recorded, it not only contained the signal from particles that had just passed through the fibers, but also signals that were produced several tens of microseconds earlier, although with a smaller light intensity. The gating mechanism reduced this signal-overlap effect because only the phosphor screens of the first two image intensifier stages contributed to the problem.

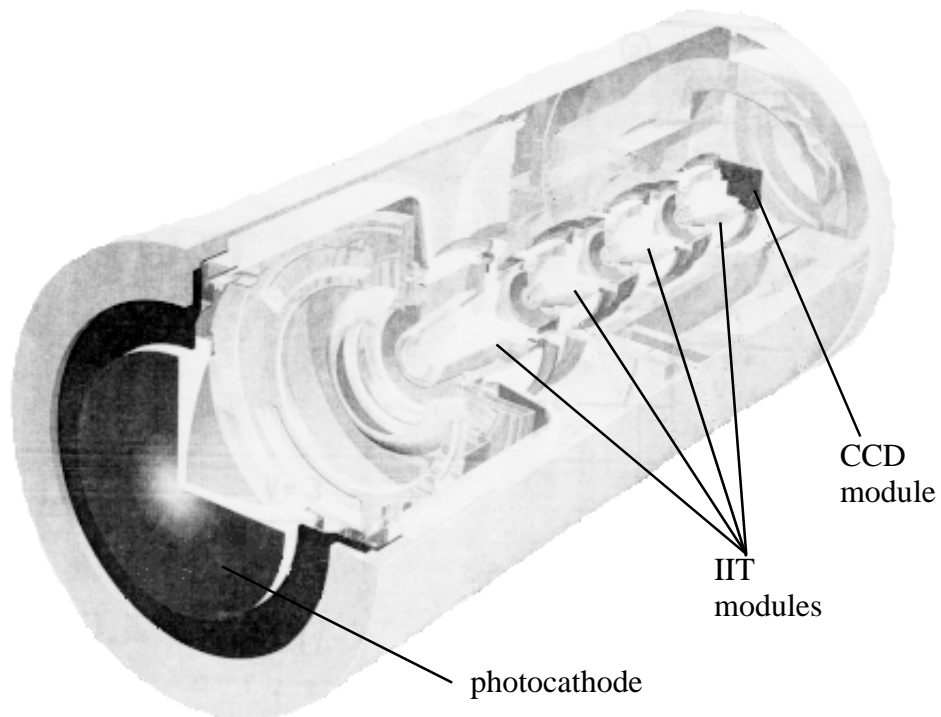


Figure 3-9. One readout module, consisting of four image intensifiers and a readout CCD module.

The performance of the IIT modules depends on two parameters: The quantum efficiency of the first stage determines the probability to produce any signal while the overall gain determines the magnitude of the output signal. In DONUT, the quantum efficiency was 22%, producing an average of four photoelectrons per charged particle fiber crossing. The average gain for all modules was 4×10^6 , and the focussing stages of the IIT chain resulted

in a total de-magnification factor of 12. The phosphor screen of the fourth IIT stage was coupled to a CCD module that converted input light into electric charge. The CCD had a sensitive area of 8.8mm by 6.6mm divided into 768 by 493 pixels, which means that the images of two neighboring fibers were separated by about three pixels on the CCD image. The separation was slightly larger at the edge of the image due to the pin-hole optics of the IIT modules.

The path of electrons in the IIT stages was very sensitive to external magnetic fields that would distort the output image. Consequently, the IIT modules were shielded from the magnetic field of the analysis magnet with large soft iron canisters.

The charge collected from the CCD module was digitized by an eight bit flash ADC custom-built for an experiment at KEK and later modified for this experiment [41]. It converted the analog pixel charge into an eight bit word at a rate of 14MHz. If all pixels were read out, the data rate would be 56MBytes/second, but the data acquisition system had a limit of 23MBytes/second and would not be fast enough to receive all of the information. A digital discriminator circumvented this limitation by only passing data into the readout stream if a pixel had a charge above threshold. Approximately half of the CCD image area was mapped by fibers, as can be seen in figure 3-10. Also, only a small percentage of the fibers generated a signal in a typical event, reducing the data rate significantly. As a result, the mean readout time for a single event was 24ms.

Electro-optical distortions and the residual magnetic field in the IIT modules affected the mapping between fibers and CCD pixels. An optical calibration system therefore monitored the location of a few fibers on the CCD image throughout the data taking period. The

mirrored end of every 12th fiber was connected to an electroluminescence (ELP) plate and light from these “fiducial fibers” was easily found on the CCD image (figure 3-10).

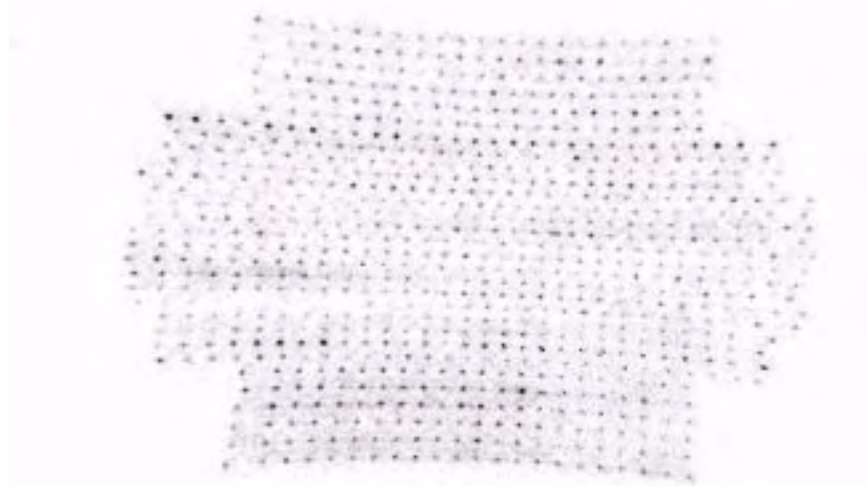


Figure 3-10. CCD image of the fiducial fibers. A dark pixel has a lot of charge, a white pixel a small charge.

The fiducial image was taken in between runs; the ELP was turned off during data acquisition. This frequent mapping procedure achieved a fiber position accuracy of better than a fraction of a pixel.

Downstream Tracking

Charged particle tracks coming from the neutrino interaction vertex and identified in the scintillating fiber system give information about the neutrino interaction parameters. The particle momentum for these tracks was determined through the combination of drift chamber tracking and deflection in a magnetic field [39].

Charged particles travelling through the E872 analysis magnet experienced a deflection equivalent to a momentum kick of 228MeV. The magnitude and direction of the magnetic field was mapped out in a survey prior to the installation of the drift chambers.

Three of these chambers were installed upstream of the analysis magnet. They are called “VDC” because they were previously used as vertex drift chambers in Fermilab experiment E665 [43]. They had an active area of 1m by 0.7m and a resolution of 0.2mm. The first

chamber was placed vertically, the second at an angle of $+5^\circ$, and the third chamber at an angle of -5° .

The direction of tracks passing through the analysis magnet was measured in three stations of drift chambers (“DC”) downstream of the analysis magnet. Each station had four sensitive planes with an active area of 3.3m by 1.6m and a resolution of 0.35mm. The first two planes, offset by half a cell width, provided a vertical position measurement while the third plane was rotated by 17° and the fourth plane by -17° to allow the three-dimensional reconstruction of charged particle tracks.

Additional drift chambers were installed in the center of the analysis magnet during the data taking period to improve the horizontal resolution. The first chamber provided a measurement of the horizontal position with four sample points per track and the second chamber provided a measurement of the vertical position.

The achieved momentum resolution of the magnet and drift chamber system was $\Delta p/p \approx 10\%$ at a momentum of $p=10\text{GeV}$ and $\Delta p/p \approx 20\%$ at $p=100\text{GeV}$ [38].

The Electromagnetic Calorimeter

Electron-neutrino charged-current interactions and tau decays produce high-energy electrons. As they pass through material, these electrons generate electromagnetic showers that can be identified in the electromagnetic calorimeter (EMCAL), which provided an estimate for the electromagnetic energy of individual particles and was also used as part of the trigger logic [44].

The EMCAL was segmented into 400 lead glass and scintillating glass blocks of dimension 0.15m by 0.15m by 0.89m. One hundred blocks in the center had a smaller surface area (0.075m by 0.075m) to improve the position resolution. These center blocks and the surrounding blocks were made of scintillating glass; they were 20.9 radiation lengths and 2.0 nuclear absorption lengths deep. The outer parts of the detector were built of lead glass blocks; each had a depth of 16.8 radiation lengths and 1.0 nuclear absorption lengths. The blocks were read out by photomultiplier tubes.

A few of the blocks were calibrated in a beam test with particles of known energy, and the response of all other blocks was normalized with respect to these calibrated blocks by their relative response to high-energy muons. An LED system was used to monitor the performance of each block and to correct for gain variations in the readout PMTs.

The resolution of the calorimeter was $\Delta E/E = 10\% + 10\%/\sqrt{E}$, where E is the electromagnetic energy signal measured in the calorimeter. The resolution changed slightly from block to block and at the beginning of the run. Also, due to electronic noise, the constant term was significantly larger at the beginning of the run, making the calorimeter unsuitable for physics analysis during that time.

Muon Identification

A muon neutrino charged-current interaction can be uniquely identified by the muon produced in the interaction. Unlike electrons and hadrons, muons can pass through a lot of material, they only lose energy through ionization, whereas electrons lose their energy in electromagnetic showers and hadrons lose their energy in hadronic showers.

A three-layer sandwich of steel plates and detectors was used to identify muons downstream of the electromagnetic calorimeter. The steel stopped electrons and hadrons, only muons passed through to produce hits in the active detector planes [36].

The upstream wall had a size of 6.25m by 3.7m by 0.42m, while the other two walls had dimensions of 5.48m by 3.25m by 0.91m each. Six planes of proportional tubes were mounted on the front and back of the second wall and on the back of the third wall. They provided a horizontal and a vertical position measurement with a resolution of 0.04m. The proportional tubes had a resolving time of 1 μ s, which was too long for the intense muon flux in the plumes. Scintillator hodoscopes were used instead in these regions; they covered about 20% of the area [37].

Alignment

The accuracy of the vertex prediction depends on the precision with which the track position can be determined in the scintillating fiber system. Similarly, the accuracy of the momentum estimate depends on the accuracy of the track position in the drift chambers.

To align the scintillating fibers with respect to the emulsion and the other spectrometer elements, each SF plane was surveyed before it was mounted in the target stand. Fiber location, offset and angles between fibers were recorded in the survey for 10% of the fibers, and the position of the stand itself was also determined.

Alignment of the fiber planes was periodically monitored with single muons passing through the detector. The straightness of the muon track typically allowed the reconstruction of the trajectory to an accuracy of about 0.5mm at the center of an emulsion module. Projected to the changeable sheet, the track location was determined to within a distance of about 0.35mm, as shown in the bottom row of figure 3-11.

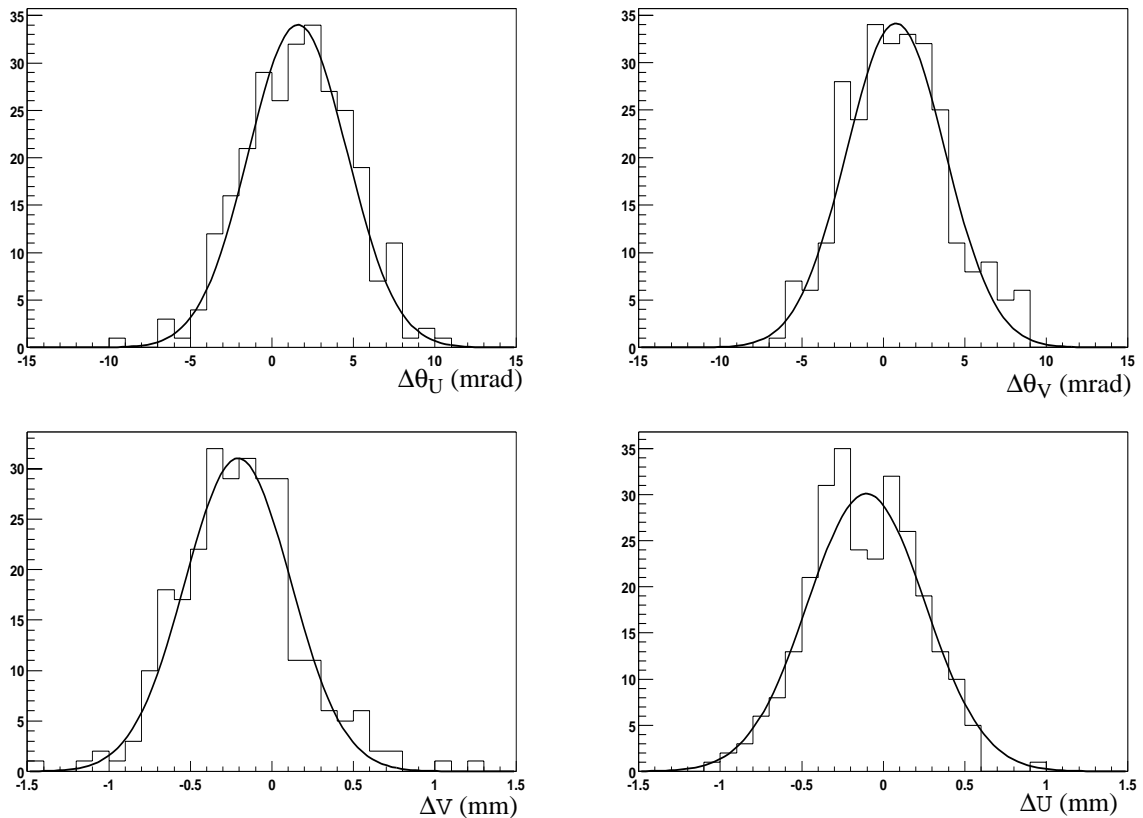


Figure 3-11. Histogram of the angle and position projection error from the SF system to changeable sheet CS5. The top row shows the difference between track angle determined in the SF system and track angle determined in the emulsion. The angle difference has a sigma of 3.3mrad. The bottom row shows the difference between the track position determined in the SF system projected to the Z position of the changeable sheet and the track position found in the changeable sheet. The difference between projection and emulsion track position has a sigma of 0.35mm. The data are from a cosmic ray run and the smooth line is a Gaussian fit to the data.

A histogram of the track angle error is shown in the top row of figure 3-11 [42], the angle was typically determined with an accuracy of 3.3mrad.

The drift chambers were also aligned with single muons passing through the detector. The position resolution for the drift chambers was about 0.3mm [38].

Data Acquisition

The electronic signals from the detector elements were digitized by LeCroy CAMAC ADCs and TDCs. A VME processor gathered information from the various CAMAC modules and sent it through a TCP/IP network connection to a workstation for online monitoring and tape storage [45].

The typical data rate was 500kB per second and 10^7 events were stored on tape.

4 Analysis

Neutrino interactions in the emulsion were selected from the events recorded on data tapes based on their track pattern. Each neutrino-nucleon interaction generated several high-momentum charged particles that would pass through the spectrometer, producing hits in the sensitive spectrometer elements. These hits were reconstructed to find the particle trajectories that were then used to identify the interaction type and to estimate the vertex location.

This vertex estimate determined a small volume of emulsion that was subsequently scanned to locate the neutrino interaction vertex. Particle trajectories reconstructed from scan data were also used to identify the neutrino interaction type.

4.1 The Hardware Event Selection

The charged particles coming from the neutrino interaction vertex were recognized by the trigger system, which was used to select events to write to tape during the data run. The trigger requirement was that there should be no track upstream of the target region and at least two high-momentum tracks leaving the downstream end of the target region.

The requirement of no incoming track was accomplished by the veto wall upstream of the first emulsion module. The twenty photomultipliers were combined in logic OR to achieve a rejection rate for charged particles of $10^3:1$ or better.

The requirement of at least two high-momentum tracks leaving the downstream end of the target region was accomplished by an adjacency requirement in the three trigger planes T1, T2, and T3. An adjacency was defined as a hit in the center trigger plane and a hit in the

neighboring trigger counter in either the upstream or the downstream trigger plane. Figure 4-1 shows an example of an adjacency.

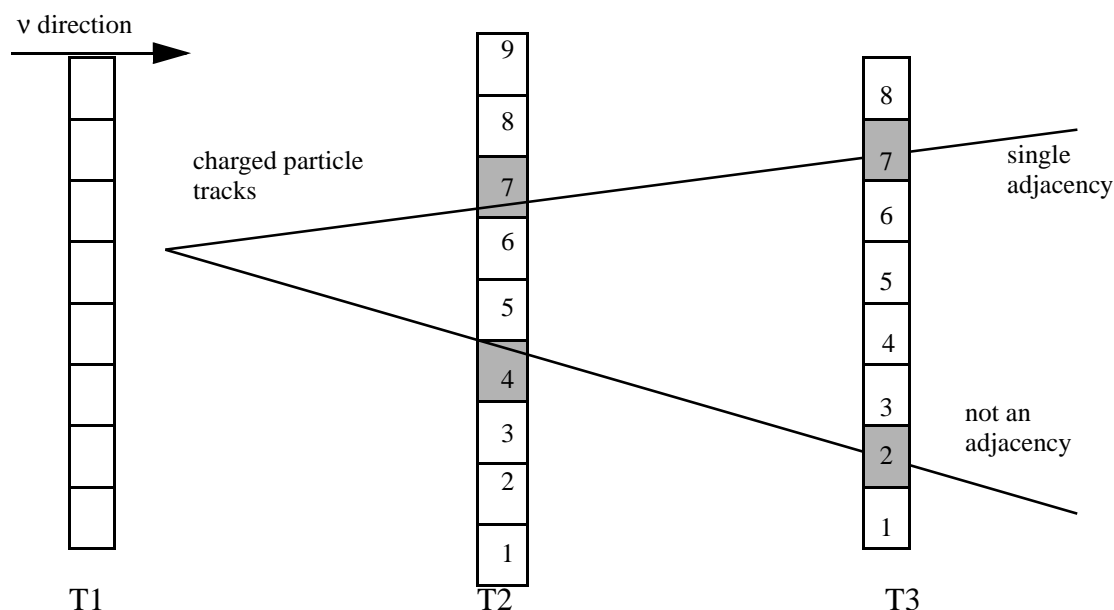


Figure 4-1. Illustration of the adjacency requirement. The figure shows only the trigger counters from figure 3-6. Two charged particles pass through the T2 and T3 trigger planes. The two trigger hits at the bottom are not next to each other and do not form an adjacency. Only the two trigger hits at the top form an adjacency.

Events satisfied the neutrino interaction requirement if they had two adjacencies, a hit in the downstream trigger plane T3, and no hits in the veto wall. This trigger condition was labeled type one, it was the basic experimental trigger and events generating this trigger type were recorded throughout the data taking period at a rate of about 3Hz.

In the later part of the experiment, events were also recorded if only a single high-momentum charged particle was produced in the emulsion that passed through the central region of the electromagnetic calorimeter. The trigger logic required only a single adjacency and a hit in the central region of the electromagnetic calorimeter. This trigger was called type two; adding it to the data stream did not change the trigger rate significantly.

Muons provide an abundant source of high momentum tracks for calibration and alignment. To produce these muons, the proton beam was directed at a target 200m upstream of the proton beam target. Interactions of protons with the target nuclei produced pions that decayed to muons and neutrinos. Pions that did not decay interacted hadronically in the

steel upstream of the emulsion target stand, whereas muons passed straight through the detector. These muon events were recorded by requiring a hit in the upstream veto wall and a hit in the trigger planes T1 and T3.

4.2 The Data Set

The DONUT experiment took data over a four-month period during the 1996-1997 fixed target run at the Fermi National Accelerator Laboratory. Both bulk and ECC type emulsion was exposed to the neutrino beam.

The Data Periods

The data were collected in four different periods distinguished by different emulsion module configurations. Bulk and ECC emulsion was mounted in the four target stations shown in figure 3-4 in different parts of the run. The run parameters for each period are shown in table 4-1.

period	1	2	3	4
# of protons on target	5.40×10^{16}	4.40×10^{16}	1.03×10^{17}	1.55×10^{17}
# of changeable sheets	4	2	6	4
number of recorded events	1×10^6	0.8×10^6	2.1×10^6	2.7×10^6
number of data tapes	79	42	90	114
total mass (kg)	492.98	557.42	589.95	549.61

Table 4-1. Number of protons on target, number of changeable sheets, and total target mass for all four target configurations. The target mass includes 292kg for the upstream lead veto wall.

The changeable sheets in the front and back of every module were exchanged about once every week. The number of protons on target includes correction factors of about 10% for detector live-time and other inefficiencies.

Table 4-2 lists the emulsion modules that were used. Only one module was made entirely of bulk sheets, and only two modules were made entirely of ECC sheets. Most of the modules had both bulk and ECC sheets.

Target module	Period	Station	ECC mass (kg)	bulk mass (kg)	total mass (kg)
ECC1	1, 2, 3	1	100.49		101.45
ECC3	1, 2	3	100.49		101.45
E/B1	4	1	49.15	19.35	69.45
E/B2	3, 4	2	42.12	25.15	66.70
E/B3	3, 4	3	44.46	21.28	66.70
E/B4	2, 3	4	36.71	27.73	67.31
B4	4	4		56.10	57.06

Table 4-2. Target configuration and module mass. ECC modules had only ECC type emulsion and bulk module had only bulk type emulsion, see section 3.2. E/B modules had ECC type emulsion in the upstream part of the module and bulk type emulsion in the downstream part of the emulsion.

4.3 Event Reconstruction

Each neutrino interaction generated many particles that passed through the spectrometer. Charged particles produced ionization in the sensitive detector elements that was recorded as a hit in the event data file. The trajectories of charged particles were reconstructed from the hit information on tape.

The Scintillating Fiber System

The optical signal from the struck scintillating fiber was amplified by the IIT chain and detected by the CCD. The total charge in each CCD pixel was digitized and recorded on tape.

Charged particle tracks in the scintillating fiber system were reconstructed from the image recorded by the CCD camera in a two step process: the charge of the CCD pixels was converted into scintillating fiber signals, which were then used to reconstruct particle trajectories.

The mapping between pixels and scintillating fibers was determined from the fiducial fiber images that were taken between data runs. This image determined the pixel coordinates of the fiducial fibers, and the pixel coordinates of every fiber were interpolated from the coordinates of the two nearest fiducial fibers. In this way, each fiber was mapped to an area on the CCD image with a diameter of about three pixels.

Although the mapping from fibers to CCD pixels was unique, the inverse determination of scintillating fiber hits from a CCD image was complicated by distortions caused by the IIT chain. The typical image size for a single scintillating fiber hit had a diameter of seven pixels and was usually not circular. This dispersion problem is discussed in detail in reference [46]. Two different methods were used to determine which fibers corresponded to a given CCD image. Both were designed to identify which fiber was struck when a single charged particle passed through a scintillating fiber plane.

The two methods can be summarized as follows: The first was based on the clustering of many pixels and assigning the total charge of the cluster to a single fiber, independent of the number of pixels in the cluster. The IIT distortions caused the image from a single scintillating fiber hit to spread out over a large number of neighboring pixels and the algorithm joined all adjacent pixels that were hit together into one cluster. Each cluster was required to have only one pixel with more charge than any of its neighbors (corresponding to a local peak). Clusters with more than one local peak were divided into smaller clusters, and each of the clusters found in this way was assigned to the scintillating fiber closest to the peak pixel.

This method decoded an average of two fiber hits each time a charged particle traversed a scintillating fiber plane. Pixel charges were assigned to the correct scintillating fiber if the track density was small, but the procedure failed to assign any charge to many of the fibers in a particle shower, and accordingly, it was mainly used in the reconstruction of charged particle tracks.

The second method assigned the charge in a 3x3 pixel square to each scintillating fiber, but only if at least seven of the pixels had a non-zero charge. This method decoded an average of 3.5 adjacent fibers each time a charged particle traversed a scintillating fiber plane. The

large number of fiber hits produced many ghost particle trajectories and hence it was not appropriate for precision track reconstruction. However, the method accurately assigned fiber hits in particle showers and was therefore mainly used to estimate the size of these showers.

Particle tracks (lines) were reconstructed in each of the two stereo views from the scintillating fiber hits. These lines were then matched to three-dimensional particle trajectories and ambiguities between several lines in one view were resolved with the help of hits in the vertical fiber planes.

Downstream Tracking

The momentum of charged particles was determined from the track vectors in the two drift chamber systems upstream and downstream of the magnet [38].

The position of a hit in the drift chambers was decoded from the signal arrival time at the drift wires and three-dimensional particle trajectories were reconstructed from these hits.

The component of the charged particle momentum parallel to the incoming neutrino beam was determined if the particle trajectory was reconstructed both upstream and downstream of the analysis magnet. A “thin lens” approximation was made where it was assumed that the particle deflection occurs in the center of the magnet. The two track segments (upstream and downstream) were projected to the magnet center and the angle α_X between them was used to determine the momentum p_Z :

$$p_Z = \frac{p_{kick}}{\sin \alpha_X}, \quad (4-1)$$

where $p_{kick} = 0.228 \text{ GeV}$ is the increase in momentum for charged particles as they pass through the magnet [39].

Due to the non-uniformity of the magnetic field, the thin lens approximation did not work well for low momentum ($< 10 \text{ GeV}$) particles. In this case, the deflection due to the magnetic field was instead found at many points along the trajectory in an iterative procedure, leading to a more accurate measurement of the momentum.

4.4 The Neutrino Data Filter

Most of the events recorded on tape were due to charged particles entering the target area from the side and not due to neutrino interactions. This background came from secondary particles produced by the large flux of muons in the steel on each side of the emulsion target stand. Muons could interact in the steel and knock out electrons and hadrons, which then entered the emulsion target area. These background events were filtered out by pattern recognition software and by interactive event scanning. These two filters were designed to accept a large fraction of the neutrino-nucleon interactions that were the main experimental focus.

Software Neutrino Event Selection

Hit information from the data tapes was analyzed to eliminate background events that were not produced by neutrinos. Requiring that one or more of the following conditions be fulfilled rejected events that contained only low energy electrons and photons ($<10\text{MeV}$) scattering in the targets:

- at least one track in the drift chambers should point back to within 0.5m of the most downstream emulsion module,
- a vertex should be reconstructed from tracks reconstructed in one view of the scintillating fiber system only, or
- a signal of at least 30GeV should be measured in the electromagnetic calorimeter.

Events were also rejected if the time difference between trigger hits in the T2 and T3 trigger planes was not consistent with a single charged particle passing through both planes.

These basic cuts reduced the number of events from 10^7 to 10^5 , the remaining events were stored in disk files (*filter* files, one file for each data tape). This was the main event sample used in the magnetic moment interaction search presented in this thesis.

Interactive Event Selection

The data set to be used in the emulsion scan to search for tau-neutrino interactions was extracted from the software selected files in a visual event analysis. Most of the events in these files had one or a few charged particle tracks that entered the target area from the side

and some of the events had large particle showers at the edge of the target area. Both of these types of background events were produced by high-momentum muons passing through the steel frame of the target stand.

Only about 1% of these events were due to neutrino-nucleon interactions. They were extracted in an interactive scan designed to accept a large fraction of neutrino interactions while rejecting background events [47]. A team of two physicists scanned each file, first separately, then together to resolve differences. An event was selected as a neutrino interaction if all of the following conditions were fulfilled:

- the event had a reconstructed vertex with at least three high-momentum tracks or a particle shower;
- the neutrino interaction vertex was in an emulsion module;
- the total event energy (estimated from the momentum of charged particle tracks and the calorimeter signal) was at least 5GeV.

A total of 828 neutrino interactions were selected in the interactive scan and the vertex position was reconstructed for each event. This data set was also analyzed in the magnetic moment search. However, the interactive event selection had large systematic uncertainties, and the sample was therefore only used to check the results obtained with the larger set of software selected events.

Vertex Prediction

In order to locate tau-neutrino interactions in the emulsion, the interaction vertex position was first determined from reconstructed spectrometer tracks. Typical neutrino-nucleon interactions in the emulsion modules produced three or more charged particle tracks that could be identified in each orientation of the scintillating fiber planes. These reconstructed tracks were used to find the most likely position of the neutrino interaction vertex in each view.

Tracks that could be reconstructed in both stereo views and matched with a hit in a vertical plane improved the vertex prediction accuracy since they were usually produced by high-momentum charged particles. An accurate vertex position prediction was important in the

analysis since it increased the probability of finding the neutrino interaction in the emulsion [48].

4.5 The Emulsion Data Analysis

The identification of tau-neutrino interaction candidate events in the main part of the DONUT experiment was based on the analysis of emulsion data. However, this information was not used in the magnetic moment search presented in this thesis.

The trajectory of charged particles is visible in the emulsion after development. Most of the particles from a neutrino-nucleon interaction travel in approximately the same direction as the neutrino. Since the emulsion sheets were oriented perpendicular to the neutrino beam, most trajectories were perpendicular to the sheet surface and the particles traveled through many sheets, producing only short track segments in each sheet. These segments were digitized in a total area of about 2mm by 2mm in each sheet, for up to twenty sheets. The position and angle of each segment was stored on disk for later analysis.

Emulsion Scanning

The track density in each emulsion sheet was approximately 2000 tracks/mm². This was too large to record each segment by hand with a microscope. An automatic emulsion scanning station, consisting of a precision table, a microscope connected to a CCD camera, and pattern recognition hardware, was used to digitize track segment information and write it to disk [39].

Each sheet of the emulsion was kept flat on the microscope stage by vacuum to avoid distortions. The scanning table was moved in steps of about 150μm, and images were taken at each position. The output of the CCD camera was digitized and stored to disk for a 200μm by 200μm field of view for 16 different depths (layers) in the sheet. A track was characterized by a continuous black mark in all the layers. This signature was then used to identify the track segment. The position and angle for each segment were stored.

Scanning an area of 2mm by 2mm on twenty sheets took ten hours, making it impossible to scan all of the emulsion. The size of the scan volume was based on the accuracy of the vertex position estimate from the spectrometer.

Emulsion Analysis

Particle trajectories in the emulsion were reconstructed from track segments found in many sheets. Most of the reconstructed trajectories were from background muons, making a determination of the vertex location difficult. However, they also provided a convenient data set for sheet-to-sheet alignment.

Two different methods were used to locate the neutrino interaction vertex in the emulsion. In one, the scan-back method, charged particle tracks that were reconstructed in the spectrometer were identified in the changeable sheet. Due to this much shorter exposure, the track density in the changeable sheets was much lower than in the emulsion modules. From the changeable sheet, the track was followed upstream from sheet to sheet in the emulsion until it stopped at the neutrino interaction vertex. The scan-back method was effective in locating the neutrino interaction vertex in events with only a few high-momentum tracks from the vertex in the scintillating fiber planes. However, the vertex in events with large particle showers was impossible to locate with this method.

In the second method, the net-scan method, a small volume of emulsion around the estimated vertex position was completely scanned and the vertex was then found from reconstructed emulsion tracks. This method was most useful for events with many tracks or particle showers coming from the vertex.

After the vertex was located, both emulsion data and spectrometer data were analyzed to identify the type of neutrino interaction and to determine interaction parameters [39].

4.6 Magnetic Moment Event Selection

Neutrino-electron magnetic moment interactions have a unique signature in the spectrometer in that a single electron is produced in the interaction that may subsequently develop into an electromagnetic shower. These interactions do not contain hadrons in the final state. Most neutrino-nucleon interactions on the other hand produce several hadrons that can be identified.

The search for neutrino-electron magnetic moment interactions was therefore designed to identify interactions that only contained electromagnetic energy. Only spectrometer data

were analyzed to find event patterns consistent with this requirement, and the emulsion information was not used in the search. The identification of a neutrino interaction in the emulsion required at least two tracks coming from the interaction vertex, and since only a single electron is produced in a neutrino-electron interaction, this type of vertex cannot be located.

Events were selected for the magnetic moment interaction sample if the first electron or the electromagnetic shower was identified. Events were removed in the selection process if they were not produced by neutrinos or if hadrons could be identified. These background interactions were produced by three major sources: neutrino-nucleon interactions in general, electron-neutrino charged-current interactions in particular, and non-neutrino background events.

Neutrino-nucleon interactions were recognized if at least one of the hadrons produced in the interaction was identified. Moreover, neutral-current neutrino-nucleon interactions and muon-neutrino charged-current interactions don't produce electrons in the interaction. These events only contain electromagnetic energy if particles (pions, muons) decay to photons or electrons. All other particles in these events are hadrons or muons, which could be identified because they have a small probability to produce a particle shower in the emulsion modules. One emulsion module corresponded to 2 radiation lengths, but only 0.2 nuclear interaction lengths. Consequently, most of the hadrons passed through the emulsion without showering, while most of the electrons started an electromagnetic shower. To illustrate this point, figure 4-2 shows the number of simulated charged particle tracks that

passed through an emulsion module without scattering by more than 0.01rad and without initiating a particle shower.

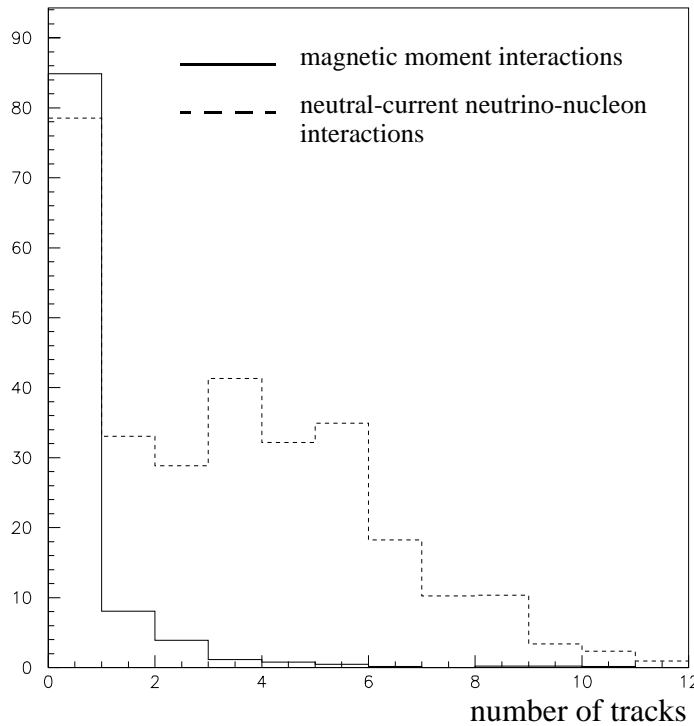


Figure 4-2. Histogram of the number of charged particle tracks per event that passed through an emulsion module without interacting. The two data sets were generated by the Monte Carlo simulation and passed the trigger and software neutrino event selection cuts.

The electrons and positrons in the electromagnetic showers of magnetic moment interactions rarely pass through an emulsion module without initiating a particle shower. The hadrons produced in a neutral-current interaction on the other hand usually pass through an emulsion module unaffected and can be identified downstream of the module. Only if the neutrino interaction occurred in station four is it not possible to identify hadrons in this fashion. The peak at zero tracks for neutral-current interactions in figure 4-2 therefore is mostly due to interactions occurring in the most downstream station.

Due to the presence of an electron in the final state of charged-current interactions of electron-neutrinos and nuclei, this class of events contributes an important source of background to the magnetic moment signal. However, the electron is typically produced with a large energy and at a large angle and the distributions of both of these parameters for elec-

tron-neutrino nucleon interactions and magnetic moment interactions are shown in figure 4-3.

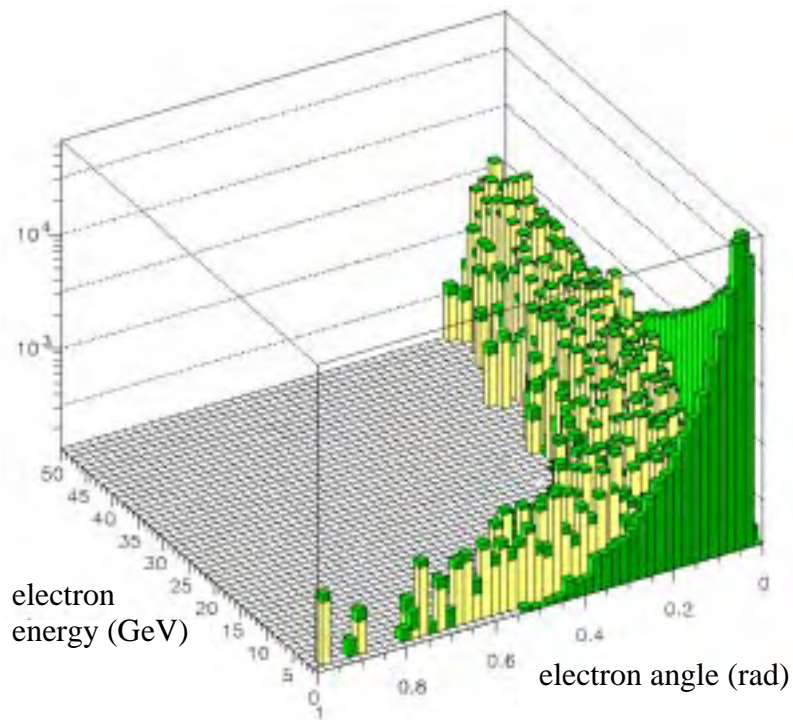


Figure 4-3. Stacked histogram of the electron energy and the angle between incoming neutrino and outgoing electron for simulated electron-neutrino-nucleon charged-current interactions (light shade) and neutrino-electron magnetic moment interactions (dark shade). The frequency is shown on a log scale.

Almost all of the entries for magnetic moment interactions are in the lowest energy and angle bin. This is also evident when comparing the projections onto the energy and angle axes shown in figure 4-4.

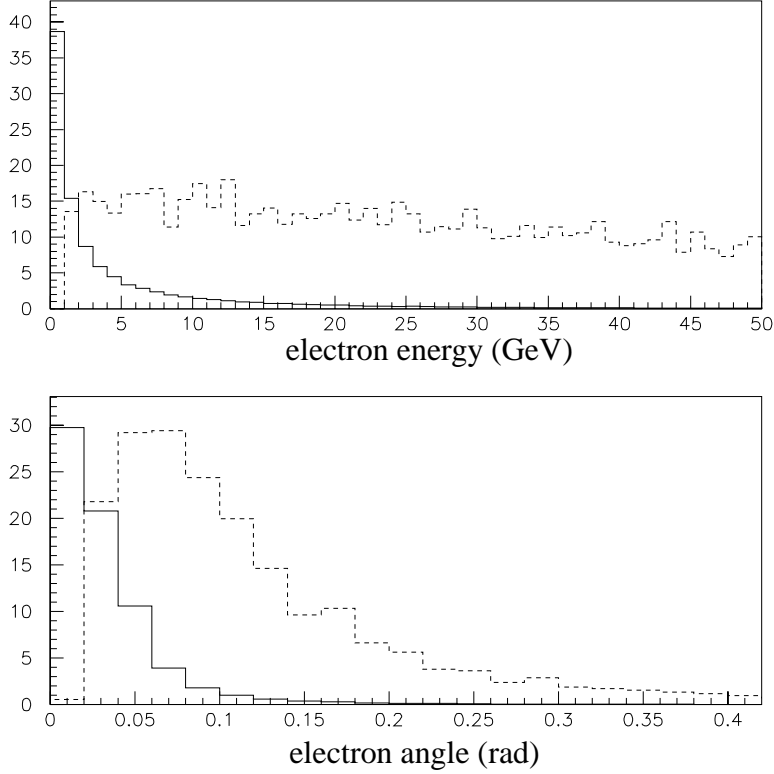


Figure 4-4. Projections from figure 4-3, i.e. comparison of energy and angle between the incoming neutrino and the scattered electron for simulated magnetic moment interactions (solid line) and simulated neutrino-nucleon charged-current interactions (dashed line).

The typical electron energy in magnetic moment interactions is below 20GeV while the typical electron energy in electron-neutrino charged-current interactions is above 20GeV. Similarly, the typical electron angle in magnetic moment interactions is below 0.1rad, whereas the typical angle in electron-neutrino charged-current interactions is larger than 0.1rad. Both energy and angle were considered when removing electron-neutrino charged-current interactions from the event sample.

The sample of events that was analyzed in this search contained a large fraction of background events that were not produced by neutrino interactions. These *filter* files contained about 10^5 events, but only approximately 1% of those were neutrino-nucleon interactions.

Moreover, some of the neutrino interaction candidate events also contained background tracks and hits. These two factors increased the complexity of the magnetic moment interaction search. Furthermore, the Monte Carlo simulation did not generate background tracks or background events. As a result, when applying the same cut to data and Monte Carlo files, the selection efficiency for neutrino interactions would be different. Some of the events that were removed in the simulation might be kept in the data. Such a situation may occur, for example, for a cut that required a minimum measured energy in the calorimeter. If background photons hit the calorimeter and increased the measured energy in the data, more events would be removed from the Monte Carlo than from the data. Consequently, the selection efficiency for data events would be higher than the value obtained in the analysis of Monte Carlo events.

Conversely, some of the events removed in the data might be kept in the simulation. This situation may occur, for example, if a cut required that all reconstructed tracks were connected to the vertex. Since some of the data events contained reconstructed background tracks in addition to the vertex tracks, more events would be removed from the data than from the Monte Carlo. Consequently, the selection efficiency for data events would be lower than the value obtained in the analysis of Monte Carlo events.

This implies that the results for the selection efficiencies obtained from the analysis of Monte Carlo events could not be used directly in the data analysis. The problem was resolved by tuning each cut with real and well-understood data and by normalizing it between Monte Carlo and data. Two sets of control events were used for this purpose, and each set contained two samples: one from the data and one from the Monte Carlo. The events in each set were selected with methods that were insensitive to the background processes mentioned above, and thus the same selection criteria were used for data and Monte Carlo events. The selection of these control events is described in detail in appendix B.

The first set consisted of muon-neutrino-nucleon charged-current interactions, which were easily identified in the data because the muon produced in the interaction could be reconstructed in the muon ID system with high efficiency. Moreover, the simple requirement of a reconstructed muon track that originated in the emulsion modules made this sample

essentially background free. These events are well understood and their parameters (muon momentum, vertex position distribution, vertex track multiplicity, etc.) were reproduced accurately by the simulation.

The second set of control samples consisted of electromagnetic showers produced in the interaction of high-energy muons with target electrons. These “knock-on electron” events were extracted from the muon calibration sample and they were used to check the effect of the selection cuts on electrons. Each of these events contained a reconstructed muon that produced an electromagnetic shower in the emulsion modules. These two simple requirements assured that this data sample was free of background interactions that did not contain electromagnetic showers. The Monte Carlo sample of the second set consisted of magnetic moment interactions. Since the spectrum of electron energies produced by these neutrino-electron interactions is similar to the electron-energy spectrum of the knock-on electrons, they could be compared directly for each selection cut.

Before the selection cuts were applied to the full set of data events (10^5) that passed the first software selection, the cut parameters were defined based on the analysis of simulated magnetic moment interactions. Then the parameters were tuned using the two data control samples to account for background processes. The cut parameters were usually tuned until the cut removed the same fraction of events from the data and Monte Carlo sample in each set. The cuts were applied to the full data set only after all parameters were fixed. This analysis method is “blind” in the sense that the cut was first defined and then applied to the data without any further modification.

The following procedure was followed to determine the parameters of each cut:

1. The cut was applied to the magnetic moment event sample and the neutrino-nucleon interaction samples that had passed all of the previous cuts. The specific cut parameters were adjusted to remove a large fraction of the neutrino-nucleon interaction sample while keeping a large fraction of the magnetic moment sample. The selection efficiencies thus obtained were used in the analysis.
2. The cut was then applied to simulated ν_μ charged-current events (set 1). Each cut was applied to the full sample to get the largest statistical significance possible. The selection efficiency thus obtained was then used to tune the cut parameters for the data.

3. The cut was then applied to ν_μ charged-current events in the data, once again to the full sample. If necessary, the parameters of the cut were tuned until the selection efficiency was identical to that obtained in the Monte Carlo analysis of step 2. Consequently, the cut parameters varied between data and Monte Carlo for some of the events. This occurred most notably in cuts that primarily removed non-neutrino interactions because the simulation did not generate such interactions.
4. The cut was then checked by applying it to the data sample of electromagnetic showers in set two and to the full magnetic moment event sample. If the difference in selection efficiency between the two was larger than the statistical uncertainty, the cut was removed from the analysis process altogether. Such a situation could occur if the electromagnetic shower development was different between data and Monte Carlo. Only cuts that were insensitive to such differences were used in the analysis.
5. The cut was then applied to the data sample that had passed all previous cuts, using the parameters for data events determined in step 3.

Due to the large number of background events in the full data set, most of the events remaining even after the third step of the software selection were not produced by neutrino interactions. The remaining background events were filtered out in an interactive event analysis in which the neutrino interaction vertex was also reconstructed. The efficiencies for this step were also determined by analyzing the control event sample.

Step One

In the first pass through the data, events were removed from the data set if they were unambiguously identified as coming from background interactions or from neutrino nucleon interactions. Neutrino-nucleon interactions with reconstructed hadrons and muons as well as electron neutrino-nucleon interactions that produced a lot of electromagnetic energy were removed.

Muon and Hadron Identification

The tracking stations downstream of the analysis magnet were used to identify hadrons and muons. These particles typically penetrated the calorimeter and produced hits in the six sensitive planes of the muon ID system.

Particle trajectories were at first reconstructed from the drift chamber hits only. If a muon ID hit was found within a distance of 1cm to the trajectory, it was associated with the track. Two features therefore characterized a muon track:

1. It was typically associated with hits in each plane of the muon ID system (six planes total).
2. The signal in the lead glass corresponding to this track was smaller than 0.5GeV.

High-momentum hadrons also had a high probability of passing through the lead glass and the first wall of muon ID steel. Such a hadron also produced only a small signal in the lead glass and its reconstructed trajectory was also associated with hits in the muon ID system.

A histogram of the number of hits in the muon ID system associated with reconstructed tracks for period four data is shown in figure 4-5.

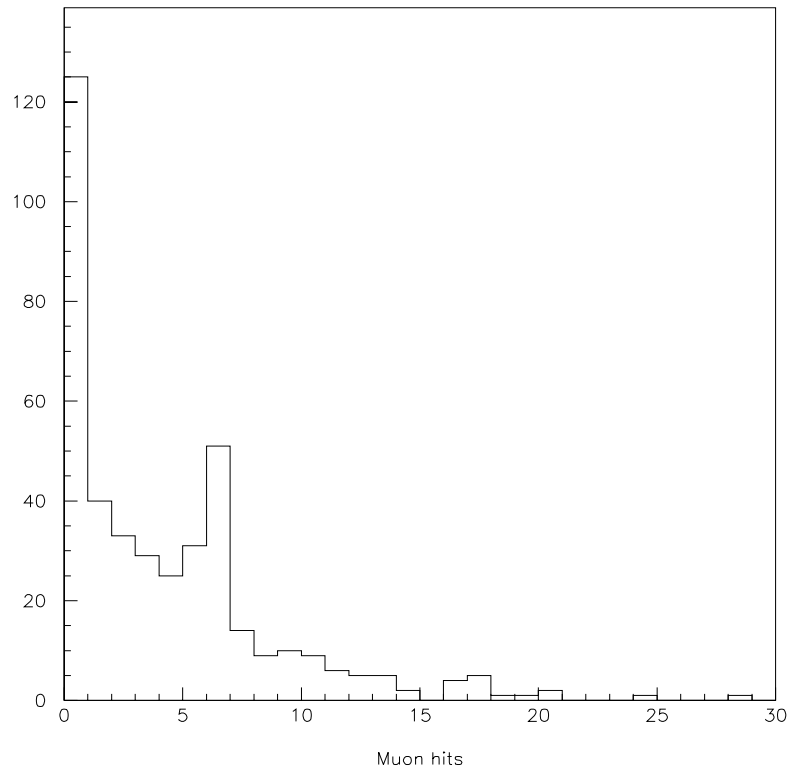


Figure 4-5. Muon hits for reconstructed tracks for period 4 neutrino candidates.

The data sample consists of events that were selected in the visual selection process described in section 4.4. The peak at a value of six indicates that muons from muon neutrino

charged-current interactions were reconstructed correctly. However, since the data sample also contained charged-current and neutral-current interactions from all neutrino flavors, a large fraction of the events had no muon ID hits, and some of the events had more than six hits.

Figure 4-6 shows the same histogram for a Monte Carlo file with muon neutrino charged-current interactions. Once again, most of the muons were reconstructed correctly, producing a peak at a value of six hits. The tail at higher values was produced by other tracks also entering the muon ID in the same event, while the peak at zero was produced by large-angle muons that didn't pass through the muon ID system.

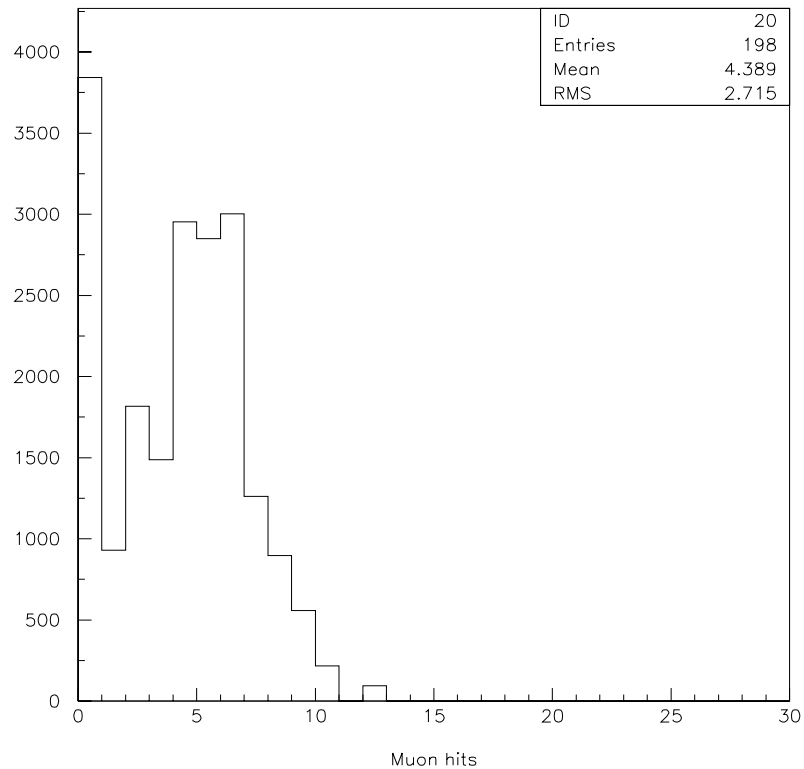


Figure 4-6. Number of muon ID hits for reconstructed tracks for Monte Carlo muon neutrino charged-current interactions only.

In contrast to neutrino-nucleon interactions, tracks reconstructed from magnetic moment events had no muon ID hits because electrons deposited all of their energy in the lead glass and didn't reach the muon ID planes. Events that had a track with a muon ID hit were therefore rejected. In the analysis of data files, this requirement was too strict because of the

large number of noise hits in and the inefficiency of the muon ID system. Events were only rejected if they had more than one muon ID hit associated with a reconstructed track.

The electromagnetic calorimeter was also used for particle identification. Electrons lose almost all of their energy in the lead glass whereas muons pass through the calorimeter and only lose energy through ionization. The average ionization generated by a muon corresponded to a signal of about 0.5GeV [44].

Events were rejected if they had a reconstructed track with a momentum of more than 4GeV and an energy signal of less than half of the momentum in the electromagnetic calorimeter. Events that were misidentified and removed from the magnetic moment sample had a track that was not reconstructed correctly in the drift chambers and the measured momentum was larger than the true particle momentum.

This cut removed about 15% of the events in the data sample and less than 10% of the Monte Carlo magnetic moment events.

ν_e -nucleon Interactions

The energy transferred to the electron in a simulated ν_e -nucleon charged current interaction was typically larger than 20GeV and the distribution was very wide, as shown in figure 4-4. By contrast, the simulated magnetic moment interactions typically had momentum transfers between the neutrino and the target electron of less than 10GeV. Consequently, the total energy measured in the electromagnetic calorimeter was much lower in magnetic moment interactions than in neutrino-nucleon interactions.

Events were therefore rejected if they had a total measured energy signal of more than 20GeV in the electromagnetic calorimeter. The cut was only applied in periods three and four since in these run periods the calorimeter performance was suitable for physics analysis.

This cut removed about 5% of the remaining data events in periods three and four and about 3% of the remaining Monte Carlo magnetic moment events. It also removed about half of the remaining Monte Carlo ν_e -nucleon charged-current interactions.

Vertex Track Reconstruction

As was shown in figure 4-3, the recoiling electron from a neutrino-electron interaction travels almost parallel to the neutrino direction. It typically produces an electromagnetic shower as it passes through material, and the shower particles also travel at a small angle with respect to the original electron.

All possible combinations of reconstructed trajectories in the two scintillating fiber views were combined to three-dimensional tracks. If any of these tracks had an angle of less than 0.1rad with respect to the neutrino direction, the vertex was positioned at the upstream end of this track. Events in which no such tracks could be reconstructed were rejected.

This cut removed about 80% of the remaining events in the data sample but only 20% of the remaining events in the simulated magnetic moment sample.

Tracks Showering in an Emulsion Module

As discussed above, most hadrons passed through the emulsion modules without scattering or showering. By contrast, electrons generated electromagnetic showers. If the electron energy was larger than about 0.5GeV , the shower could be recognized downstream of the next emulsion module. However, if the electron energy was small or the electron angle larger than about 0.2rad , the shower particles would stop in the emulsion and no particle tracks would be reconstructed downstream of the next emulsion module. Therefore, particle tracks that were reconstructed both upstream and downstream of an emulsion module could be identified as hadrons.

Accordingly, events were rejected if at least one such hadronic particle trajectory with an angle larger than 0.2rad with respect to the neutrino direction was found.

This cut removed about 10% of the remaining data events and 3% of the remaining Monte Carlo magnetic moment events.

Altogether, the cuts in step one removed 90% of the data events while keeping 70% of the Monte Carlo magnetic moment events. About 10000 events were remaining in the data sample after step one. A summary of the analysis of the control events is given at the end of step two.

Step Two

In this step, background interactions due to particles that entered the emulsion target region from the side were removed. Most of these interactions were caused by the scattering of muons as they passed by the target region. These scatters occurred in the target stand and in the lead surrounding the target region (see figure 3-7).

The second scintillating fiber decoding method was used in this step because it gave more accurate information about the amount of ionization that was produced in the scintillating fiber.

Out-of-Time Events

A histogram of the scintillating fiber signal produced by a minimum-ionizing particle is shown in figure 4-7.

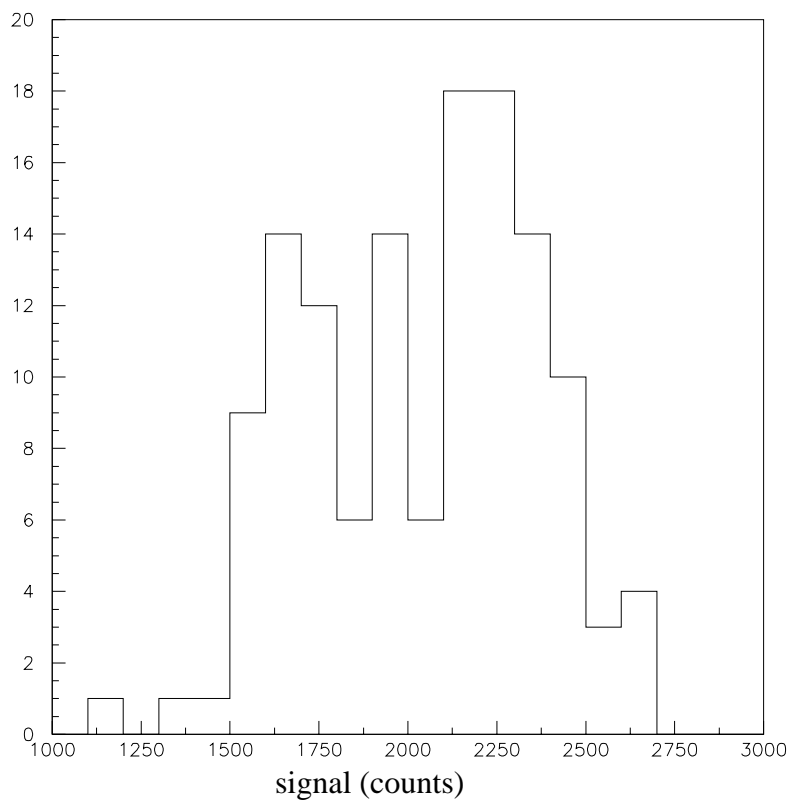


Figure 4-7. Histogram of the average scintillating fiber signal per event in the data control sample of period four.

In some of the data events, the average pulseheight for all tracks is significantly lower than the mean of the histogram in figure 4-7. These events were produced when two particles passed through the spectrometer at different times. For example, a muon could pass through the spectrometer and interact with a target electron or nucleon, which then produced a particle shower. A few microseconds later, a second particle generated hits that satisfied the trigger condition. In this case, the original shower would not be recorded if the muon was identified in the upstream veto wall. However, due to the decay time of the phosphor screens in the image intensifier modules, it would still be visible at the time the second particle produced trigger hits. At that time, the original shower would be recorded by the CCD, although only with a small signal.

Events were rejected if the average signal in the scintillating fibers was below 1500 counts, which is two standard deviations below the mean event energy for the control events.

This cut removed 5% of the remaining events in the data sample and 2% of the remaining events in the Monte Carlo magnetic moment sample.

Vertex Location

Many of the reconstructed vertex locations from step one were at the edge of the emulsion modules. Figure 4-8 shows their distribution together with the outline of a module.

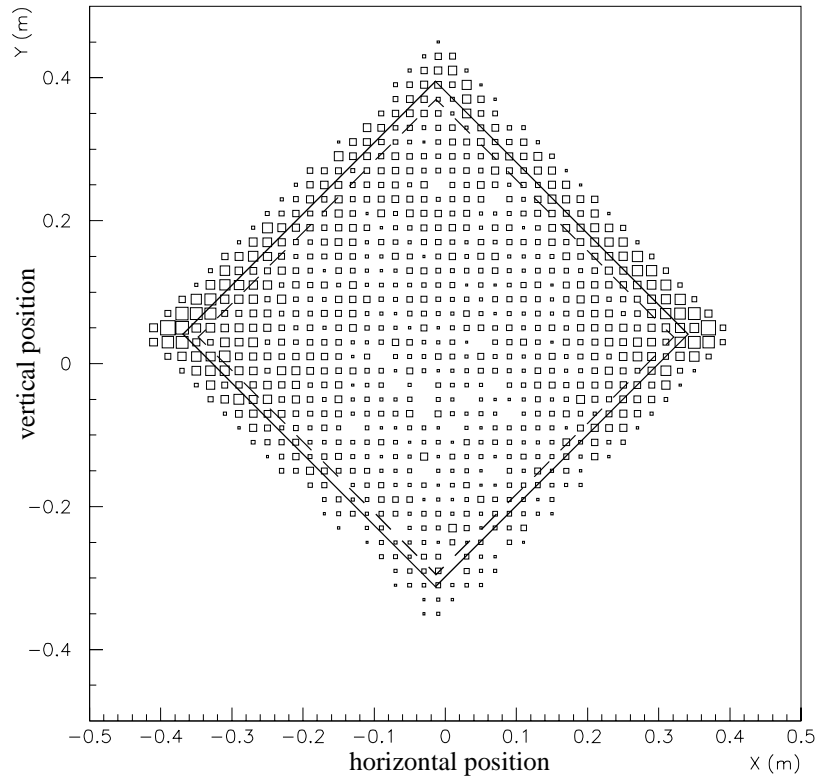


Figure 4-8. Distribution of reconstructed vertex positions in the remaining data events. The solid line shows the location of the 0.5m wide emulsion modules. The dashed line shows the cut region. A large square means a large number of vertices are at that location.

Most of the reconstructed vertex positions are at the left and right hand side. Also, more reconstructed vertices occurred at the top than at the bottom. These events occurred in the steel and the shielding surrounding the target region. Since the lead shield is installed on top of the target region but not underneath, more background tracks were produced near the top. Most of the background tracks were produced on the sides by interactions of the high-energy muons.

Events were rejected if the reconstructed vertex position was outside of the dashed line in figure 4-8, which corresponds to 15% of the surface area of the emulsion modules.

This fiducial volume cut removed about 40% of the remaining data events and 15% of the remaining magnetic moment events.

Backward Trigger

Some of the data events showed a pattern of trigger hits as shown in figure 4-9. Two adjacent trigger counters were hit in T2, and only one trigger counter was hit in T3.

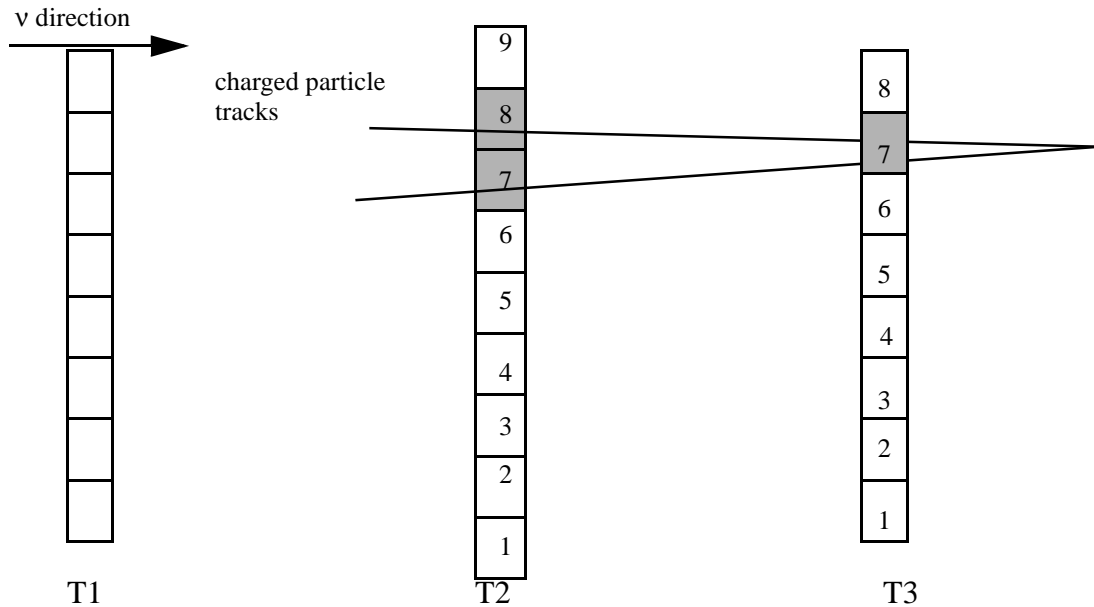


Figure 4-9. Illustration of a backward adjacency. The figure shows only the trigger counters from figure 3-6. Two charged particles pass through the T2 and T3 trigger planes. The hits are consistent with a particle shower that started downstream of T3.

The pattern corresponds to two adjacencies as defined in section 4.1 that share a common hit in T3. Most of these “backward” adjacencies were produced when a high-energy muon interacted with a nucleon of the steel of the analysis magnet and produced a particle shower. Some of these particles then traveled upstream and generated a single trigger hit in T3 and several trigger hits in T2.

Events were rejected if they had a backward adjacency as shown in figure 4-9 and no additional trigger hits.

This cut removed about 20% of the remaining data events and 4% of the remaining Monte Carlo magnetic moment events.

Trigger Hit Downstream of the Vertex

Since the direction of the electromagnetic shower produced in a magnetic moment interaction is parallel to the neutrino beam, the trigger counters downstream of the interaction vertex should be hit by many charged particles.

Figure 4-10 shows an example of a background data event in which a vertex and a small-angle track were reconstructed. However, the track could not be an electron since it did not generate any trigger hits downstream of the next emulsion module.

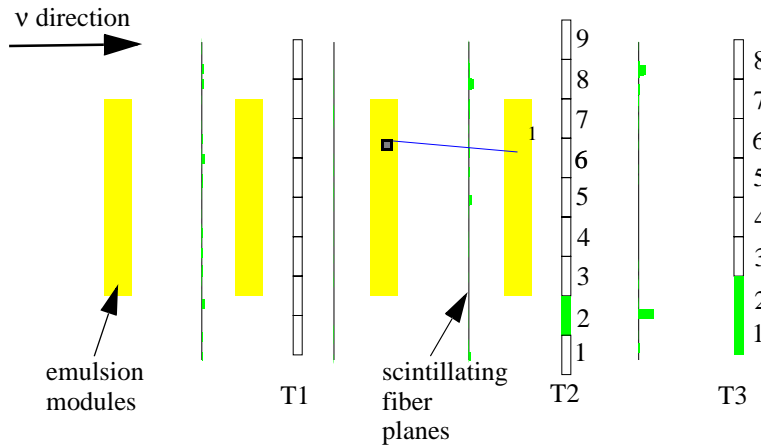


Figure 4-10. View of the target region for an event in which the reconstructed electron track did not produce a shower downstream of the next emulsion module. The vertex is shown as a small box and the track is shown as a line starting at the vertex. Filled boxes depict trigger counters that were hit.

These events were produced when a particle entered the target region from one side and scattered in the emulsion module so that the reconstructed track was almost parallel to the neutrino beam. At the same time, other particles entered the target region from the other side and generate trigger hits that satisfied the trigger requirement.

These events were rejected by requiring that at least one of the three trigger counters closest to the neutrino interaction vertex were hit, in the trigger planes downstream of the interaction. In figure 4-10, this would correspond to at least one hit in the T2 counters 5, 6, or 7, and at least one hit in the T3 counters 5, 6, or 7.

This cut removed about 25% of the remaining data events and about 5% of the remaining Monte Carlo magnetic moment events.

Slow Hadron Identification

Some of the reconstructed tracks showed large signals in the scintillating fiber system. These were produced by non-relativistic hadrons, pions, and muons that are strongly ionizing. They were often produced in neutrino-nucleon interactions and in some background interactions in which slow protons entered the target region.

The mean rate of ionization energy loss is described by the Bethe-Bloch equation [14], which gives the energy loss (dE/dx) dependence on macroscopic variables describing the material:

$$\frac{dE}{dx} = Kz^2 \frac{Z}{A} \frac{1}{\beta^2} \left[\frac{1}{2} \ln \left(\frac{2m_e c^2 \beta^2 \gamma^2 T_{max}}{I^2} \right) - \beta^2 - \frac{\delta}{2} \right]. \quad (4-2)$$

Here $\frac{K}{A} = 0.307 \text{ MeV g}^{-1} \text{ cm}^2$, z is the charge number of the incident particle, Z is the atomic number of the medium, and I its mean excitation energy. The particle speed β is in units of speed of light (c) and γ is the relativistic factor. The mass of the electron is given by m_e and δ denotes a small density effect correction that will be ignored. The maximum kinetic energy that can be transferred to an electron in a collision is given by T_{max} and can be calculated as

$$T_{max} = 2m_e c^2 \beta^2 \gamma^2 \quad (4-3)$$

in the low energy limit $2\gamma(m_e/M) \ll 1$.

The functional behavior of equation 4-2 can be seen in figure 4-11.

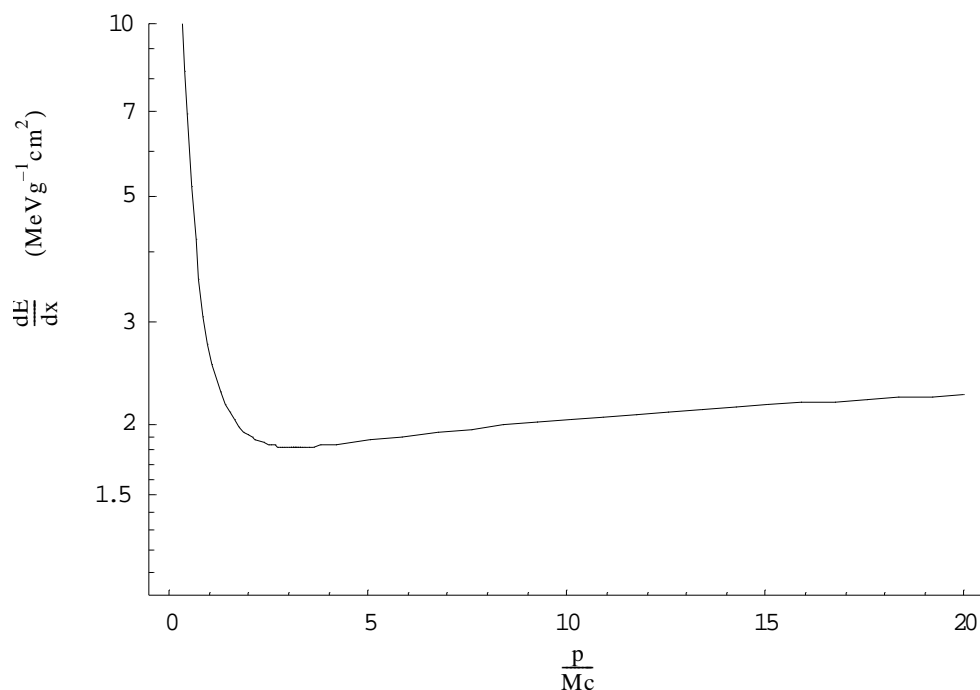


Figure 4-11. Bethe-Bloch formula for energy loss in plastic scintillator.

The ionization energy loss decreases sharply until it reaches a broad minimum, at a particle momentum that is about twice the mass of the particle. For a higher momentum, the energy loss is almost independent of the particle momentum. Figure 4-11 is valid for muons, pions, and charged hadrons. Since only non-relativistic particles are heavily ionizing, the size of the scintillating fiber signal can be used to identify them.

Events were therefore rejected if they had a large angle, large signal track behind one of the emulsion modules in one SF view. A large signal corresponded to at least five times the signal produced by a minimum ionizing particle. A large angle corresponded to an angle of at least 0.2rad with respect to the direction of the neutrino beam.

This cut removed about 4% of the remaining data events and about 3% of the remaining Monte Carlo magnetic moment events, mostly due to statistical fluctuations that generated large scintillating fiber signals for a few tracks.

Altogether, the step two cuts removed about 80% of the data events, keeping 2700 events total. Only 25% of the Monte Carlo magnetic moment events were removed in this step.

Figure 4-12 shows a summary of the analysis of the control event sets.

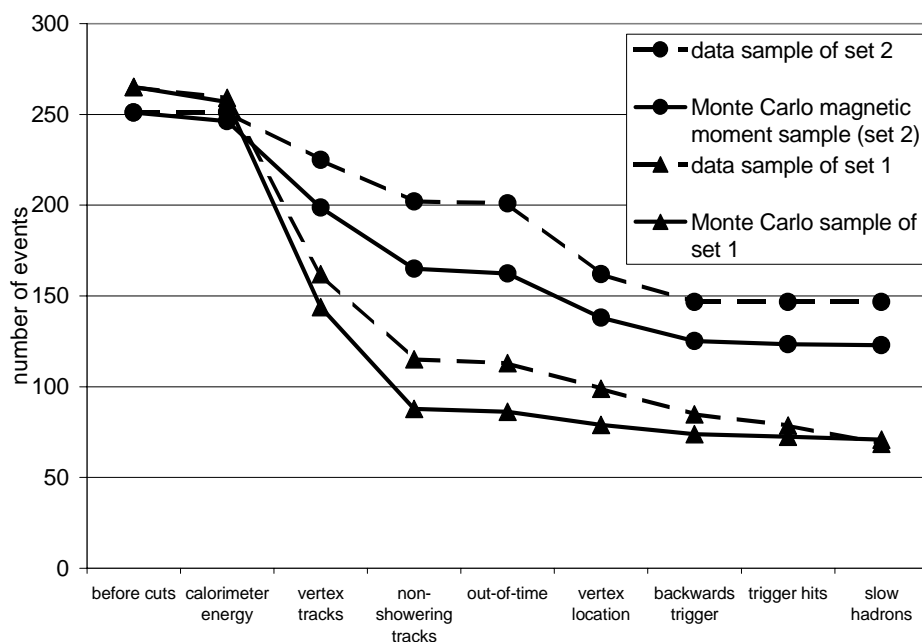


Figure 4-12. Number of events remaining in the four control samples after each of the step one and step two cuts. The two lower lines (triangles) are for control set one of ν_μ charged-current interactions and the two upper lines (circles) are for control set two of electromagnetic showers. Each line starts at the number of events remaining after the software selection.

The two curves for set one (neutrino interactions with a reconstructed muon) follow each other closely; they agree within statistical uncertainty. The two curves for set two (events with electromagnetic showers) show a difference that is larger than the statistical uncertainty. This behavior is expected since the two samples are not identical. Nevertheless, both show the same tendencies for most of the cuts.

Step Three

Most of the events that remained after step two were produced by neutral-current interactions and background events in which particles entered the target region from the side. They contained only a few tracks and small showers, but not many high-momentum particles.

These background interactions were removed by analyzing the reconstructed lines and tracks in the scintillating fiber system. As they had low track multiplicity, the first scintillating fiber decoder method was used to obtain accurate hit position information. The parameters for each cut were adjusted until the cut removed the same fraction of events from the data and Monte Carlo control samples.

Tracks not connected to the Vertex

In some of the remaining events, most of the reconstructed tracks were not connected to the vertex that was found in step one by searching for tracks that were parallel to the neutrino direction. Most events furthermore contained tracks that entered the target region from the side. Figure 4-13 shows an example of such an event.

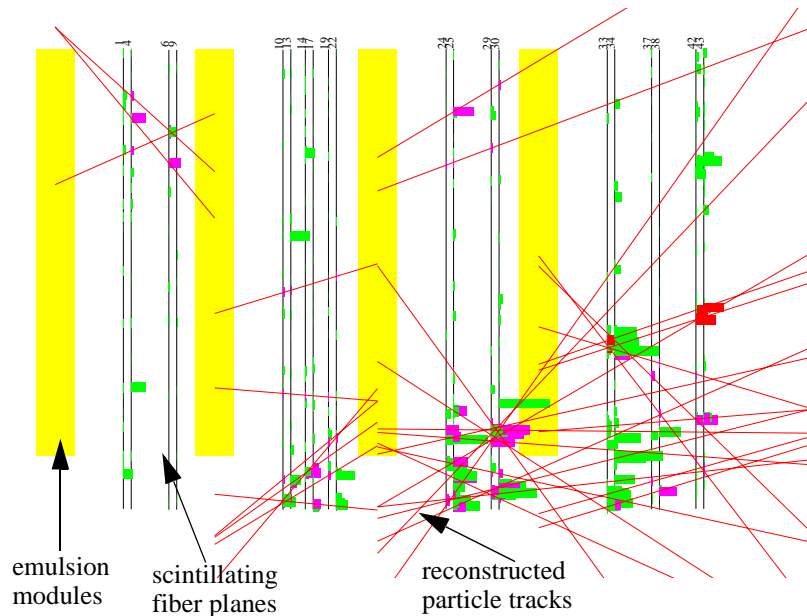


Figure 4-13. View of the target region for a background event in which many tracks are coming from the side (the bottom of the figure).

Several reconstructed particle tracks seem to originate in the bottom of the figure, which means they entered the target region from the side. This event was probably produced by the interaction of a muon in the shielding surrounding the target stand. Some of the particles produced in the interaction entered the target region and produced more particle showers.

The distinction between tracks that are coming from the side and tracks that are starting in the emulsion is based on the impact parameter of the track to the center of the next emulsion module upstream. The tracks were divided into two groups that separated background tracks from neutrino interaction tracks:

1. If the impact parameter was more than 0.24m, the track was coming from the outside. This means that the track originated outside of the area defined by the vertex cut in figure 4-8.
2. If the impact parameter was smaller than 0.24m, the track was coming from the center.

Events were rejected if there were more than a factor of three more tracks in group (1) than in group (2). They were also rejected if at least a factor of two more tracks were coming from one side than from the other.

Figure 4-14 shows two views of a background event in which the reconstructed tracks were not connected to the vertex.

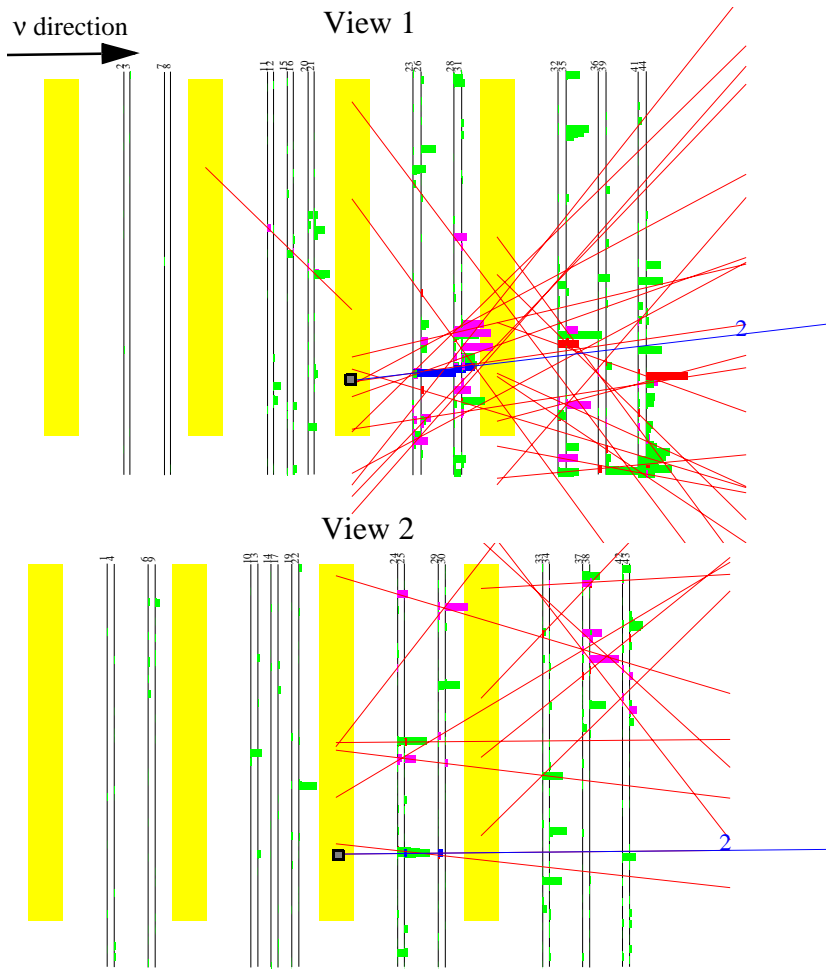


Figure 4-14. Two orthogonal views of a background event. The reconstructed vertex is shown as a small shaded box.

View one of the figure appears to show a particle shower that starts near the reconstructed vertex location. By contrast, only one or two tracks appear to be connected to the vertex in view two. Most of the tracks in this view appear to have a different origin.

Such an event could be produced when several muons pass by the target region at the same time, producing charged particles that entered the target region from both sides.

These events were removed by requiring that most of the reconstructed tracks were connected to the vertex. Events were rejected if the average impact parameter between the

tracks and the vertex was more than 0.2m. This average distance was found for tracks reconstructed behind all emulsion modules upstream of (and including) the vertex module. This cut removed about 50% of the remaining data events and 5% of the remaining Monte Carlo magnetic moment events.

Reconstructed tracks in only one View

Some of the events had many scintillating fiber hits in one orientation and few in the other. The situation is shown in figure 4-15.

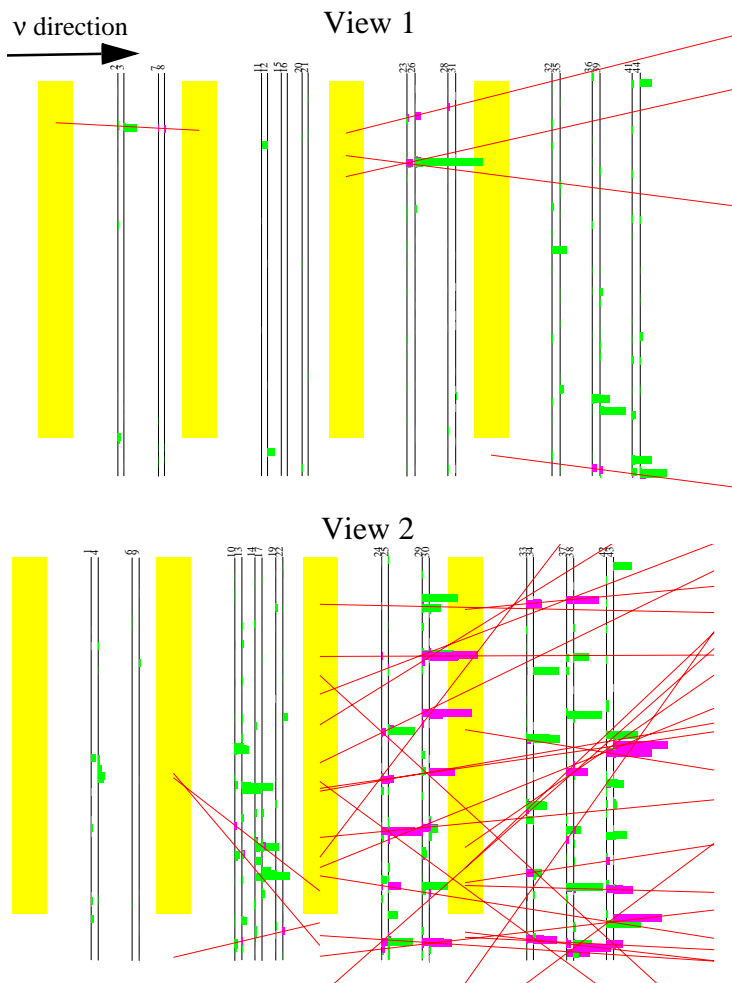


Figure 4-15. Two orthogonal views of a background event.

View one only has a few scintillating fiber hits that were reconstructed to five tracks. View two by contrast has many reconstructed tracks.

This hit pattern can be explained by an instrumental effect. It occurred when charged particles passed through the readout end of the scintillating fiber planes in one orientation and not at all through the planes of the other orientation. The situation is depicted in figure 4-16.

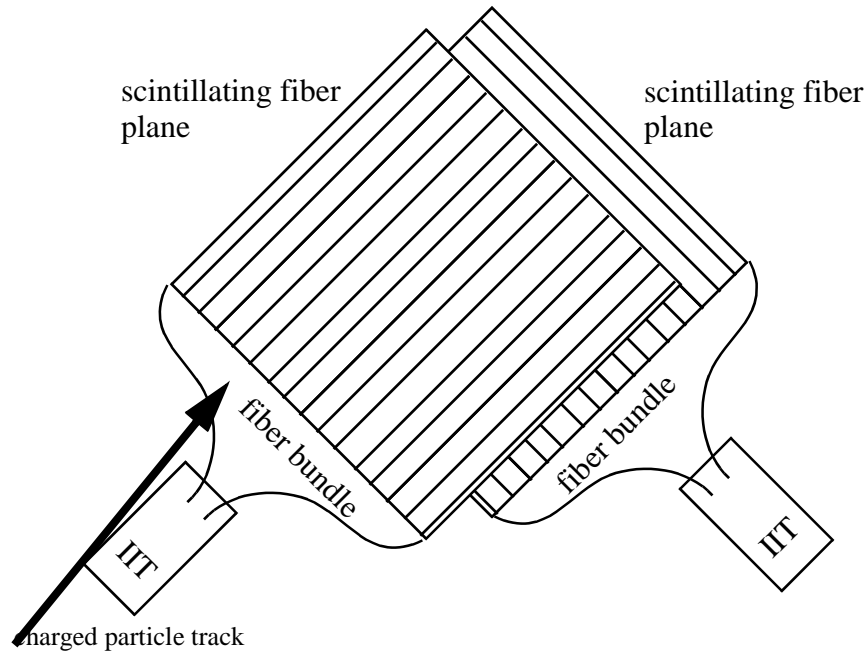


Figure 4-16. Example of a charged particle track crossing the readout end of a plane. The particle does not pass through the plane of opposite orientation.

The charged particle passed through the readout end of all planes in one orientation and did not pass through any of the planes of the opposite orientation. This situation occurred frequently when charged particles were produced near the lower edge of the target region.

In the analysis of the data sample, events were rejected if the number of reconstructed tracks in one view was less than 8% of the number of reconstructed tracks in the other view.

This cut removed about 9% of the remaining events in the data sample and about 15% of the remaining events in the Monte Carlo magnetic moment sample.

No Tracks downstream of the Vertex

Some of the events show a reconstructed track pattern in the scintillating fiber system as shown in figure 4-17.

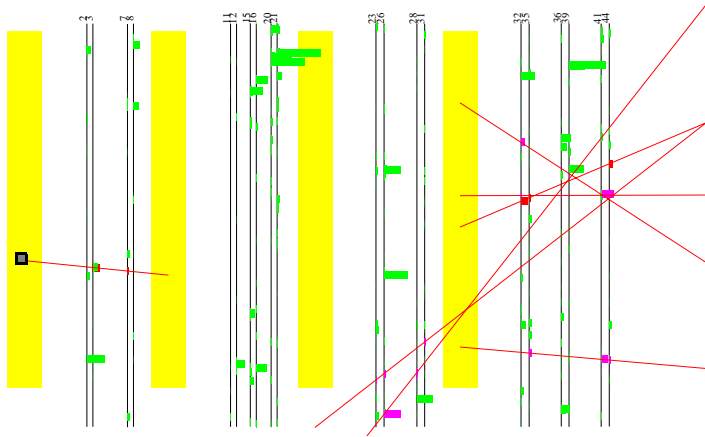


Figure 4-17. Target region view of an event with no reconstructed tracks behind the next module downstream of the vertex, shown as a small shaded box.

One reconstructed track was parallel to the neutrino beam, but it did not generate a visible particle shower behind the next module downstream. Other tracks were reconstructed at the downstream end of the target region. These particles satisfied the trigger requirement and the previous cuts, and the upstream track was probably unrelated and may have been misidentified.

The electron from a magnetic moment interaction typically produces an electromagnetic shower as it passes through the emulsion modules and most of the energy in the shower is located in a cone along the direction of the neutrino. The event shown in figure 4-17 is most likely not a magnetic moment interaction because no such electromagnetic shower has been reconstructed. It was most likely produced by muons interacting in the steel of the target frame.

Events were therefore rejected if they did not have reconstructed tracks in each view behind each module downstream of the vertex. The tracks were required to have an impact parameter of less than 0.02m to the vertex position. If the interaction occurred upstream of station two, the distance cut was increased to 0.024m to account for large particle showers. This

cut removed about 30% from the remaining data events and about 3% of the remaining Monte Carlo magnetic moment interactions.

Track Angles

Most of the reconstructed tracks in some of the remaining events do not point back to the emulsion modules; instead they appear to come from the side. This type of event pattern is shown in figures 4-13 and 4-17. These reconstructed tracks have similar angles, but those angles are large with respect to the neutrino beam, and they all appear to come from the same side.

Tracks in electromagnetic showers produced by magnetic moment interactions are typically parallel to the neutrino direction, and their average angle is also similar to the neutrino angle. The reconstructed tracks that appear to be coming from the side were most likely produced by muon interactions in the steel of the target frame. The charged particles produced in these background interactions entered the target area from the side and were correctly reconstructed.

Events were therefore rejected if the average angle for all reconstructed tracks was larger than 0.3rad . This condition was tested in both scintillating fiber views behind all emulsion modules.

This cut removed about 25% of the remaining data events, and about 7% of the remaining Monte Carlo magnetic moment events.

Of the 2000 data events remaining after step two, only 245 were remaining after step three. Nevertheless, about 60% of the Monte Carlo events remaining after step two passed all of the step three cuts.

Figure 4-18 shows a summary of the step three analysis of the control events.

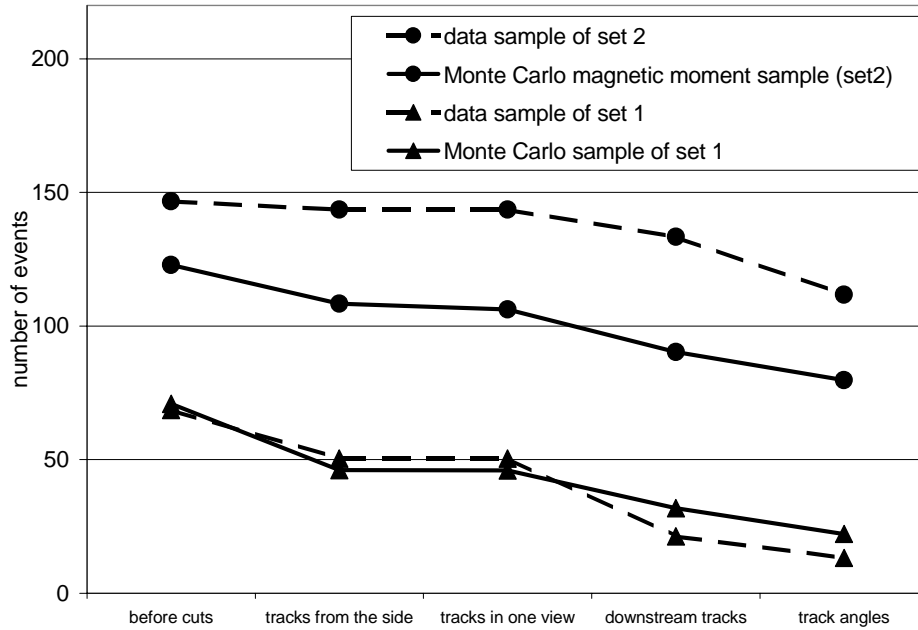


Figure 4-18. Number of events remaining in the control samples after each of the step three cuts. The two lower lines (triangles) are for control set one of ν_μ charged-current interactions and the two upper lines (circles) are for control set two of electromagnetic showers. Each line starts at the number of events remaining after step two.

The analysis of the neutrino interaction samples (set one) shows no significant difference between data and Monte Carlo, the small variations are consistent with statistical fluctuations. The two samples with electromagnetic showers (set two) show a difference that resulted from the previous selection cuts. More events remained in the data control sample than in the magnetic moment Monte Carlo sample, indicating that the selection efficiency for magnetic moment events might be larger than calculated. However, the two samples were not produced by the same process. Moreover, the data sample also contained a muon in each event, which could cause the observed increase in efficiency for data events. Hence, the difference in selection efficiency is consistent with expectation. Moreover, none of the cuts removed a considerable fraction of events from the electromagnetic shower samples, indicating that systematic effects have been accounted for correctly.

Step Four

The pattern recognition cuts from step three rejected most of the background interactions, but not all of them. The remaining background events were removed in an interactive event selection. The criteria for event selection were determined in an analysis of the control events and of events that were removed by the previous cuts.

Muon Identification

Some of the background interactions contained tracks that passed through all of the emulsion modules without scattering or producing a particle shower. Figure 4-19 shows an example of such an event.

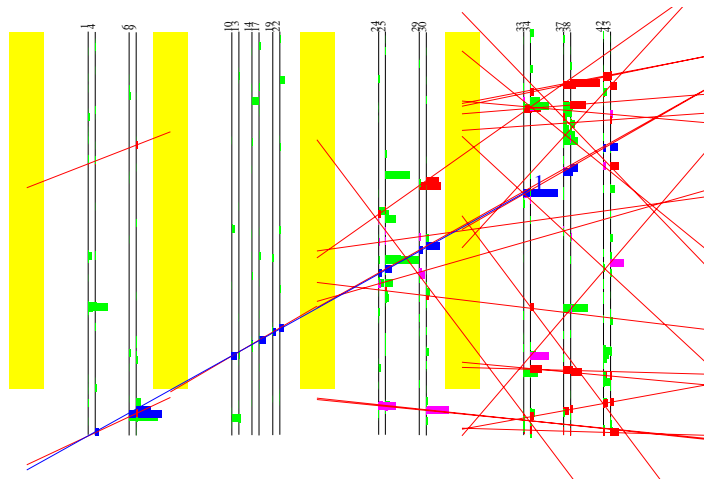


Figure 4-19. Target region view of an event with a long particle track that was found in the interactive analysis (dark line).

These events were most likely produced when muons scattered in the steel of the target stand or in the shielding and passed through the target region. This situation may also occur if the veto wall did not register a penetrating muon. Although the veto wall efficiency for these muons was better than 99%, the large number of muons produced in the proton beam target yielded a few events in which the muon was not registered.

These muons were usually identified because they passed straight through all of the emulsion modules and the track was reconstructed in the interactive analysis. Although the hadron identification in step two used a similar cut, it required that the track angle was larger than 0.2rad and failed to recognize these events.

Events were therefore rejected if a single penetrating track was recognized in at least one of the two scintillating fiber views. This cut removed about 30% of the remaining data events.

Out-of-Time Events

Some of the background interactions were produced by two or more independent processes. The charged particles that generated the detector hits in this type of event were unrelated and the hits were produced at different times.

The time of each hit was recorded for all trigger planes, and the time difference between trigger hits in trigger planes two and three has already been used to select events for the pass 1 file. If the neutrino interaction occurred in a module upstream of trigger plane one (upstream of emulsion module three), then the time difference between hits in T1 and T3 should also be consistent with a straight particle track. Figure 4-20 shows a histogram of this time difference for single muons.

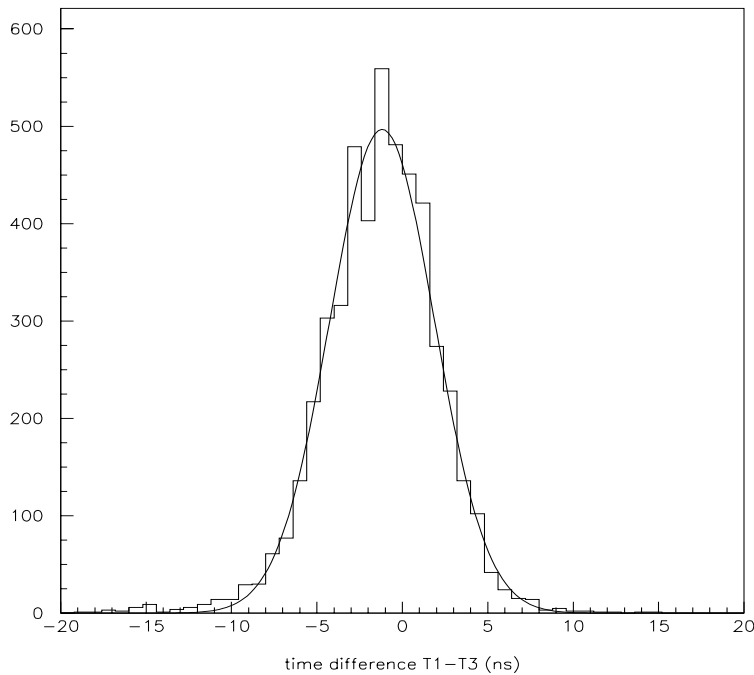


Figure 4-20. Histogram of the normalized time difference between a hit in trigger plane T3 and a hit in trigger plane T1 for penetrating muons from the muon calibration file.

The time difference follows a Gaussian distribution with $\sigma = 3.0\text{ns}$.

Events were therefore rejected if the interaction vertex was in modules zero, one, or two, and the trigger time difference between T1 and T3 was more than 10ns. Events were also rejected if both the trigger time difference between T1 and T3 was more than 5ns and the difference between T2 and T3 was more than 5ns.

This cut removed about 20% of the remaining data events.

No Vertex

The electron from a magnetic moment interaction typically produces an electromagnetic shower as it passes through the two radiation lengths of an emulsion module. If the interaction occurs at the downstream end of module four, this shower starts in the lead shield downstream of the target stand, which corresponds to ten radiation lengths. In this case the shower should be visible in the drift chambers.

Electromagnetic showers in the emulsion were easily recognized in the interactive analysis. They typically showed a vertex in the emulsion with five or more tracks in a narrow cone in the forward direction.

Events were rejected if they had no visible vertex at all or if the vertex was outside the fiducial region defined above. Most of the events shown above fall into one of these categories; no vertex could be identified in figure 4-15 whereas the reconstructed vertex in figures 4-13 and 4-17 is outside the fiducial region.

This cut removes about 10% of the remaining data events.

The cuts in step four removed less than 5% from any of the control samples. This was expected since only non-neutrino interactions were removed. In the analysis of the control sample, no events were rejected in most cuts; only the muon identification cut removed about 5% of the muon neutrino interaction sample, both in the data and Monte Carlo. No events were removed from the magnetic moment event sample or from the electromagnetic shower data sample. Nevertheless, the efficiency for magnetic moment events is assumed to be 97% to account for systematic effects.

Only 34 events remained in the data sample; all of them were neutrino interactions that were analyzed in more detail in step five.

Step Five

Only events consistent with a neutrino interaction remained after step four. This data sample was analyzed in detail with cuts that identified electrons and hadrons and distinguished between electromagnetic and hadronic showers.

Slow Hadrons

Sometimes a track that had a large scintillating fiber signal was not reconstructed properly. Figure 4-21 shows an example of several tracks behind module 4 that have a large pulse-height but were not reconstructed.

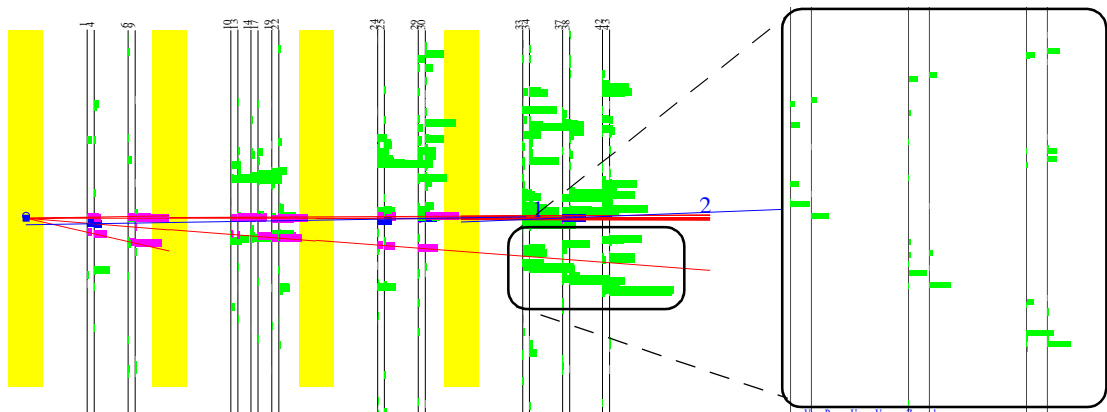


Figure 4-21. View of the target region for an event with a large pulseheight track (hits inside the oval) that was not reconstructed properly in the scintillating fiber planes. The box on the right-hand side shows a close-up view of the track hits.

If a non-relativistic charged particle scattered in a scintillating fiber plane, producing hits as shown in the figure, then the corresponding track was not reconstructed and the previous cuts did not remove the event. In the interactive analysis, such a track was seen as a series of large SF hits that were connected but did not lie on a straight line. Events with these tracks were rejected.

This cut removed 4 of the remaining 34 data events and none of the Monte Carlo magnetic moment events.

Shower Development

Some of the interactions in emulsion module four had two reconstructed tracks connected to the vertex. Figure 4-22 shows an example of such an event.

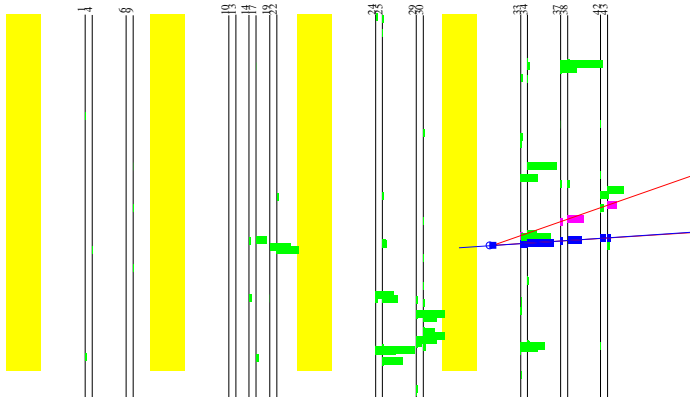


Figure 4-22. View of the target region for an event with two reconstructed tracks connected to the vertex.

Magnetic moment interactions of neutrinos with target electrons produce one final state electron that may in turn create an electromagnetic shower. In this process, two charged particles are produced in each step and the total number of charged particles is therefore always odd.

A photon entering the target region from the side may also produce an electron-positron pair. Since it has no charge, the initial photon in this process remains undetected; only the two particles would be visible in the scintillating fibers. The event shown above was most likely produced by such a photon conversion since only two charged particle tracks were reconstructed.

Events were therefore rejected if the neutrino interaction vertex was in module four and two or four reconstructed tracks were connected to the vertex.

This cut removed 6 of the remaining 30 data events and about 4% of the Monte Carlo magnetic moment events. In these misidentified events, one of the two particles from the pair conversion was not reconstructed.

Single Track Upstream of the Vertex

In some of the events, reconstructed tracks were connected to the vertex, but upstream of the vertex module. An example of this situation is shown in figure 4-23.

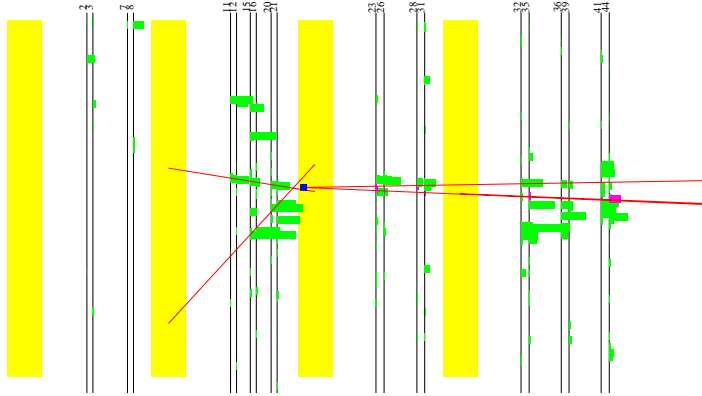


Figure 4-23. View of the target region for an event with two reconstructed tracks upstream of the interaction vertex.

The nuclear breakup that occurs in a neutrino-nucleon interaction typically produces many particles, some of which may travel upstream. If the momentum of these particles is large enough to exit the emulsion, they can be detected in the scintillating fiber system. This situation does not occur in neutrino-electron interactions because they do not involve nucleons. However, the electron in the magnetic moment interaction might be produced in one emulsion module and generate a shower in the next emulsion module downstream. This situation produces a similar event pattern as that mentioned above. It can be identified because the single electron is almost parallel to the neutrino, whereas the hadrons in the first case are typically not.

Events were therefore rejected if a track was reconstructed upstream of the interaction vertex and the track had an angle of more than 0.1rad with respect to the neutrino direction. This cut removed 7 of the remaining 24 data events and about 2% of the remaining Monte Carlo magnetic moment events. These were removed because one of the particles in the electromagnetic shower was identified upstream of the interaction vertex.

Single Track from Module Four

Figure 4-24 shows an event in which a single charged particle track was reconstructed behind emulsion module four. This event would be a magnetic moment interaction candi-

date event if the charged particle produced an electromagnetic shower in the lead downstream of the target region.

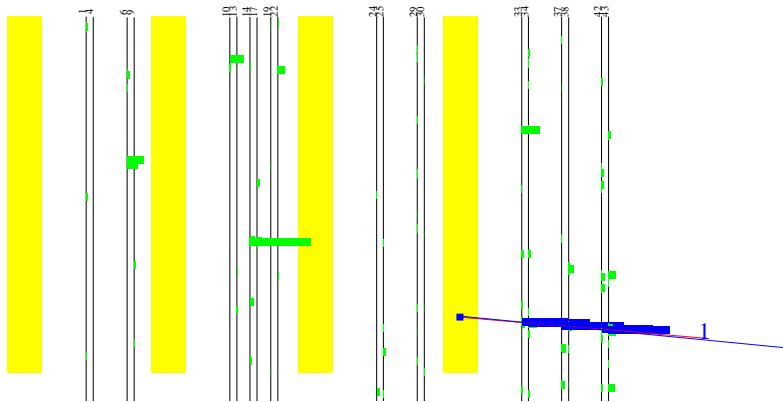


Figure 4-24. View of the target region for an event with a single reconstructed charged particle track downstream of emulsion module four.

Figure 4-25 shows a view of the event that includes the drift chambers.

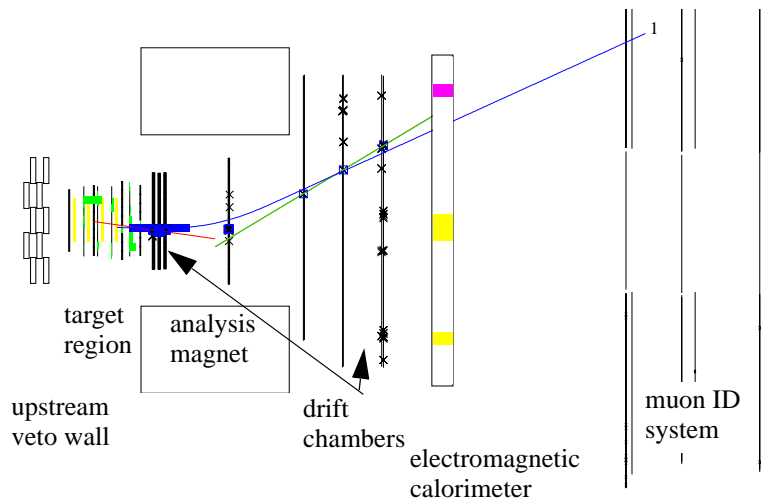


Figure 4-25. View of the target region and the downstream spectrometer elements for the event shown in figure 4-24

The particle did not produce a shower; it passed through the lead without scattering and was reconstructed and momentum analyzed. This event was most likely produced by charge transfer between a neutron that entered the target region and a proton in emulsion module four. This proton was then reconstructed in the spectrometer. It could also have been pro-

duced by a neutral-current neutrino interaction in which only a proton or pion was ejected from the nucleus.

Magnetic moment interactions in module four don't necessarily produce an electromagnetic shower in the emulsion module, but they can be expected to produce electromagnetic showers in the lead downstream of the target box since that corresponds to ten radiation lengths.

Events were therefore rejected if only a single track was reconstructed behind module four that did not produce a shower in the downstream lead. This cut removed 11 of the remaining 17 data events and about 4% of the remaining Monte Carlo magnetic moment events.

Shower Profile

Since electromagnetic showers develop in a narrow cone around the direction of the original electron. Since the electron from a magnetic moment interaction typically has an angle of less than 0.1rad with respect to the neutrino direction, the reconstructed shower tracks also have a similarly small angle.

Neutrino-nucleon interactions on the other hand break up the nucleus and produce low-momentum particles that travel at large angles, some of them even backwards. Figure 4-26 shows two histograms of the largest reconstructed track angle coming from the vertex.

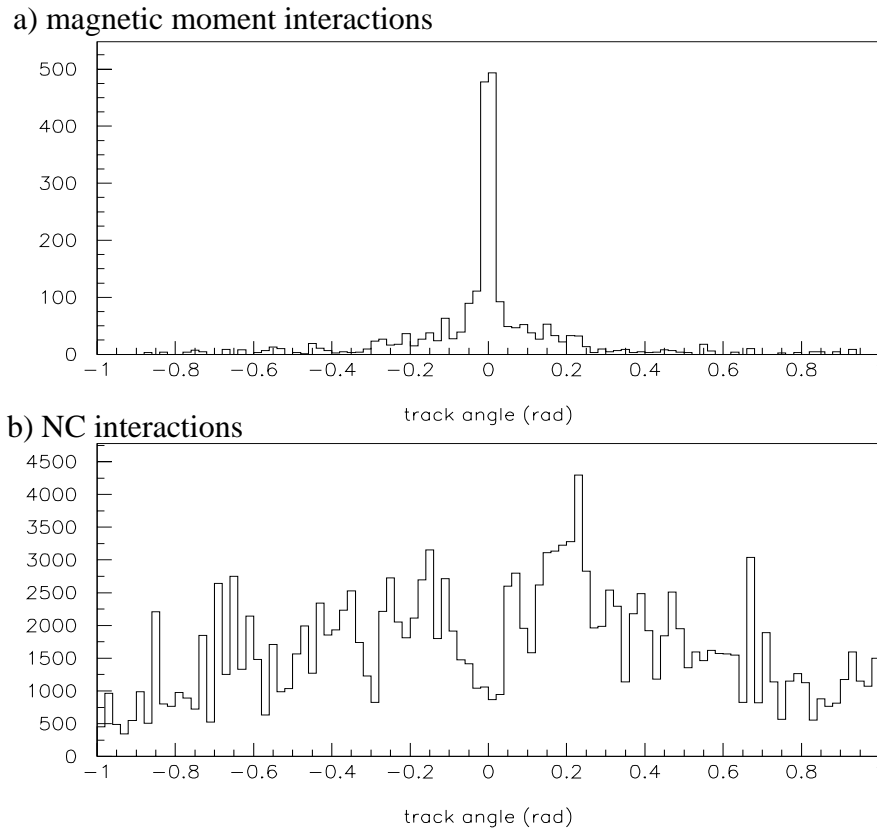


Figure 4-26. Maximum angle of a vertex track for events with five or less vertex tracks for magnetic moment events (upper histogram) and neutral-current events (lower histogram) for Monte Carlo events in period four.

Only events with five tracks or less were considered while larger showers were excluded because large electromagnetic showers usually have a few large-angle tracks.

Events were therefore rejected if five vertex tracks or less were reconstructed and at least one of them had an angle of more than 0.35rad with respect to the neutrino direction. If the neutrino interaction vertex was in station four, the cut was applied regardless of the number of vertex tracks. A tighter cut of 0.1rad was also considered, but that would remove many events from the tail of the distribution in figure 4-26 and reduce the efficiency of this cut for Monte Carlo magnetic moment events from 95% to 60%.

This cut removed 2 of the remaining 6 data events and about 5% of the remaining events in the Monte Carlo magnetic moment sample.

Hadrons Passing through a Module

Some of the remaining events had reconstructed tracks that did not produce a shower as they passed through an emulsion module. An example is shown in figure 4-27.

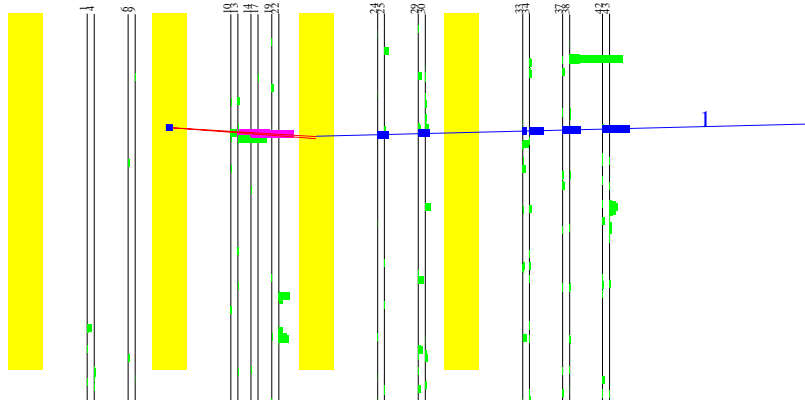


Figure 4-27. Target region view of an event with a reconstructed track connected to the vertex that passed through several emulsion modules.

The reconstructed track had a small angle with respect to the neutrino direction. Tracks like this one were already identified as hadrons in step one, but the event was only removed previously if the track angle was larger than 0.2rad with respect to the neutrino direction. It was not clear in that cut if smaller angle tracks were part of a particle shower.

In this cut, events were removed if they had a reconstructed track that passed through a module without producing a shower and with an angular deflection between emulsion modules of less than 0.1rad .

The cut removed 2 of the remaining 4 data events and about 2% of the remaining Monte Carlo magnetic moment events.

Only two events remained in the data sample after step five, which accepted about 85% of the remaining Monte Carlo magnetic moment events.

Figure 4-28 shows a summary of the step five analysis of the control events.

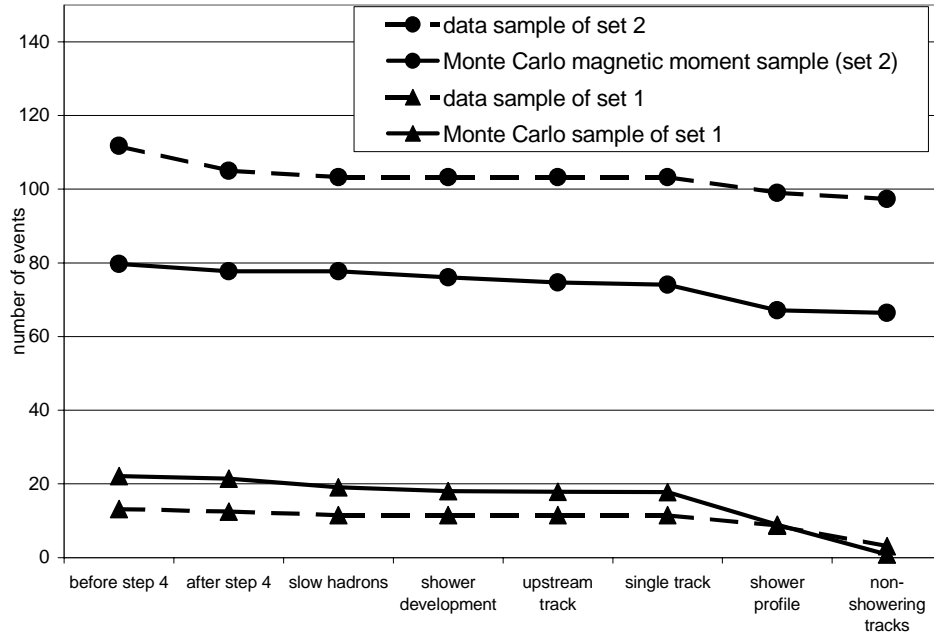


Figure 4-28. Number of events remaining in the control samples after step four and each of the step five cuts. The two lower lines (triangles) are for control set one of ν_μ charged-current interactions and the two upper lines (circles) are for control set two of electromagnetic showers. Each line starts at the number of events remaining after step three.

As before, the cuts removed the same fraction of events from the set of neutrino interactions with a muon (set one), within statistical uncertainty. The situation is similar for the electromagnetic shower samples (set two), although in this case data and Monte Carlo differed as a result of the step two and step three cuts as discussed above.

Figures 4-12, 4-18, and 4-28 also show that the selection efficiency for electromagnetic showers is considerably larger than for neutrino-nucleon interactions, both in the data and in the Monte Carlo. About 60% of the electromagnetic showers passed all of the selection cuts while more than 99% of the neutrino-nucleon interactions were removed. The analysis of all the different types of neutrino-nucleon interactions is given in chapter 5. In the analysis of the data sample, two events remained after all of the selection cuts.

5 Simulation

The selection of neutrino interactions and magnetic moment candidate events was based on particle identification and pattern recognition in the spectrometer. Events were selected if they contained no muons or hadrons and if they exhibited a hit pattern in the scintillating fibers that was identified as an electromagnetic shower. The development of these selection parameters was based on the analysis of events generated in a Monte Carlo simulation.

To obtain the efficiencies for each cut, all parts of the experiment had to be simulated, and the E872 Monte Carlo simulation therefore consisted of several building blocks: The first part was the generation of neutrinos, based on the parameters established in appendix A [49]. The second block was the interaction of these neutrinos with emulsion target nucleons, realized by the LEPTO program package [50]. This package was not able to generate neutrino magnetic moment interactions; this was taken care of by algorithms specifically developed for this thesis according to the cross sections from chapter 2. The third was the propagation of particles produced in the neutrino interactions through the detector and the simulation of the detector response. The GEANT detector simulation tool used for this last task modeled the interactions and decays of the different particles and the response of the detector elements in detail [51].

5.1 The Neutrino Event Generator

The generation of prompt neutrinos in the proton beam target followed the actual physical process outlined in appendix A. Charm mesons were generated in the proton beam target according to the angular and momentum distributions given in appendix A and their decay produced prompt neutrinos. Only small-angle neutrinos that passed through the emulsion targets were used in interactions. The neutrino interaction vertex was chosen according to the density of the target material, producing more interactions in the iron than in the emulsion or plastic.

The nonprompt neutrino beam component was modeled through the decay of kaons and pions in the proton beam target.

5.2 Neutrino Interactions

The interactions between incoming neutrinos and target nuclei were simulated by the LEPTO program package [50], which reproduced the hadronic component of the scattering process well. The lepton-nucleon cross scattering process was based on the leading-order electroweak cross sections of the underlying parton level.

Magnetic moment interactions between neutrinos and electrons from the atomic shell of the target atoms were generated according to the differential cross section from equation 2-8, with a low-energy cutoff for the recoil electron of 0.5GeV. All other scattering parameters were calculated from the neutrino energy and the fractional momentum transfer [52].

Figure 5-1 shows a typical simulated magnetic moment interaction.

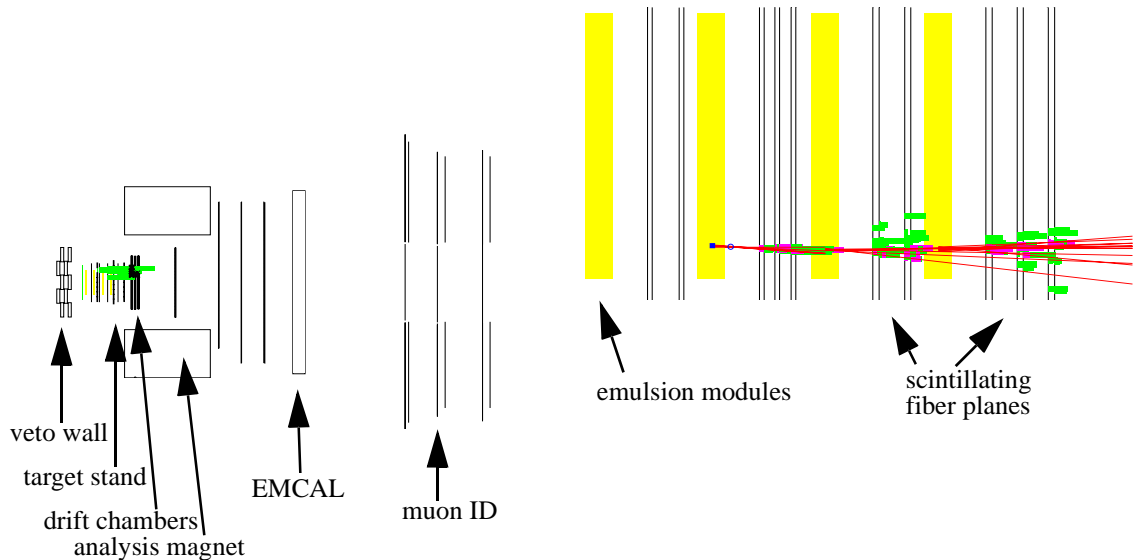


Figure 5-1. Typical simulated magnetic moment interaction. The left hand side shows a view of the entire spectrometer; the right hand side shows a close-up view of the target region.

The electron produces a shower that spread out behind the target stations downstream of the interaction point. However, none of the shower particles passed through the analysis magnet. This situation commonly occurs in magnetic moment interactions because of the lead wall downstream of the target region corresponding to seven radiation lengths.

5.3 The Hybrid Emulsion Spectrometer Simulation

Particles produced in the neutrino interaction were propagated through the spectrometer with the GEANT program package [51]. The scintillating fiber planes, drift chambers, electromagnetic calorimeter, and muon ID system were represented in detail in the simulation and building blocks such as the target stand, the magnet coils or the muon ID steel were also included. A charged particle passing through a sensitive detector element generated a detector hit that was stored on tape and translated into the correct format for the detector analysis software.

The Emulsion Targets

Each of the different emulsion target configurations was reproduced in the simulation, including steel plates, plastic sheet, and emulsion coating [39].

The Scintillating Fiber Tracker

Each of the forty-four scintillating fiber planes was a separate sensitive element in the detector simulation. It was not possible to generate the CCD image charge distribution typically found in data events. Instead, the simulation package generated fiber hits, calibrated with the hit distribution from muon runs [53].

The GEANT hit position was smeared by a Gaussian distribution with a width of 0.1mm and a hit was generated in the fiber closest to the smeared position. The signal was randomly selected from the experimental distribution corresponding to minimum ionizing particles [53].

To generate a hit that corresponded to the new SF decoder, several fibers around the hit position were filled in the simulation, with the largest signal in the center fiber and smaller signals in the fibers next to the center.

Downstream Tracking

Hits in the drift chambers were stored as the time difference between the trigger pulse and the signal arrival. The simulation package translated the drift chamber hits into wire drift times, taking into account uncertainties and efficiencies. The limit of one hit per wire in the large chambers downstream of the analysis magnet was also taken into account [38].

The Electromagnetic Calorimeter

Each of the 425 blocks in the calorimeter was a separate sensitive element in the GEANT simulation, and the total energy in each block was found by adding the contribution from all particles passing through it [44]. The energy sum was then smeared by the experimental resolution.

5.4 Calibration of the Monte Carlo

The analysis of simulated events is only meaningful if the Monte Carlo reproduces the conditions of the experimental run accurately. The equivalence of data and Monte Carlo was established on several levels of detail. At the lowest level, detector hits were smeared to reproduce the distributions found in the analysis of muons recorded with the special trigger setup outlined in section 4.1. The position uncertainties and efficiencies of the detector elements were adjusted to give the resolutions mentioned in chapter 4. At the next complexity level, the particle production thresholds in LEPTO and the tracking thresholds in GEANT were adjusted until particle multiplicity, track angles, calorimeter energy, and other event parameters resembled the data closely. The comparison was based on muon-neutrino charged current interactions that could be easily selected in the data as explained in appendix B.

At the next level, the momentum distributions of each neutrino flavor were calibrated by comparing the event energy measured in data files with the event energy obtained by analyzing Monte Carlo files. Only muon neutrino and electron neutrino charged current interactions were analyzed in this way since only these occurred frequently enough to generate distributions.

At the last level, the number of neutrino-nucleon interactions identified in the data was compared to the number of interactions expected for the proton flux and target mass. The last two tests were used to find proton flux, the number of events of the different neutrino flavors, the neutrino energy distribution, and the number of nonprompt neutrinos.

5.5 Monte Carlo Results

All of the cuts presented in section 4.6 were applied to the different neutrino interaction samples to find the selection efficiency. The goal of the selection process was to eliminate neutrino-nucleon interactions while keeping neutrino-electron magnetic moment interactions.

Each cut was adjusted to remove about 10% of the magnetic moment events. Moreover, the cut parameters were arranged to only remove events that were on the edge of the distribution under investigation. These two measures made the cuts relatively insensitive to systematic effects.

Magnetic Moment Interactions

The hardware event selection and the first pass of the neutrino event selection were designed to identify the shower particles produced by a neutrino-nucleon interaction. These

were not optimized for neutrino-electron interactions with small momentum transfers. The fraction of events remaining after the trigger selection is shown in figure 5-2.

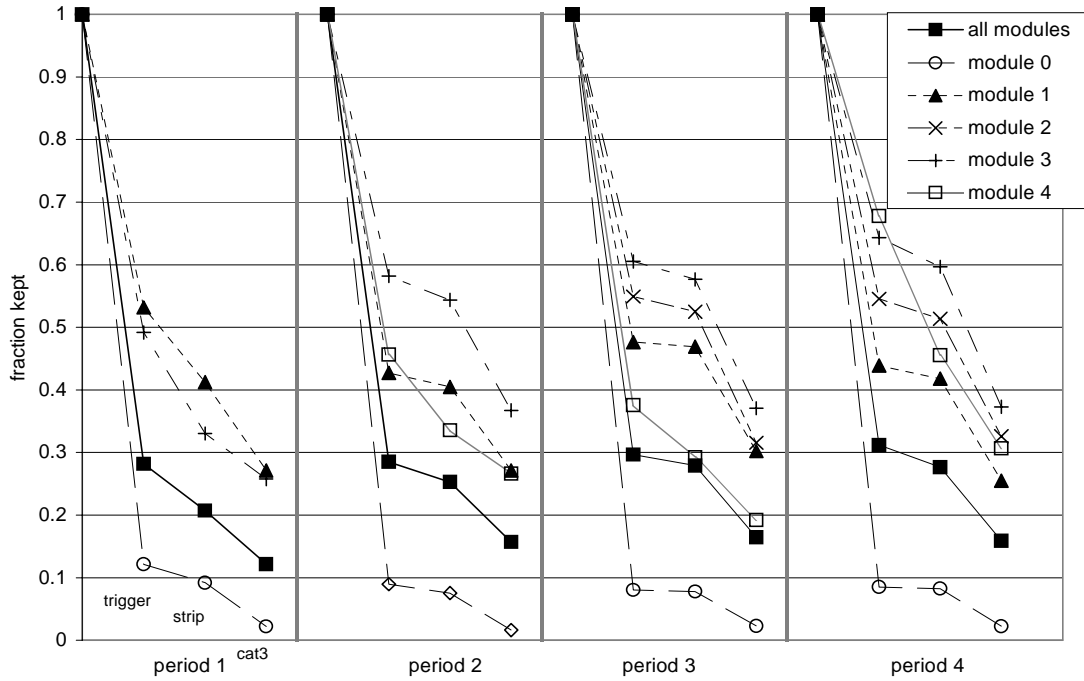


Figure 5-2. Trigger, pass 1, and visual selection efficiency for neutrino-electron magnetic moment interactions. Each plot shows the fraction of events remaining after the cut, starting at one. The second mark shows the trigger efficiency, the third mark the software selection efficiency. The visual selection efficiency is given by the fourth point.

As expected, the trigger cut out about half of the magnetic moment events, more from the upstream modules since the electrons in those interactions don't penetrate to the last trigger

plane. The effect of these selection cuts on the electron-energy distribution is shown in figure 5-3.

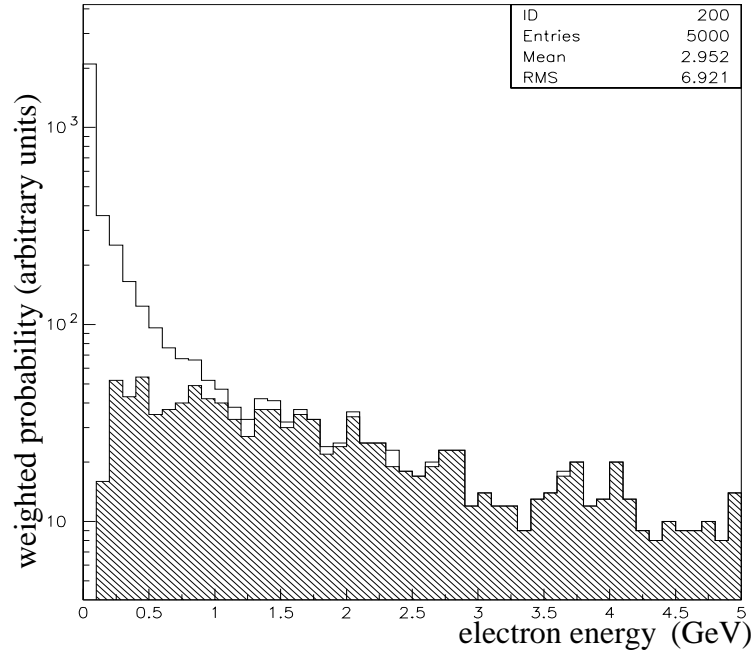


Figure 5-3. Distribution of electron energies for magnetic moment scattering. The solid histogram shows the spectrum of electron energies in neutrino-electron magnetic moment interactions. The shaded area shows the spectrum after trigger and software neutrino interaction selection.

Events with an energy below about 0.5GeV were removed from the data by the trigger and the software selection. Conversely, above an energy of about 3GeV all events remained in the sample.

The fraction of magnetic moment events remaining after each of the step one cuts is shown in figure 5-4.

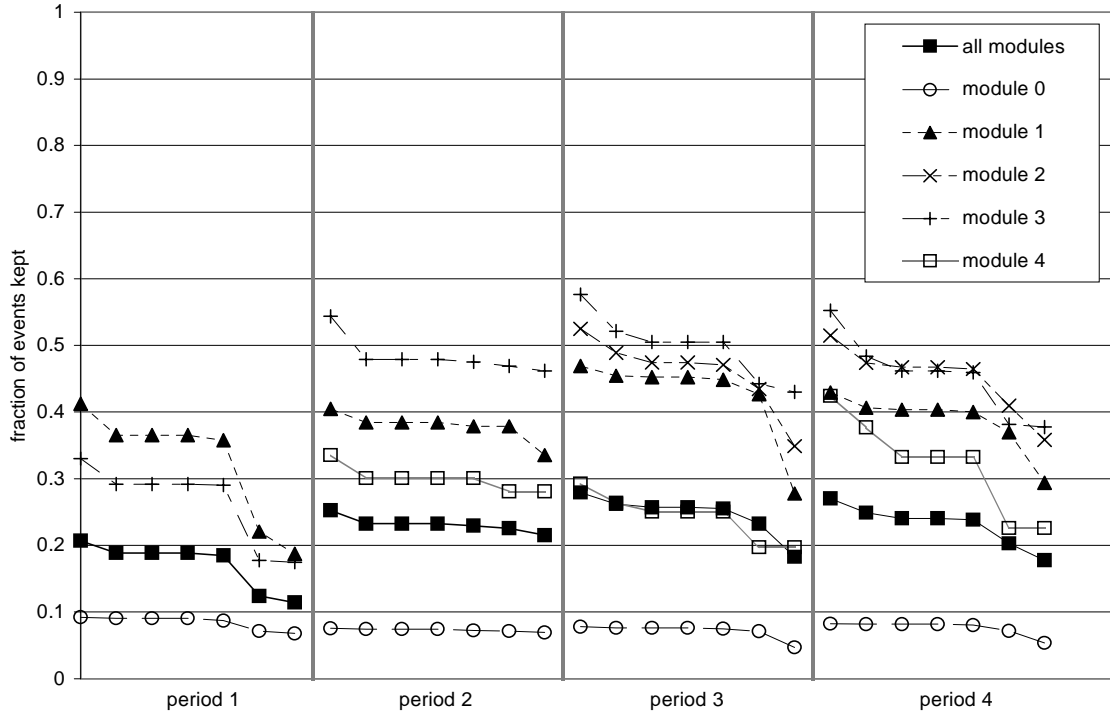


Figure 5-4. Step one selection efficiency for neutrino-electron magnetic moment interactions. Each line shows the fraction of events remaining after each of the cuts in step one, sorted by run period and target module. Each line starts at the fraction of events that is in the software event selection file (continuation of the plot from figure 5-2). The second point shows the fraction remaining after the muon cut, the third point shows the fraction remaining after the calorimeter energy cut, the fourth point shows the fraction remaining after the hadron cut, the fifth point shows the fraction remaining after the vertex reconstruction cut, and the last point shows the fraction of events remaining after all of the step one cuts.

Most of the cuts removed a small fraction of events; only the vertex reconstruction cut removed a larger fraction. In this cut, events were removed if they did not have at least one reconstructed track that was parallel to the neutrino direction. Although the first electron in almost all of the magnetic moment interactions is parallel to the neutrino beam, a surrounding electromagnetic shower could make its recognition impossible.

The fraction of magnetic moment events remaining after each of the step two cuts is shown in figure 5-5.

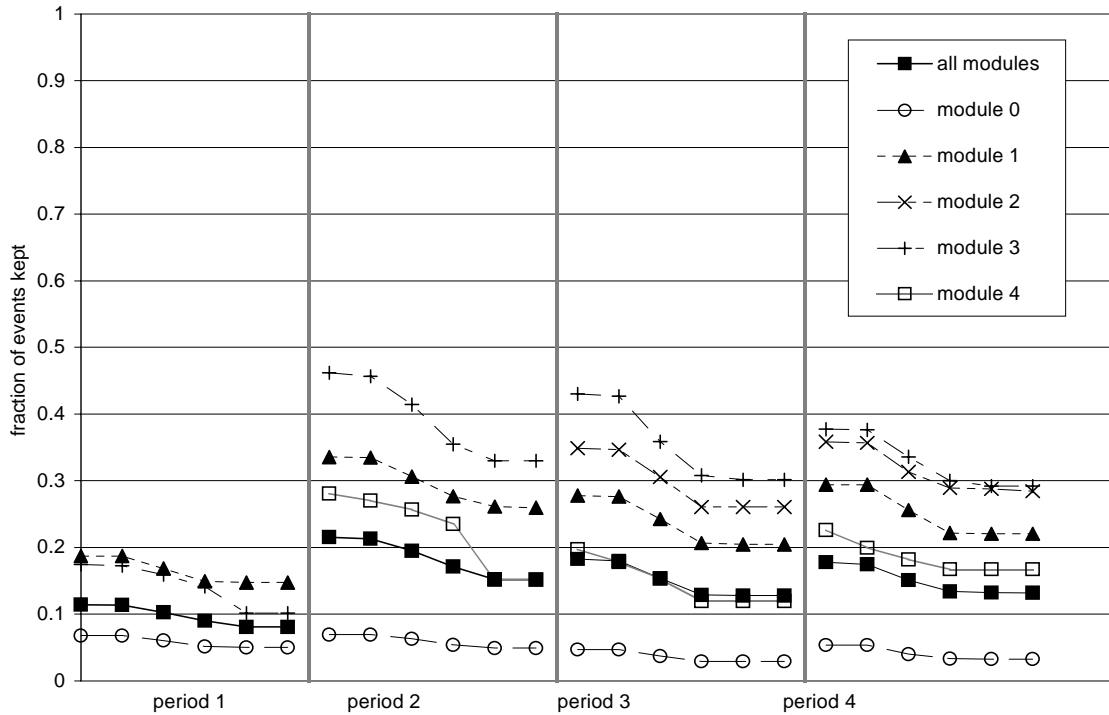


Figure 5-5. Step two selection efficiency for neutrino-electron magnetic moment interactions. Each plot shows the fraction of events remaining after the cut. The points show the fraction of events remaining after each of the cuts in step two. Each line starts at the fraction of events remaining after step one (each line is continued from figure 5-4). The second point shows the fraction of events remaining after the out-of-time cut, the third point shows the fraction remaining after the vertex location cut, the fourth and fifth points show the fraction remaining after the two trigger cuts, and the sixth point shows the fraction remaining after all of the pass two cuts.

Step two reduced the number of magnetic moment events by about 30%, mostly through the removal of backward triggers. In these events, a small electromagnetic shower developed behind the downstream module that produced two hits in the T2 trigger plane. However, the shower was so small that only one counter in the T3 trigger plane was hit, thus producing the signature of a backward trigger.

The fraction of magnetic moment events remaining after each of the step three cuts is shown in figure 5-6.

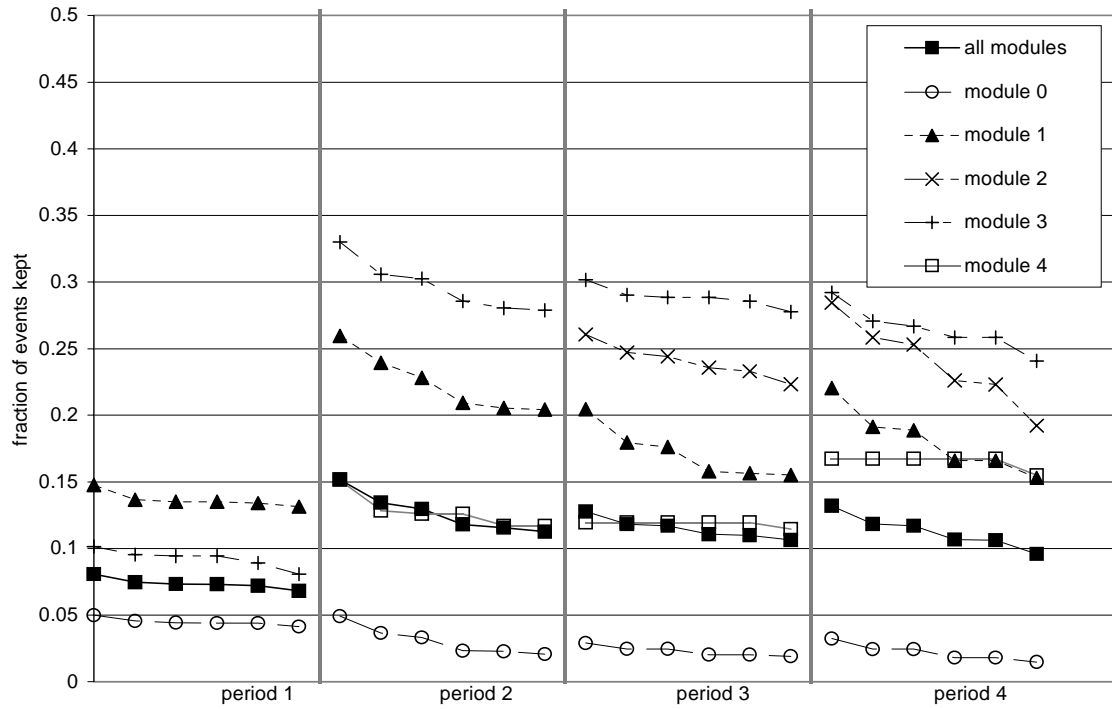


Figure 5-6. Step three selection efficiency for neutrino-nucleon interactions. Each plot shows the fraction of events remaining after the cut. The points show the fraction of events remaining after each of the cuts in step three. Each line starts at the fraction of events remaining after step two (each line is continued from figure 5-5). The second point shows the fraction of events remaining after the vertex track cut, the third point shows the fraction remaining after the single view track cut, the fourth point shows the fraction remaining after the downstream track cut, and the fifth point shows the fraction remaining after all of the pass three cuts.

Once again, while none of the cuts removed more than a few percent, the total number of magnetic moment events was reduced by about 30%. A histogram of the electron energy for events remaining after step three is shown in figure 5-7.

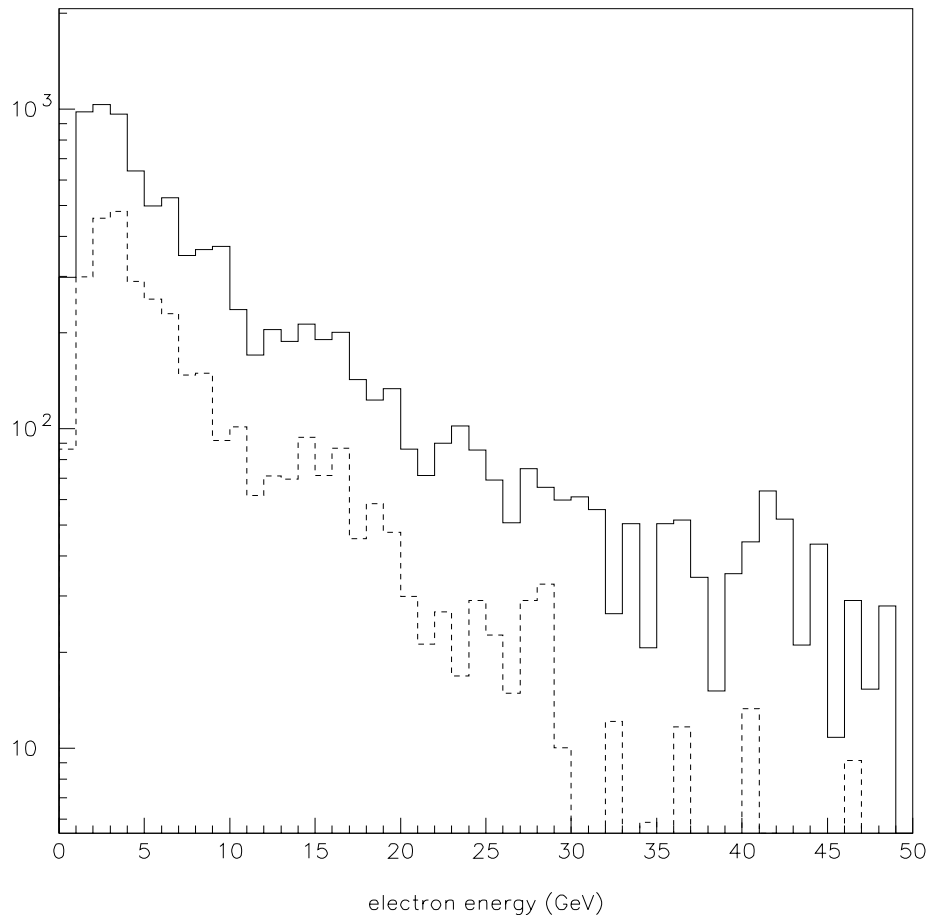


Figure 5-7. Histogram of the electron energy for magnetic moment events. The solid line shows the events selected by the neutrino interaction cuts (same as the shaded area in figure 5-3), the dashed line shows the energy distribution after the step three selection cuts.

Events with small electron energies were removed because the electromagnetic showers were not recognized, whereas events with large electron energies were removed because they were very similar to electron neutrino-nucleon interactions.

Only interactions that could not be identified as neutrino interactions were removed in step four. In principal, all magnetic moment interactions remaining after step three should be recognizable, as they all contain electromagnetic showers and reconstructed tracks. How-

ever, it is possible that many background tracks cover up a small shower in a magnetic moment event, and a conservative estimate for the efficiency of 97% was used for step four. The last step of the magnetic moment event selection relied on the recognition of electromagnetic showers. Table 5-1 shows the fraction of magnetic moment interactions that were removed by the step five cuts in the four run periods.

run period	number of events removed by the cut (in%)					number of events kept (in%)
	slow hadrons	shower development	single track	shower profile	non-show- ering tracks	
period 1	0	1.5	3	7	2.5	86
period 2	0	1	2	6	1	90
period 3	0	1	1	8	3	87
period 4	0	1	1	5	2	91

Table 5-1. Effect of step five cuts on tau neutrino-electron magnetic moment interactions in the four run periods. The cuts were done in series; events removed by the first cut were not analyzed with the second cut anymore. The last column shows the fraction of events that passed all of the cuts.

The selection efficiency for magnetic moment interactions was about 90% in step five, the overall efficiency for all cuts was about 10%, and most of the events were removed by the hardware trigger.

Neutrino-Nucleon Interactions

The interactions of neutrinos and nuclei produced a background to the magnetic moment search. These interactions were the main focus of the experiment and consequently the trig-

ger and software selection efficiencies are considerably larger than for magnetic moment events. They are shown in figure 5-8.

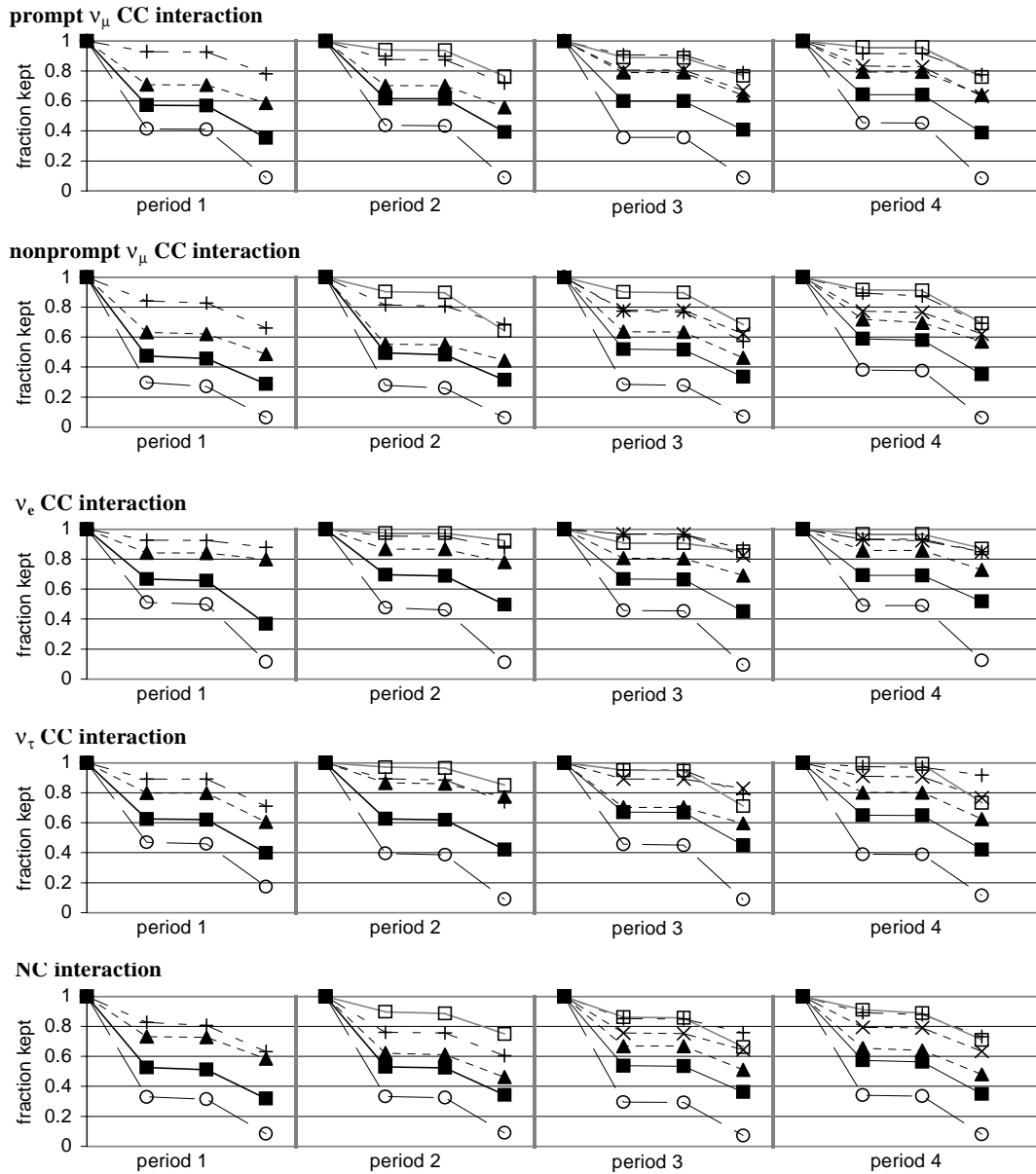


Figure 5-8. Trigger, software, and visual selection efficiency for neutrino-nucleon interactions. Each plot shows the fraction of events remaining after the cut; each line starts at one. The second mark shows the trigger efficiency, the third mark the software selection efficiency. The visual selection efficiency is given by the fourth point. Each line shows the efficiency for one emulsion module; the legend is shown in figure 5-2.

The hardware trigger selected almost all of the events in the emulsion modules; only interactions in the upstream lead wall were removed because some of the particles from the

nuclear breakup traveled upstream and produced hits in the upstream veto wall. This effect was correctly reproduced in the simulation [54].

The trigger efficiency was also affected by noise and background tracks. High-energy muons from the beam-dump target interacting in the steel surrounding the target module sometimes produced charged particles that hit the veto wall or entered the target area, generating additional trigger hits. The frequency of these background tracks was estimated with the help of events that had been identified as neutrino-nucleon interactions. It was found that they changed the trigger efficiency by less than 5%.

The first step in the neutrino interaction selection filtered out background events through simple cuts. The efficiency is also shown in figure 5-8; the cuts removed only very few neutrino-nucleon interactions.

Events with several high-momentum tracks coming from the vertex were easily identified in the visual scanning process, only if there was a large shower with many large angle tracks or if there was only a single track was the event missed in the visual selection. The selection efficiency was obtained by comparing the control event sample (see appendix B) to the output of the visual selection [55].

The first step of the magnetic moment filter was designed to remove events in which a muon or a hadron was identified in the downstream spectrometer elements. It removed

most of the muon neutrino-nucleon charged current interactions, as shown in figure 5-9. It furthermore removed about 70% of the other types of neutrino interactions.

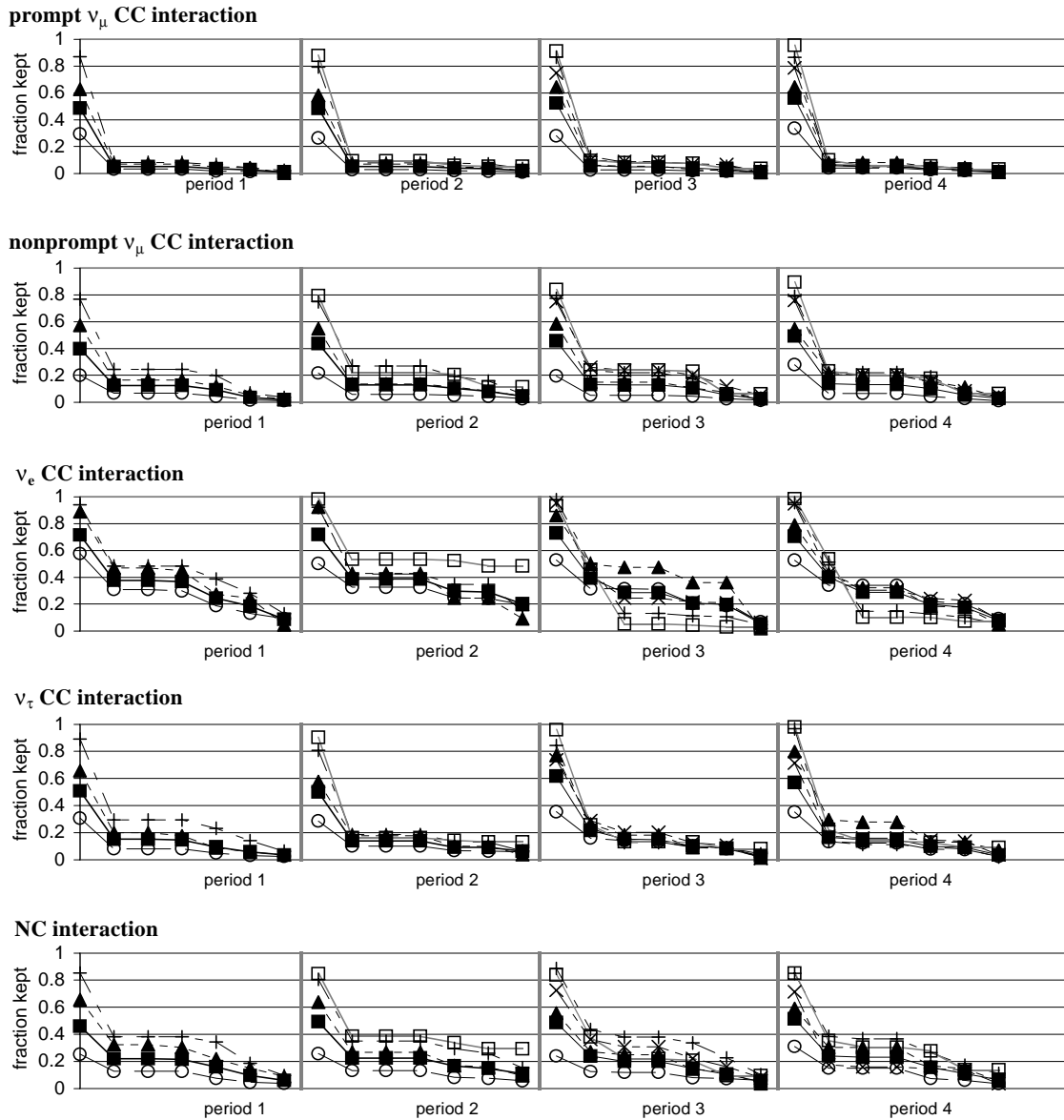


Figure 5-9. Step one selection efficiency for neutrino-nucleon interactions. Each line shows the fraction of events remaining after each of the cuts in step one, sorted by run period and target module. Each line starts at the fraction of events that is in the software selection event file (continuation of the plot from figure 5-8). The second point shows the fraction remaining after the muon cut, the third point shows the fraction remaining after the calorimeter cut, the fourth point shows the fraction remaining after the hadron cut, the fifth point shows the fraction remaining after the vertex track cut, and the last point shows the fraction of events remaining after all of the step one cuts. Each line shows the efficiency for one emulsion module; the legend is shown in figure 5-2.

After all of the step one cuts had been applied, the number of neutrino-nucleon interactions was reduced by a factor of ten. The step two selection cuts removed another half of these events; the efficiency is shown in figure 5-10.

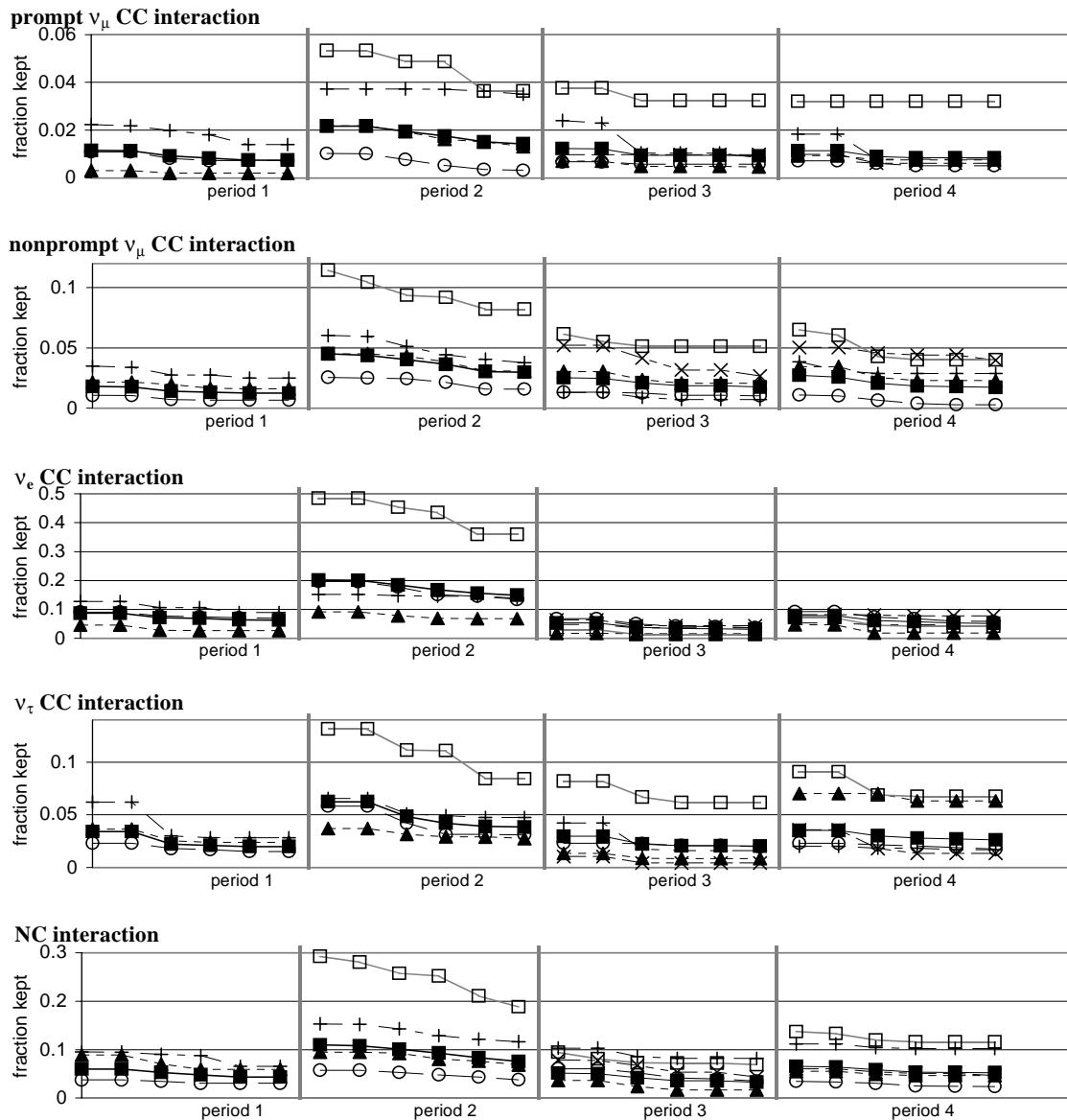


Figure 5-10. Step two selection efficiency for neutrino-nucleon interactions. Each plot shows the fraction of events remaining after the cut. The points show the fraction of events remaining after each of the cuts in step two. Each line starts at the fraction of events remaining after step one (each line is continued from figure 5-9). The second point shows the fraction of events remaining after the out-of-time cut, the third point shows the fraction remaining after the vertex location cut, the fourth and fifth points show the fraction remaining after the two trigger cuts, and the sixth point shows the fraction remaining after all of the pass two cuts. Each line shows the efficiency for one emulsion module; the legend is shown in figure 5-2.

The largest fraction was removed from interactions occurring in module four, most of them because the reconstructed vertex location was outside the fiducial region.

The step three selection efficiency for neutrino-nucleon interactions is shown in figure 5-11.

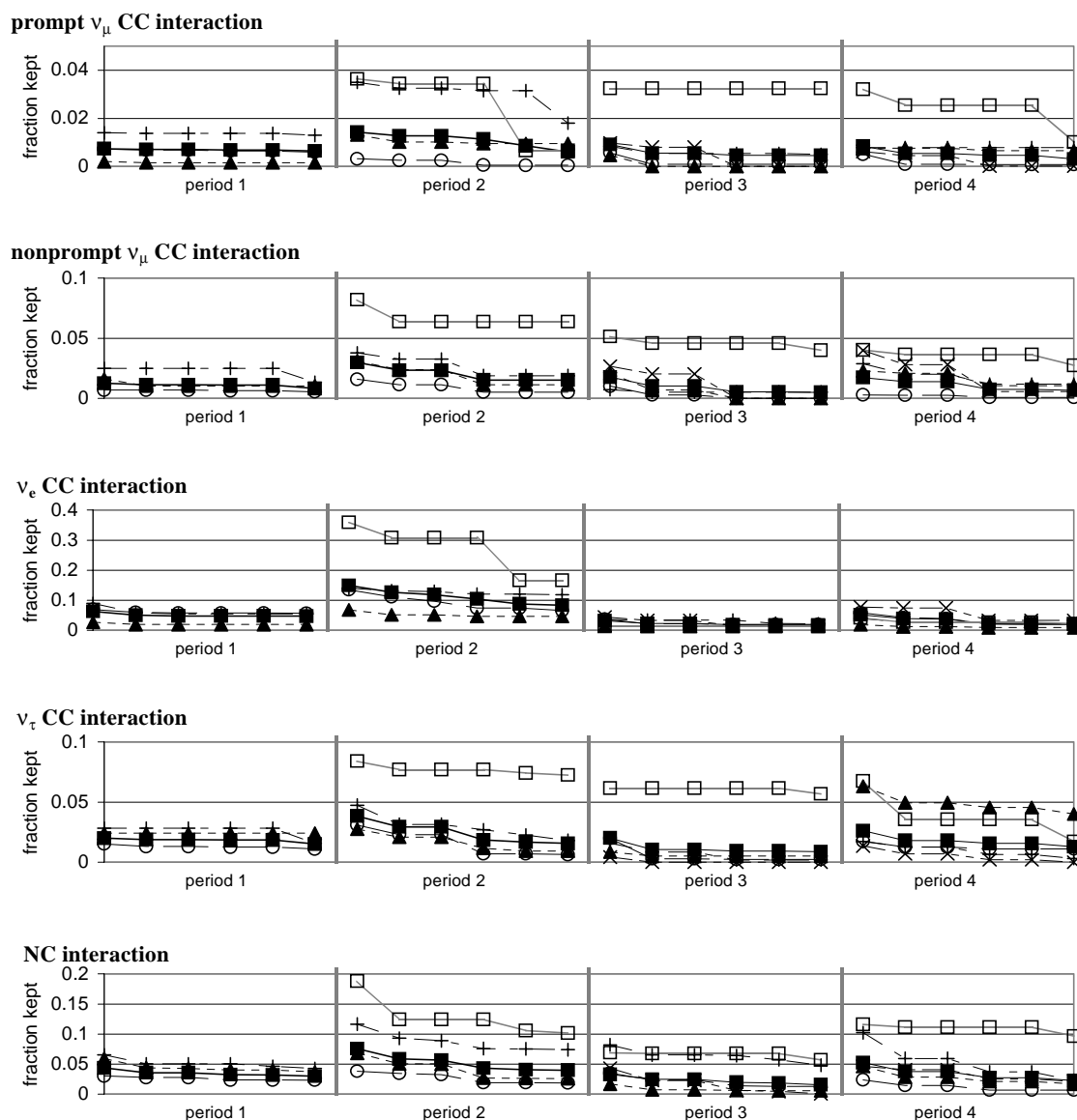


Figure 5-11. Step three selection efficiency for neutrino-nucleon interactions. Each plot shows the fraction of events remaining after the cut. The points show the fraction of events remaining after each of the cuts in step three. Each line starts at the fraction of events remaining after step two (each line is continued from figure 5-10). The second point shows the fraction of events remaining after the vertex track cut, the third point shows the fraction remaining after the single view track cut, the fourth point shows the fraction remaining after the downstream track cut, and the fifth point shows the fraction remaining after all of the pass three cuts. Each line shows the efficiency for one emulsion module; the legend is shown in figure 5-2.

Only events that did not have the signature of a neutrino interaction were removed in the visual selection of step four, and the number of neutrino-nucleon interactions remaining after step four is shown in table 5-2. Half of the remaining events were produced by electron neutrino charged current interactions.

event type	period 1	period 2	period 3	period 4	all periods
prompt ν_μ CC	0.45	0.29	0.50	0.65	1.89
nonprompt ν_μ CC	0.38	0.74	0.48	1.07	2.67
ν_e CC	4.10	5.91	4.24	5.73	19.98
ν_τ CC	0.35	0.34	0.42	0.90	2.01
NC	2.08	2.43	2.48	4.95	11.94
sum	7.36	9.72	8.11	13.30	38.49

Table 5-2. Number of neutrino-nucleon Monte Carlo interactions after visual selection in step four, sorted by event type.

The last step in the magnetic moment event selection removed neutrino-nucleon interactions in which at least one hadron was recognized in the spectrometer. The number of events remaining after step five is shown in table 5-3.

event type	period 1	period 2	period 3	period 4	all periods
prompt ν_μ CC	0.02	0.02	0.01	0.03	0.08
nonprompt ν_μ CC	0.03	0.05	0.05	0.06	0.19
ν_e CC	0.77	1.21	0.65	0.84	3.47
ν_τ CC	0.03	0.02	0.02	0.03	0.10
NC	0.09	0.21	0.09	0.20	0.59
sum	0.95	1.45	0.81	1.13	4.41

Table 5-3. Number of Monte Carlo neutrino-nucleon interactions remaining after step five, sorted by event type.

Again, most of the remaining events were electron neutrino charged current interactions with small momentum transfer to the target nucleus in which only the electromagnetic energy was visible in the spectrometer. Also, a total of 0.6 events were expected from neutral current interactions in which a hadronic shower was produced that could not be distinguished from an electromagnetic shower.

The Selection Uncertainty

All of the event selection cuts have been tested with the control event samples and no systematic difference between data and Monte Carlo has been found. The only uncertainty in the selection efficiency for neutrino-nucleon interactions and tau neutrino-electron magnetic moment interactions is therefore given by the statistical fluctuations due to the finite size of the Monte Carlo event sample. The number of events generated for each of the event types listed in table 5-3 was at least a factor of ten larger than the number of events expected in the data. In all, over 30000 neutrino-nucleon Monte Carlo interactions were generated. The resulting uncertainty in each cut is therefore about 1% and the statistical uncertainty in the selection efficiency for neutrino-nucleon events is about 5% (uncertainties added in quadrature).

The Monte Carlo event sample of tau neutrino-electron magnetic moment interactions contained 25000 events, and the statistical uncertainty in the selection efficiency is also about 5%.

Although the selection efficiency was calibrated and no difference could be found between data and Monte Carlo within statistical uncertainty for the control events, an additional contribution of 5% is added to the uncertainty in the selection efficiency. This accounts for the limited size of the control sample and is a conservative estimate of the uncertainty. It also accounts for any effects that are too small to observe in the control events.

6 Results

All of the magnetic moment selection cuts were applied to the full data sample, and the resulting candidate events and their possible production mechanisms (besides a magnetic moment interaction) are presented in this chapter.

The selection efficiency for magnetic moment events and the number of background events from neutrino-nucleon interactions was determined in the Monte Carlo simulation. To assure that the results obtained in the simulation are applicable to the data, each of the selection cuts was adjusted between data and Monte Carlo files with the two control samples explained in appendix B. Additionally, a subset of the cuts was applied to the set of visually selected neutrino interaction candidates. Since this event sample contained only neutrino interactions and was free from non-neutrino background events, the selection steps three and four were not required. Table 6-1 shows the number of events remaining in the two data sets and in the Monte Carlo simulation after each of the steps.

# of events remaining	all data	all MC	visual selection data	visual selection MC
initially	100,000	1412	819	931
after step 1	10,000	105	79	71
after step 2	2,700	70	43	54
after step 3	245	35		
after step 4	34	34		
after step 5	2	4.4	4	6.0

Table 6-1. Number of events remaining after each of the selection cuts. The cuts from step three and four were not applied to the visual selection data.

The complete data set contained a large fraction of background events that were gradually removed until none were left after step four. These events were not present in the visual

selection, and for this sample the number of events agrees between data and Monte Carlo for all steps.

The number of selected candidate events is consistent with the expected number of events from neutrino-nucleon interactions and no evidence for magnetic moment interactions has been found. Consequently, the measured neutrino magnetic moment is zero, and only a 90% upper confidence limit can be obtained in the statistical analysis of the result.

6.1 The Candidate Events

Out of the 100,000 analyzed events, only two remained after all of the cuts: one event in emulsion module three during period three, and the second event in emulsion module four during period four. The first candidate event is shown in figure 6-1.

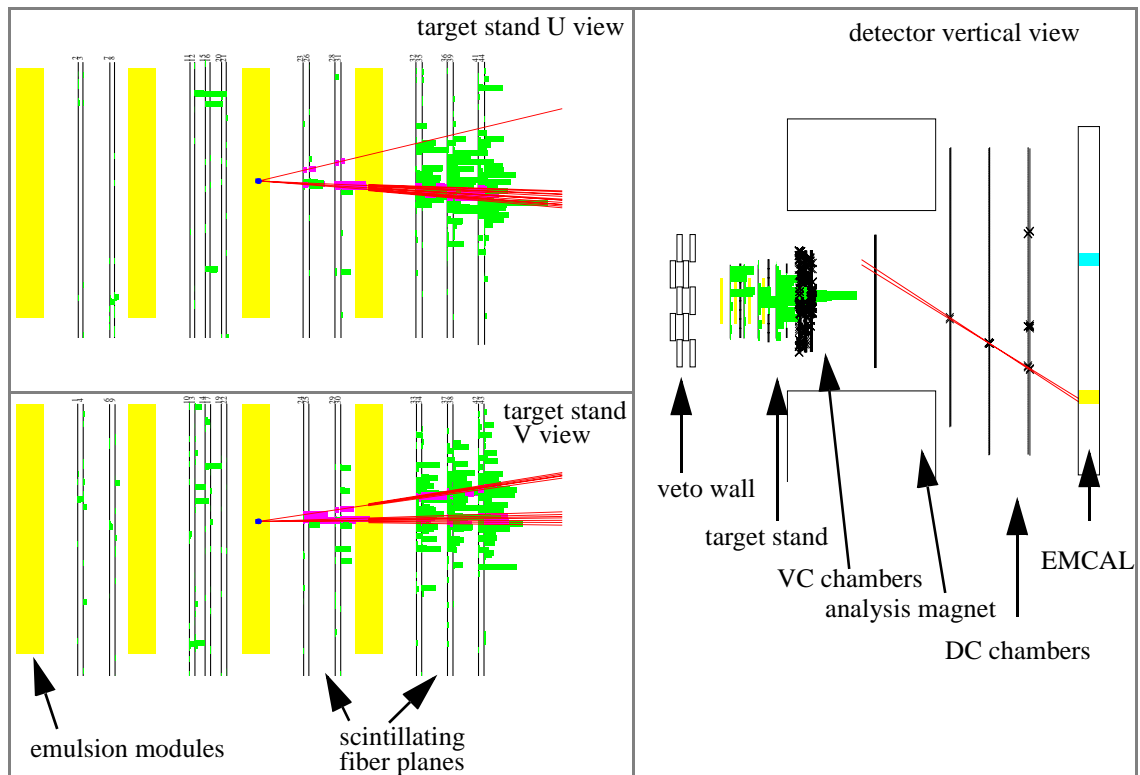


Figure 6-1. Three view of the first magnetic moment candidate event (run 3138, event 7918). Each dark line corresponds to a reconstructed track. The size of a hit in the SF planes indicates its pulseheight.

In this event, four charged particle tracks have been identified in each view. The three-dimensional particle trajectories could not be reconstructed unambiguously because the

tracks lie too close together, and there might actually be more than four tracks. One of the vertex tracks appears separate from the other three, and none of them pass through the next emulsion module without producing a shower. This particle shower was also identified in the VC drift chambers. However, only one charged particle track was identified downstream of the analysis magnet, with a measured momentum of less than 1GeV and a signal of 0.8GeV in the electromagnetic calorimeter.

The event was most likely produced by an electron-neutrino charged-current interaction with a target nucleon. The neutrino energy was probably small, since the total visible event energy has been measured to be about 26GeV. The hadrons produced in the nuclear breakup either interacted or decayed in the most downstream emulsion module. Besides the signal from the charged particle track that was identified downstream of the analysis magnet, one additional lead glass block was hit with a measured signal of 2.8GeV. Since no reconstructed track pointed to this block, this signal was generated by photons or neutral particles, with the most likely source being the decay of a π^0 into two photons.

The second candidate event is shown in figure 6-2.

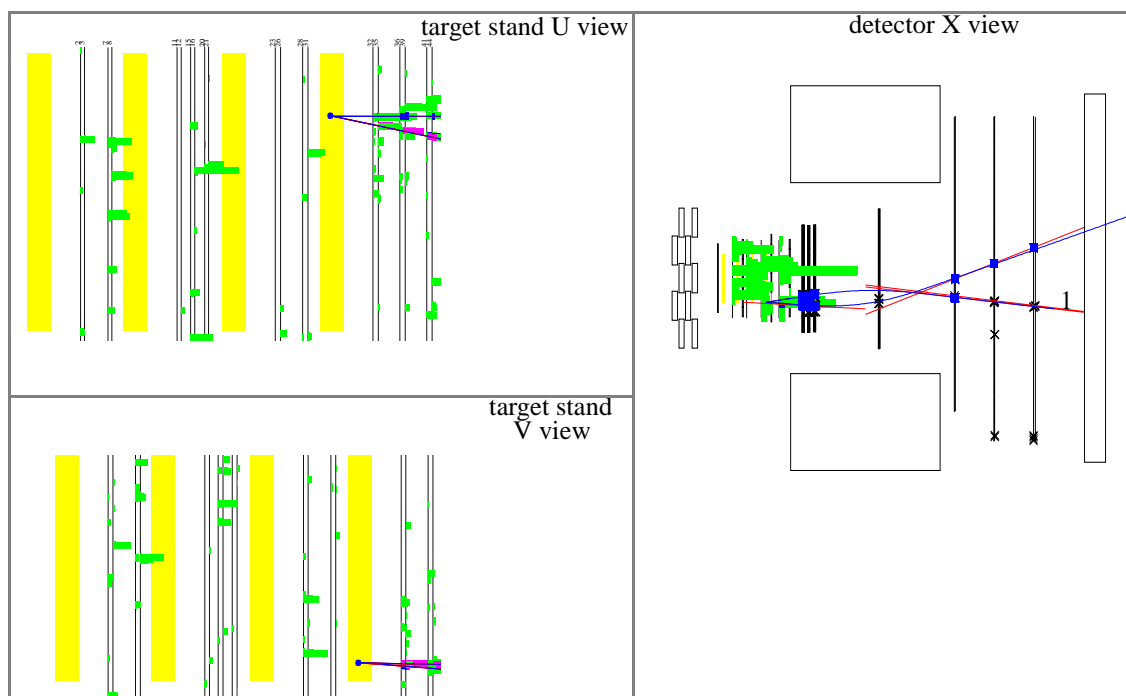


Figure 6-2. Three view of the second candidate event (run 3273, event 10082). Each dark line corresponds to a final track. The size of a hit in the SF planes is proportional to the fiber light signal.

In this event, three tracks have been reconstructed downstream of module four. Two of them have also been identified downstream of the analysis magnet; they had opposite charge and a similar measured momentum of about 1.2GeV with an opening angle of 0.15rad between them. The measured signal in the calorimeter was less than 0.5GeV for each track. Since they did not produce a particle shower downstream of the target stand, the two particles are likely a $\pi^+\pi^-$ pair, although it is also possible that they are an electron-positron pair. The third track has not been identified in the drift chambers and probably scattered in the trigger plane T3.

The momentum and opening angle between the two particles suggests the decay of a neutral particle with a mass of $(0.4 \pm 0.2)\text{GeV}$, the most likely candidate being the decay of a K_S^0 with an energy of 5.5GeV into two pions. The decay length for the kaon is a few cm, which means that the neutrino interaction probably occurred in the center of the emulsion module

and the K_S^0 decayed at the downstream edge of the module. This event is therefore most likely a neutral current interaction with a small momentum transfer to the nucleon.

6.2 Calculation of the Magnetic Moment

The measured value for the tau neutrino magnetic moment depends on the measured number of events, the tau neutrino flux, and the total target mass. This section describes how to derive the magnetic moment from these parameters.

The Magnetic Moment

The integral of the neutrino-electron magnetic moment cross section from equation 2-9 is given by

$$\sigma_{tot}(E_\nu) = f_\mu^2 \frac{\pi \alpha^2}{m_e^2} \int_{y_{min}}^1 \left(\frac{1}{y} - 1 \right) dy, \quad (6-1)$$

where $f_\mu = \mu_\nu / \mu_B$, and μ_B is the Bohr magneton. The integral is over the fractional energy transfer $y = T/E_\nu$, where T is the kinetic energy of the electron and E_ν is the incoming neutrino energy. However, not all incoming neutrinos have the same energy, hence the total cross section depends on the neutrino energy spectrum $\sigma_{prod}(E_\nu)$. When including this energy-dependence, the integral over y in equation 6-1 becomes

$$par = \int_{E_\nu} \int_{y_{min}}^1 \left(\frac{1}{y} - 1 \right) \sigma_{prod}(E_\nu) dy dE_\nu. \quad (6-2)$$

Accounting for this correction, equation 6-1 can be solved to give the magnetic moment (in units of Bohr magnetons):

$$f_\mu = \sqrt{\frac{\sigma_{tot} m_e^2}{par \pi \alpha^2}}. \quad (6-3)$$

The Total Cross Section

The total cross section σ_{tot} is determined experimentally from the number of neutrino-electron magnetic moment interactions n'_e and the incoming neutrino flux ϕ_{in} ,

$$n'_e = \phi_{in} \times \sigma_{tot}. \quad (6-4)$$

The cross section is given in m^2 per target electron, while the flux is given in neutrinos/ m^2 . The number of events n'_e is therefore the number of scattered electrons per target electron. To convert it into the total number of interactions that occurred in the target, this number is multiplied by the number of target electrons (n_{te}),

$$n_e = n_{te} \times n'_e, \quad (6-5)$$

where n_{te} can be calculated from the target mass M :

$$n_{te} = \frac{Z}{A} \frac{M}{1.66 \times 10^{-27} \text{ kg}}, \quad (6-6)$$

where Z is the atomic charge and A the atomic number and averaging over all target materials gives $Z/A=0.49$.

Equation 6-4 can now be solved to find the total cross section,

$$\sigma_{tot} = \frac{n_e}{n_{te} \phi_{in}}. \quad (6-7)$$

Event Selection

Not all of the magnetic moment interactions that occurred were also observed as some of them were removed by the event selection cuts. The fraction of events that passed all of the cuts is given by the selection efficiency ε , which relates the actual number of tau neutrino-electron magnetic moment interactions n_e to the number of magnetic moment interaction candidates n_{signal} through

$$n_e = \frac{n_{signal}}{\varepsilon}. \quad (6-8)$$

Background Correction

The selection cuts not only selected magnetic moment interactions but also a few neutrino-nucleon interactions. Hence, the number of magnetic moment interaction candidates is the difference between the total number of observed events (n_{obs}) and the expected number of background events (n_{bg}), or $n_{obs} = n_{signal} + n_{bg}$.

6.3 Collection of Experimental Parameters

The selection efficiency and the number of expected background events were determined with the Monte Carlo simulation described in chapter 5. The calculation of the incoming neutrino flux is given in appendix A; it is consistent with the observed number of ν_e CC and ν_μ CC interactions.

The Event Selection Efficiency

The selection efficiency for neutrino-electron magnetic moment interactions is shown in table 6-2.

	period 1	period 2	period 3	period 4	all periods
station 0	0.035	0.017	0.017	0.013	0.018
station 1	0.111	0.170	0.136	0.134	0.136
station 2			0.196	0.169	0.180
station 3	0.069	0.237	0.244	0.211	0.195
stations 4		0.099	0.100	0.136	0.117
all stations	0.058	0.095	0.093	0.084	0.087

Table 6-2. Event selection efficiency ε for all target stations and run periods. The different target configurations and neutrino fluxes have been taken into account.

Although the selection cuts were designed to remove very few neutrino-electron magnetic moment interactions, only a small fraction of events remained in the final sample. Most of the events were removed by the trigger condition (see figure 5-2), which required a particle shower behind the most downstream emulsion module. Magnetic moment interactions in

the upstream emulsion modules were thus removed since the typical energy in these interactions is small.

The uncertainty in the selection efficiency has been estimated to be 9%, see also section 5.5.

The Expected Number of Background Events

The dominant source of background in the remaining event sample is from neutrino-nucleon interactions; 4.4 such events are expected. About half of these are from ν_e CC interactions in which the hadronic particles were not recognized. Table 6-3 shows a detailed listing of the number of neutrino-nucleon interactions in each module and run period that passed all of the selection cuts.

target station	period 1	period 2	period 3	period 4	all periods
station 0 (upstream lead)	0.64	0.46	0.36	0.40	1.87
station 1	0.15	0.17	0.04	0.09	0.45
station 2	n/a	n/a	0.04	0.16	0.20
station 3	0.16	0.39	0.12	0.19	0.87
station 4	n/a	0.43	0.25	0.29	0.98
all stations	0.95	1.45	0.81	1.13	4.41

Table 6-3. Number of Monte Carlo neutrino-nucleon interactions remaining after step five.

Other sources of background include weak neutrino-electron interactions and photon conversions in the emulsion in which the positron is lost. Both processes contribute less than 0.05 events to the background event sample.

The Neutrino Flux

The tau neutrino flux at the target is $\phi'_{in} = (2.1 \pm 0.3) \times 10^{-5} \nu_{\tau}/m^2/POT$; the flux calculation is outlined in appendix A. The uncertainty in the flux is dominated by the uncertainty in charm production within the proton-beam target. The total number of neutrinos per unit

area is obtained by multiplying the flux by the number of protons on target that is given in table 4-1. The result is shown in table 6-4.

	period 1	period 2	period 3	period 4	all periods
ν_τ flux ($\times 10^{12} \nu_\tau/\text{m}^2$)	1.08	0.88	2.06	3.10	1.80

Table 6-4. Neutrino flux Φ_{in} for the four run periods. The flux for all periods is averaged over the four periods, weighted by the total target mass in each period.

The integral over the neutrino beam energy spectrum in equation 6-2 has a numerical value of $par = 4.35$; it is dimensionless. The product $m_e^2/(\pi\alpha^2)$ has the numerical value $m_e^2/(\pi\alpha^2) = 4.006 \times 10^{28} \text{ m}^{-2}$.

6.4 Statistical Analysis

Since fewer magnetic moment candidates were found than expected from background processes, the estimated tau neutrino magnetic moment is zero. However, the number of events is a probabilistic variable that follows Poisson statistics with a fixed but unknown mean.

A mean of 4.4 events gives a probability to observe exactly two events of 12% and a probability to observe two or less events of 18%. The statistical treatment yields a confidence interval, which in this case ranges between zero and the 90% upper confidence limit, which is found in this section.

The interpretation of the confidence limit depends on the approach to statistical data analysis. Two different approaches are currently used in high-energy-physics.

The Frequentist or “classical” approach starts from the definition of probability as the frequency of an event in an experiment that is repeated many times [56]. If an experiment is repeated n times and A is one of the possible outcomes, then the probability P for A is given by

$$P(A) = \lim_{n \rightarrow \infty} \frac{\text{number of times } A \text{ occurs in } n \text{ measurements}}{n}. \quad (6-9)$$

A 90% confidence limit means that if the experiment were repeated many times and a confidence limit is found in each experiment, then the fixed but unknown true value will be lower than the limit in 90% (or more) of the experiments¹. This approach is widely used in

neutrino physics and it does not require the definition of a prior probability distribution for the neutrino magnetic moment [57]. It has the disadvantage that it does not allow the incorporation of all types of systematic uncertainty. In the Frequentist interpretation, uncertainty is not a probability in the strictest sense because it usually expresses ignorance of a detector that has a fixed but imperfectly known response. Only if the systematic uncertainty itself was determined in a large number of repeated experiments, can it be included in a Frequentist analysis.

The Bayesian approach defines probability as a measure of the degree of belief that a certain outcome will occur [59]. This definition is very general and allows for systematic uncertainties, personal opinions, and predictions made from data. A 90% confidence limit in the Bayesian interpretation expresses that based on one measurement we are 90% certain that the magnetic moment is smaller than the limit. This definition has the advantage that it refers directly to the magnetic moment (rather than many experiments). It has the disadvantage that a prior probability distribution function for the magnetic moment is required as input to the analysis. Both approaches are discussed below as they apply to this observation.

The Strict Classical Evaluation

Of all of the parameters in the analysis, only the observed number of events n is a probabilistic variable. The statistical analysis procedure follows reference [57]: First, a 90% acceptance interval for the number of events n is determined for each possible value for the true number of signal events, n_{true} . In a graph of n versus n_{true} , the acceptance intervals appear as a belt, the “confidence belt” shown in figure 6-3. The 90% confidence interval for n_{true}

1. This is the definition of probability as limiting relative frequency given in [56].

is then given by the intersection of the belt with the vertical line corresponding to the number of events actually observed in the experiment.

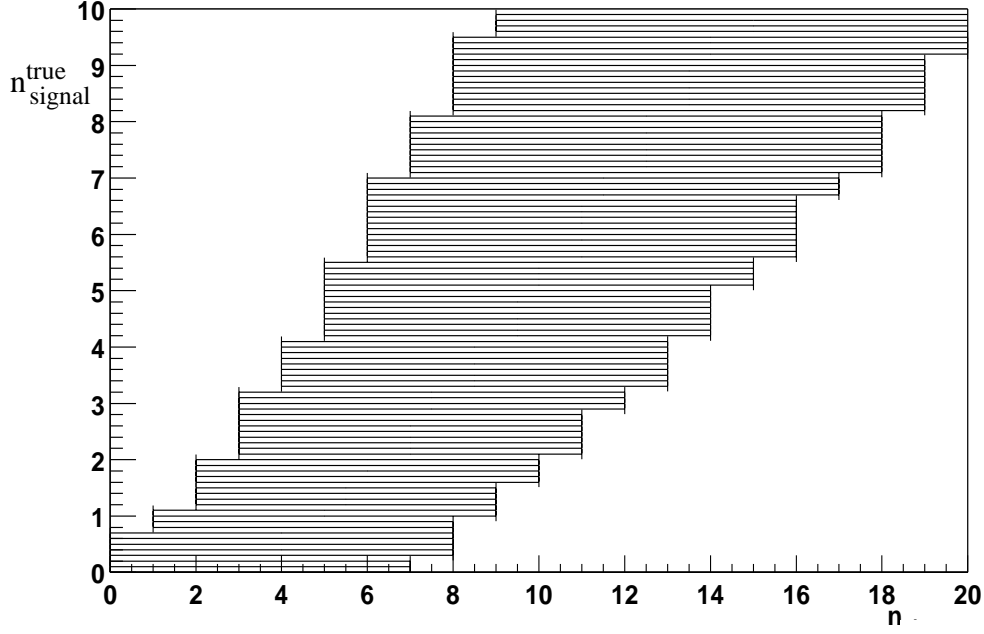


Figure 6-3. Confidence belt for equation 6-10 with $n_{bg}=4.4$. Each horizontal line corresponds to an acceptance interval.

The Acceptance Interval

The interval that contains the measured value 90% of the time in repeated experiments is the acceptance interval; it is defined for a given combination of signal and background.

As was mentioned before, the number of events is the sum over the number of signal events n_{signal} and the number of background events n_{bg} ,

$$n = n_{signal} + n_{bg}. \quad (6-10)$$

Both n_{signal} and n_{bg} are probabilistic variables with mean n_{signal}^{true} and n_{bg}^{true} . The sum follows a Poisson distribution,

$$P(n|n_{signal}^{true}) = \frac{(n_{signal}^{true} + n_{bg}^{true})^n}{n!} e^{-(n_{signal}^{true} + n_{bg}^{true})}. \quad (6-11)$$

The acceptance interval $[n_1, n_2]$ is then defined as the interval that contains 90% of the possible values for n ,

$$P(n \in [n_1, n_2] | n_{signal}^{true}) \geq 0.9. \quad (6-12)$$

The requirement in equation 6-12 only determines the size of the interval; it does not determine both limits n_1 and n_2 uniquely. An ordering principle based on likelihood ratios is used to center the interval on the most probable values for n .

The Likelihood Ratio

The likelihood ratio R determines where the acceptance interval should be centered. It is given by the ratio of the probability to observe n given the mean n_{signal}^{true} , normalized to the probability to observe n in the best possible situation, or

$$R = \frac{P(n | n_{signal}^{true})}{P(n | n_{best})}. \quad (6-13)$$

The normalizing factor $P(n | n_{best})$ is the probability at a value of $n_{signal}^{true} = n_{best}$ that maximizes P , under the condition that n_{best} be physically allowed ($n_{best} \geq 0$);

$$n_{best} = \begin{cases} 0 & \text{if } n \leq n_{bg} \\ n - n_{bg} & \text{if } n > n_{bg} \end{cases}. \quad (6-14)$$

The three quantities are shown in figure 6-4.

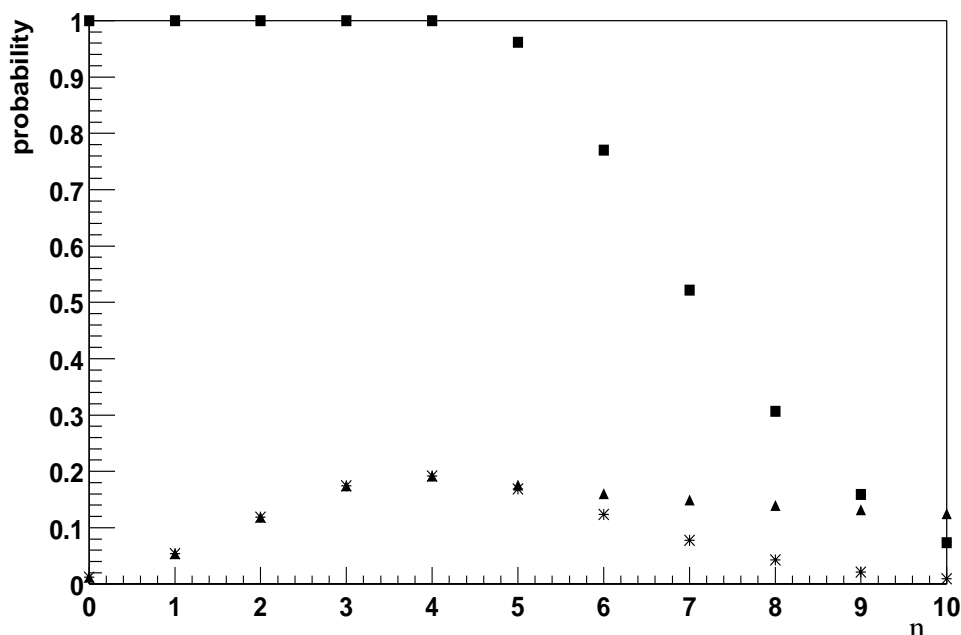


Figure 6-4. Probability distribution from equation 6-13 for $n_{signal}^{true} = 0$ and $n_{bg}^{true} = 4.4$. The stars show $P(n|n_{signal}^{true})$, the triangles show $P(n|n_{best})$, and the squares show R .

The ratio is exactly one as long as n is smaller than the expected background. For larger n , the ratio is normalized by the peak probability and R decreases rapidly.

The acceptance interval is then constructed by starting at the largest value of R and adding points along the n axis to the interval in decreasing R order until condition 6-12 is satisfied.

The Confidence Belt

A collection of acceptance intervals for many different values of the mean signal and background forms the confidence belt. In general, it depends on both of these parameters, but it is usually shown only in a two-dimensional plot with a fixed number of background events.

A graph of the acceptance intervals for many different values of n_{signal}^{true} at a fixed value of n_{bg}^{true} is shown in figure 6-3.

The Confidence Limit

The 90% confidence interval is determined from the confidence belt in figure 6-3 by finding the vertical line that corresponds to the number of events observed in the experiments.

Since two events were observed in this analysis, the lower edge of the confidence limit is zero and the upper edge is 2.05. Hence, the interval is interpreted as a 90% upper confidence limit for n_{signal} of 2.05.

The Limit for the Magnetic Moment

From the confidence limit obtained for n_{signal} , the total cross section is found according to the outline in section 6.2. Correcting for the selection efficiency with equation 6-8, the limit for the number of interactions that occurred is $n_e \leq 23.7$, which corresponds to a cross section of $\sigma_{tot} \leq 1.9 \times 10^{-41} \text{ m}^2$ according to equation 6-7. Equation 6-3 then gives a 90% upper confidence limit for the tau neutrino magnetic moment of $f_\mu \leq 4.2 \times 10^{-7}$.

Systematic uncertainties in the target mass and the neutrino flux have to be ignored in the classical treatment since they are not probabilistic variables in the Frequentist description. These nuisance parameters require a Bayesian treatment, which could be combined with the Feldman-Cousins method in a semi-classical statistical analysis [58].

Including Systematic Uncertainties

Rather than mixing Bayesian and Frequentist interpretations to incorporate systematic uncertainties, a purely Bayesian analysis is used. This method views uncertainty as a “degree of belief”, which is a natural and accurate description of a systematic uncertainty [59].

Sources of Systematic Uncertainty

The largest uncertainties are in the tau neutrino flux and in the determination of the selection efficiency and the background. Other quantities such as the target mass are known accurately and their uncertainty does not contribute to the overall uncertainty. To simplify the calculation, a Gaussian distribution function is assumed for each of the parameters under consideration. This is a reasonable approximation since the uncertainties are either due to fluctuations in a large number of Monte Carlo events or due to imprecise measurements.

There are two uncertainties associated with the tau neutrino flux: One is the possible variation in the neutrino production with an uncertainty of 15%. The other is the uncertainty in

the total number of protons on target, which is estimated to be 15%. Besides these two factors which affect the total number of neutrinos, the energy and angle distributions of the neutrinos is also not completely known. They are determined by the two parameters n and b (defined in appendix A.4), and their uncertainty affects the selection, background, and the integral over the neutrino spectrum from equation 6-2.

The expected number of background events was determined with the Monte Carlo simulation in which a total number of 30000 events were generated. The selection uncertainty due to the number of events has been estimated in section 5.5 to be 5%. The simulation of magnetic moment events was done with a similar number of events, yielding the same uncertainty in the selection efficiency of 5%.

The differences between Monte Carlo and data files are tested in the cross-check events. No systematic difference can be seen. Nevertheless, an additional systematic uncertainty of 5% is used to reflect the degree of belief in the accuracy of the Monte Carlo simulation.

source	Quantity	uncertainty (in%)
number of protons on target	ϕ_{in}	15
neutrino-beam calculation	ϕ_{in}	15
number of Monte Carlo events	n_{bg}	5
number of Monte Carlo magnetic moment events	\mathcal{E}	5
degree of belief in the precision of the Monte Carlo	\mathcal{E}, n_{bg}	5
uncertainty in n and b	\mathcal{E}, n_{bg}, par	5
total flux uncertainty	ϕ_{in}	21.2
total background uncertainty	n_{bg}	8.7
total selection uncertainty	\mathcal{E}	8.7

Table 6-5. Sources of systematic uncertainty.

Bayes' Theorem

The probability distribution function from equation 6-11 gives the probability to observe n_{obs} events for a fixed magnetic moment factor f_{μ} . The classical method does not view f_{μ} as a probabilistic variable: it is fixed but unknown. That restriction is removed by Bayes' theorem, which assigns a probabilistic meaning to f_{μ} . The theorem connects the quantity

we seek to limit (f_μ) to the experimental result n_{obs} and the intermediate quantities h [59]. It is given by

$$f^{\text{posterior}}(f_\mu | n_{obs}) = \frac{\int f(n_{obs} | f_\mu, h) f^{\text{prior}}(f_\mu, h) dh}{\iint f(n_{obs} | f_\mu, h) f^{\text{prior}}(f_\mu, h) dh df_\mu}, \quad (6-15)$$

where $f(n_{obs} | f_\mu, h)$ is the likelihood function, $f^{\text{prior}}(f_\mu, h)$ is the prior probability distribution function, and $f^{\text{posterior}}(f_\mu | n_{obs})$ is the posterior probability distribution function. The integral in the numerator is over the intermediate quantities h and the integral in the denominator is over the intermediate quantities and all possible values for f_μ . The input parameters are assumed to be independent, which means that the prior probability distribution function can be written as

$$f^{\text{prior}}(f_\mu, h) = f^{\text{prior}}(f_\mu) f^{\text{prior}}(h). \quad (6-16)$$

Since the prior $f^{\text{prior}}(f_\mu)$ reflects previous knowledge about the variable f_μ , many different functional forms have been used in the past. In this analysis, a flat distribution is used for the prior, following common Bayesian practice.

The symbol h represents the variables n_{bg} , \mathcal{E} , par , and ϕ_{in} . Each has a Gaussian distribution function with the uncertainty given in table 6-5. These are intermediate quantities that have a probability distribution, which is integrated over to obtain a confidence limit only for f_μ .

The likelihood function follows a Poisson distribution; it is given by

$$f(n_{obs} | f_\mu, h) = f(n_{obs} | n_{pred}) = \frac{e^{-n_{pred}} (n_{pred})^{n_{obs}}}{n_{obs}!}, \quad (6-17)$$

where n_{pred} denotes the mean number of events in the Poisson distribution, It is given by

$$n_{pred} = n_{pred}(n_{bg}, \mathcal{E}, par, \phi_{in}) = \phi_{in} \left(f_\mu \frac{\pi \alpha^2}{m_e^2} par \right) n_{te} \mathcal{E} + n_{bg}. \quad (6-18)$$

The Posterior Probability Distribution Function

The posterior probability distribution function from equation 6-15 gives the degree of belief in any value of f_μ for a fixed set of experimental parameters. This function is shown in figure 6-5 for $n_{obs} = 2$. It is obtained by repeating the integrals in equation 6-15 for many values of f_μ .

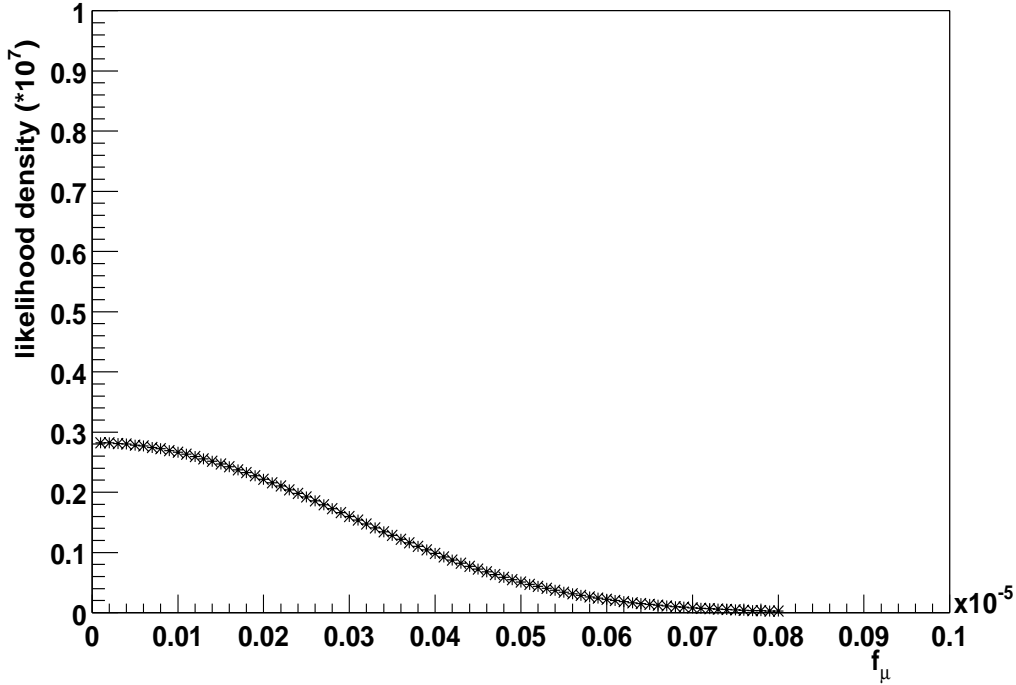


Figure 6-5. Posterior pdf from equation 6-15 for $n_{obs} = 2$.

The most likely value for the magnetic moment is $f_\mu = 0$, which is identical to the result obtained in the classical analysis. The 90% confidence limit for f_μ is 4.3×10^{-7} . It is also comparable to the limit obtained in the classical approach.

6.5 Analysis of Visually Selected Events

Events in the reduced data sample of visually selected events have the characteristics of neutrino-nucleon interactions. It was not necessary to apply the neutrino interaction cuts from step three and four of the analysis to these events. The two trigger cuts from step two were not applied to category three events, either.

The statistical data analysis follows the same steps that were explained in detail in section 6.4.

The Candidate Events

Four events remained from the visually selected event sample after all of the cuts. The first event is shown in figure 6-6.

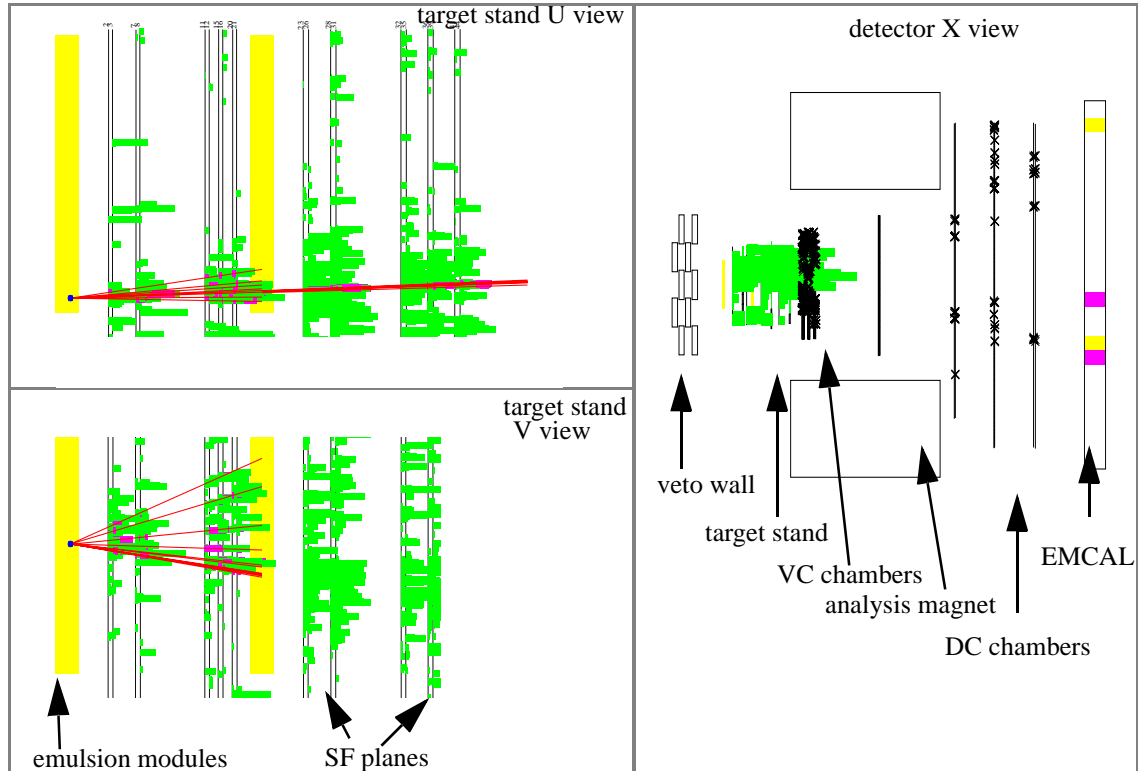


Figure 6-6. Three views of the first candidate event (run 2907, event 12929) in the visually selected sample. Each dark line corresponds to a final track. The size of a hit in the SF planes indicates its pulseheight.

The neutrino interacted in station one during period one. A particle shower has been reconstructed in the scintillating fiber planes downstream of station one and none of the particles in the shower could be reconstructed downstream of station three. The total signal measured in the calorimeter was 7GeV.

The event could have been produced by an electron-neutrino nucleon interaction in which the electron generated a large electromagnetic shower and many hadrons were produced in the interaction.

The second candidate event is shown in figure 6-7.

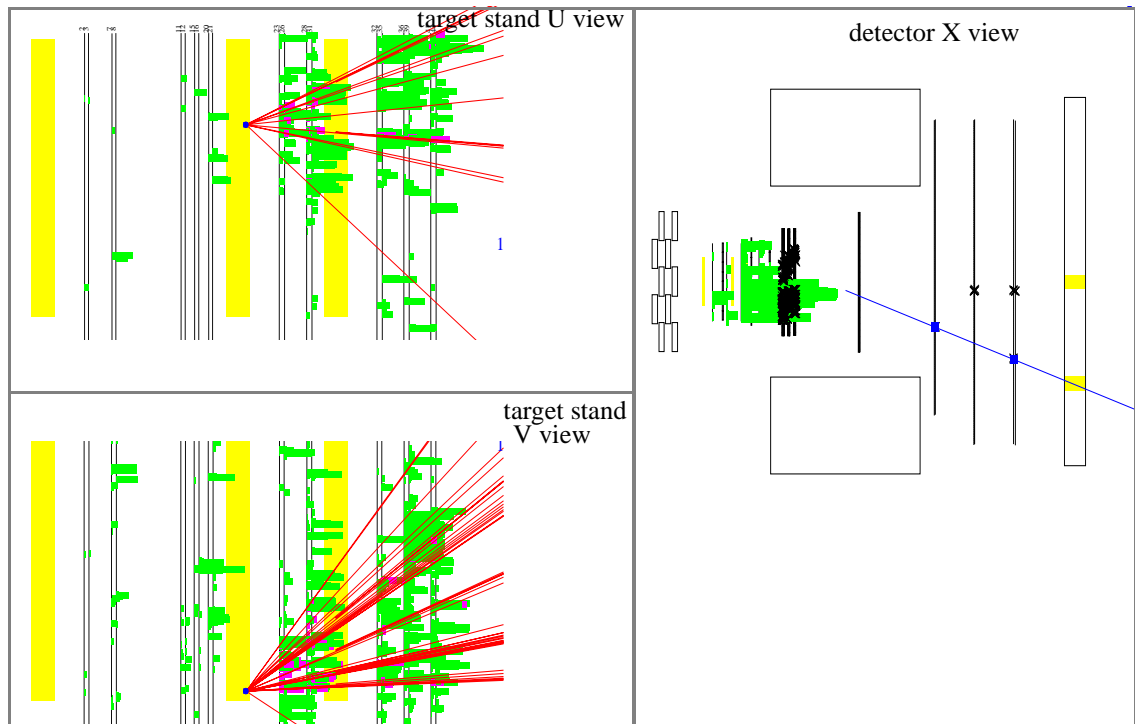


Figure 6-7. Same as figure 6-6 for the second candidate event (run 3024, event 11173) of the visually selected event sample.

The interaction occurred in station three during period two, at the edge of the fiducial volume. It produced a large particle shower that was also identified downstream of station four. Only two charged particles passed through the magnet and generated a small signal in the calorimeter.

The interaction was most likely produced by a neutral current interaction; the shower visible in the scintillating fibers was probably a purely hadronic shower.

The third candidate event is shown in figure 6-8.

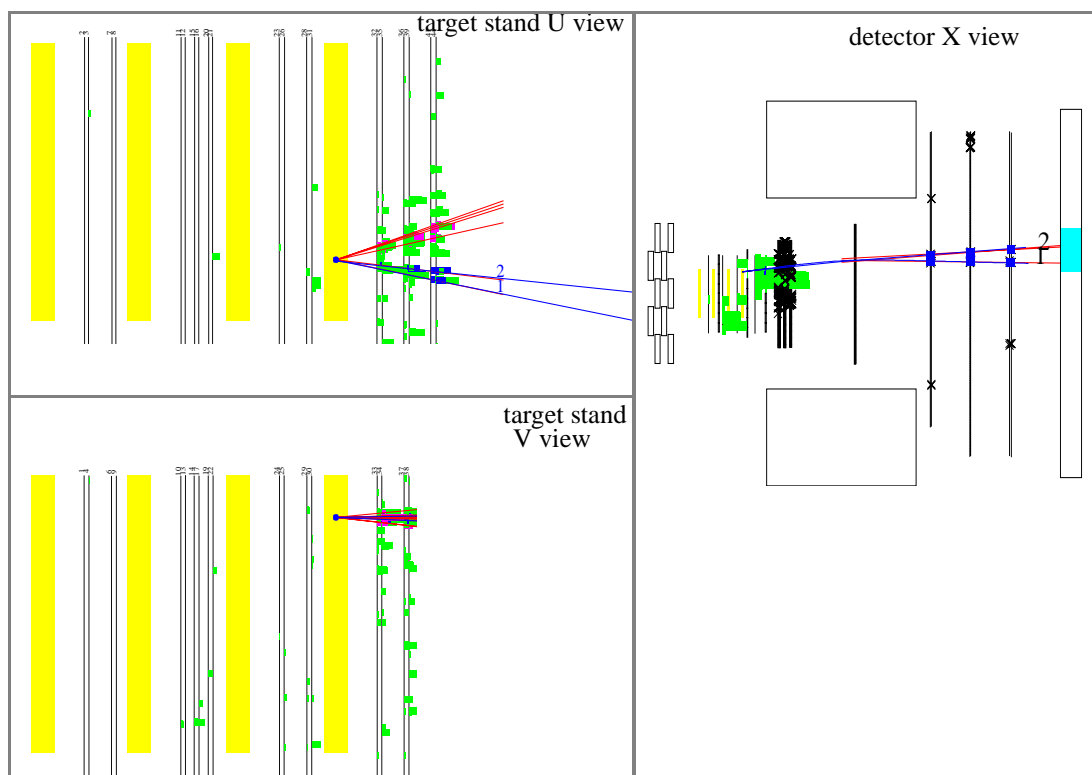


Figure 6-8. Same as figure 6-6 for the third candidate event (run 3138, event 3097) in the visually selected event sample.

The neutrino interaction occurred in station four during period three. Two particles from the shower passed through the analysis magnet. Track one had a measured momentum of 2.7GeV and a positive charge; a signal of 1GeV was associated with it in the calorimeter. Track two had a measured momentum of 13GeV, also a positive charge, and a signal of 7GeV was associated with it in the calorimeter.

The event was most likely produced by an electron-neutrino interaction in which the electron produced an electromagnetic shower in the lead wall downstream of the target region and two of the shower particles were identified in the calorimeter.

The fourth candidate event is shown in figure 6-9.

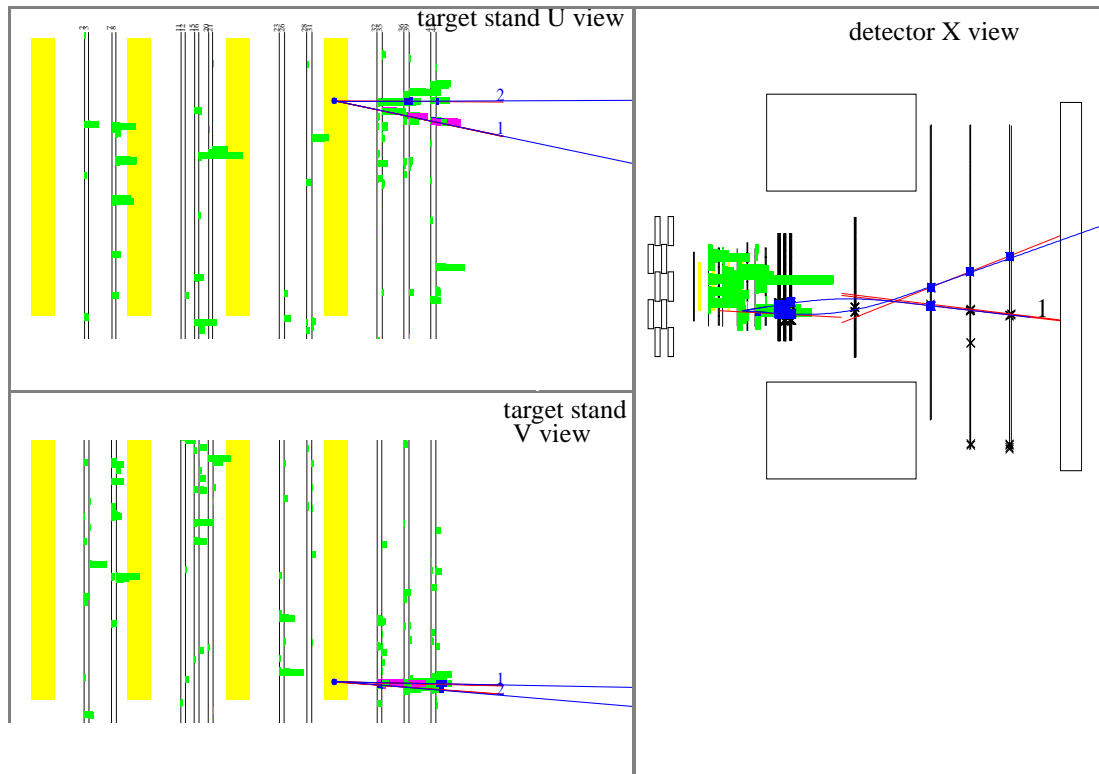


Figure 6-9. Same as figure 6-6 for the fourth candidate event (run 3273, event 10082) in the visually selected event sample.

The neutrino interaction occurred in station four during period four. Three vertex tracks were reconstructed; two of them were also identified downstream of the analysis magnet. One of the tracks had a positive charge, the other one a negative charge. Each of them had a measured momentum of about 1.2GeV and the signal measured in the calorimeter was less than 0.3GeV .

The event was most likely produced by a neutral-current interaction with a small momentum transfer from the scattered neutrino to the target nucleus.

The Number of Background Events

The number of neutrino-nucleon events that passed all of the cuts has to be modified due to two changes:

- Since only some of the cuts were applied to this event sample, the number of expected events is higher than in the previous analysis.
- The visual selection process accepted about 85% of the events that passed the software neutrino event selection cuts, which reduced the number of expected background events.

Altogether, 6.0 neutrino-nucleon interactions passed all of the cuts, 1.0 events in period one, 2.0 events in period two, 1.2 events in period three, and 1.8 events in period 4.

Statistical Analysis

The observed number of four events is consistent with zero neutrino magnetic moment interactions at the expected number of 6.0 events from background processes. The resulting 90% confidence limit for the tau neutrino magnetic moment is again found with the Frequentist and the Bayesian method.

The Frequentist analysis gives a limit for the number of found events of 2.85. That corresponds to a 90% confidence limit for the cross section of $\sigma_{\text{tot}} \leq 2.9 \times 10^{-41} \text{ m}^2$ and the limit for the magnetic moment is $f_{\mu} \leq 5.2 \times 10^{-7}$.

The Bayesian analysis was repeated with the same systematic uncertainties. It gives a 90% confidence limit of $f_{\mu} \leq 5.2 \times 10^{-7}$.

The limits obtained in the analysis of category three events are slightly higher than the limits found in the analysis of software selected events. They confirm the previous result and indicate that the selection cuts in steps three and step four were free of systematic errors.

7 Conclusions

The search for neutrino-electron interactions in the E872 data set has yielded two candidate events with a mean expected background from neutrino-nucleon scattering of 4.4 events. This result is consistent with the Standard Model at the 90% confidence level; it shows no evidence for interactions beyond the Standard Model.

The sensitivity of the search is expressed by setting an upper limit on the tau neutrino magnetic moment. Since no excess of interactions has been recorded, a 90% upper confidence limit for the tau neutrino magnetic moment is deduced. Two different approaches to the statistical analysis have been presented: The classical approach views probability as limiting frequency; it is widely used in neutrino physics and gives a 90% confidence limit for the magnetic moment of $\mu_{\nu_\tau} \leq 4.2 \times 10^{-7} \mu_B$. The Bayesian approach views probability as a degree of belief, which incorporates systematic uncertainty. In this approach, a probability distribution function is found for the parameter under investigation that requires a prior probability distribution in its calculation. The Bayesian approach gives a 90% upper confidence limit for the magnetic moment of $\mu_{\nu_\tau} \leq 4.3 \times 10^{-7} \mu_B$ with a prior that is flat in the magnetic moment.

Both statistical analysis methods give similar results. The inclusion of systematic uncertainty does not have a big effect on the confidence limit since the statistical uncertainty due to the small number of events ($\sqrt{2}/2 = 71\%$) is much larger than the systematic uncertainty (about 25%).

The analysis of the smaller set of neutrino interaction candidate events gives a 90% confidence limit of $\mu_{\nu_\tau} \leq 5.2 \times 10^{-7} \mu_B$ with both statistical analysis methods. Only about half of the magnetic moment selection cuts were applied to this sample, which therefore provides a test of the previous analysis.

Each of the confidence limits for the tau neutrino magnetic moment is an improvement over the current published value [8]. Moreover, none of the previous experiments measuring the tau neutrino magnetic moment has had any evidence for the presence of tau neutrinos in the neutrino beam. DONUT is the first experiment to observe the interaction of tau neutrinos directly (see references [38] and [39]), which increases the confidence in the obtained limit and also provides an estimate for the tau neutrino flux.

The confidence limit is four orders of magnitude larger than the current upper limit for the other neutrino flavors; this discrepancy is due to the relatively small tau neutrino flux. The limit could be improved in future experiments by increasing the flux, which could be achieved by repeating the experiment with a larger number of protons on target.

Alternatively, the oscillation of muon-neutrinos to tau-neutrinos could be exploited in long-baseline neutrino experiment. The atmospheric neutrino anomaly [1] suggests oscillations between muon-neutrinos and tau-neutrinos with a characteristic distance of a few hundred kilometers. Currently, three experiments are running or planned to look for these oscillations (see references [60], [61], and [62]) and to confirm the oscillation mode. If the oscillation hypothesis is true, about half of the muon-neutrinos should oscillate into tau-neutrinos, which means that the tau-neutrino flux will be similar to the muon-neutrino flux at the far detector. These experiments would then be sensitive to a much lower tau-neutrino magnetic moment.

Appendix A Neutrino Beam

The interactions of protons and nuclei create a large number of quarks that combine to particles. The production cross section decreases with increasing quark mass; light quarks are produced more abundantly than heavy quarks. Most of the particles interact and lose energy in the target material before they decay. Only short-lived particles decay before they can interact, and these decays produce the prompt neutrino beam. The lightest short-lived particles are D mesons; the D decay is therefore the main source of electron- and muon-neutrinos. The lightest particle with a significant branching fraction to tau-neutrinos is the D_s meson.

The following sections discuss the production and decay properties of D mesons in a fixed target experiment with a proton beam of 800GeV.

A.1 The D Production Cross Section

The D^+ (D^0) meson consists of a charm quark and a down (up) quark. Many experiments have studied the D production parameters with proton and pion beams and a variety of targets. A summary of the experimental results is shown in table A-1.

Experiment (year published)	particle, energy	D^{+-} production cross section ($\mu\text{barn} / \text{nucleon}$)	D^0 production cross section ($\mu\text{barn} / \text{nucleon}$)	D_s production cross section ($\mu\text{barn} / \text{nucleon}$)	parameter range
E653 (1991) [63]	p, 800GeV/c	38 ± 16.6	38 ± 13.3	not measured	all x_F
E653 (1992) [64]	π , 600GeV/c	8.66 ± 2	22.05 ± 5	not measured	$x_F > 0$

Table A-1. Fixed target open charm production data. The cross section is given for the parameter range in the “condition” column. The variable x_F is explained in section A.4.

Experi- ment (year published)	particle, energy	D^{+-} produc- tion cross section ($\mu\text{barn} /$ nucleon)	D^0 pro- duction cross section ($\mu\text{barn} /$ nucleon)	D_s produc- tion cross section ($\mu\text{barn} /$ nucleon)	parameter range
NA32 (1991) [65]	π , 230GeV/c	3.2 ± 0.73	7.78 ± 0.54	1.29 ± 0.37^a	$x_F > 0$
E743 (1988) [66]	p, 800GeV/c	26 ± 9	22 ± 9.7	not measured	all
E691 (1989) [67]	γ , 80- 230GeV/c	1.35 ± 0.25^a	2.64 ± 0.41^a	0.36 ± 0.1^a	$x_F > 0.2$
E769 (1996) [68]	π , 250GeV/c	3.2 ± 0.28	7.2 ± 0.64	2.0 ± 0.45	$x_F > 0$
E769 (1996) [68]	π , 210GeV/c	1.7 ± 0.32	6.3 ± 1.1	not measured	$x_F > 0$
E769 (1996) [68]	K, 250GeV/c	3.0 ± 0.35	7.2 ± 1.1	3.0 ± 0.9	$x_F > 0$
E769 (1996) [68]	K, 210GeV/c	3.3 ± 1.0	not measured	not measured	$x_F > 0$
E769 (1996) [68]	p, 250GeV/c	3.2 ± 0.5	5.4 ± 1.4	1.5 ± 1.5	$x_F > 0$
E706 (1997) [69]	π , 515GeV/c	11.4 ± 4.3	not measured	not measured	$x_F > 0$
WA92 (1997) [70]	π , 350GeV/c	3.28 ± 0.3	7.78 ± 0.54	1.29 ± 0.37	$x_F > 0$

Table A-1. Fixed target open charm production data. The cross section is given for the parameter range in the “condition” column. The variable x_F is explained in section A.4.

Experiment (year published)	particle, energy	D^{+-} production cross section ($\mu\text{barn} / \text{nucleon}$)	D^0 production cross section ($\mu\text{barn} / \text{nucleon}$)	D_s production cross section ($\mu\text{barn} / \text{nucleon}$)	parameter range
E789 (1997) ([71] and [72])	p, 800GeV/c	not measured	20.9 ± 3.5	not measured	all x_F ^b
Helios (1996) [73]	p, 450GeV	10 ± 5	27 ± 13	not measured	many restrictions ^c

Table A-1. Fixed target open charm production data. The cross section is given for the parameter range in the “condition” column. The variable x_F is explained in section A.4.

- a. The cross section is calculated using the value for (cross section times branching ratio) given in the paper and the current branching ratio from [14].
- b. The measurement was done for x_F near zero and extrapolated to all $x_F > 0$ using the distributions given in [63] and [66] ($n=7.7$, $b=0.8\text{GeV}^{-2}$).
- c. The experiment measured the cross section for production of electron-muon pairs in the forward direction with missing energy and obtained a result for the total $c\bar{c}$ cross section. The mean $D^{+-}D^0$ ratio is used to deduce the individual cross sections.

The last column of table A-1 lists the parameter range for which the quoted production cross section is valid. The Feynman variable x_F is defined in section A.4 and theoretical calculations show that the cross section σ for all x_F is given by $\sigma \approx 1.6\sigma(x_F > 0)$ for pions and $\sigma \approx 2\sigma(x_F > 0)$ for protons [74]. The experiments were done with different targets, and the values in table A-1 have been calculated assuming a cross section proportional to A^1 , where A is the atomic number of the target (see section A.3).

The cross section for all x_F is shown in figures A-1 and A-2 for all of the experiments listed in table A-1.

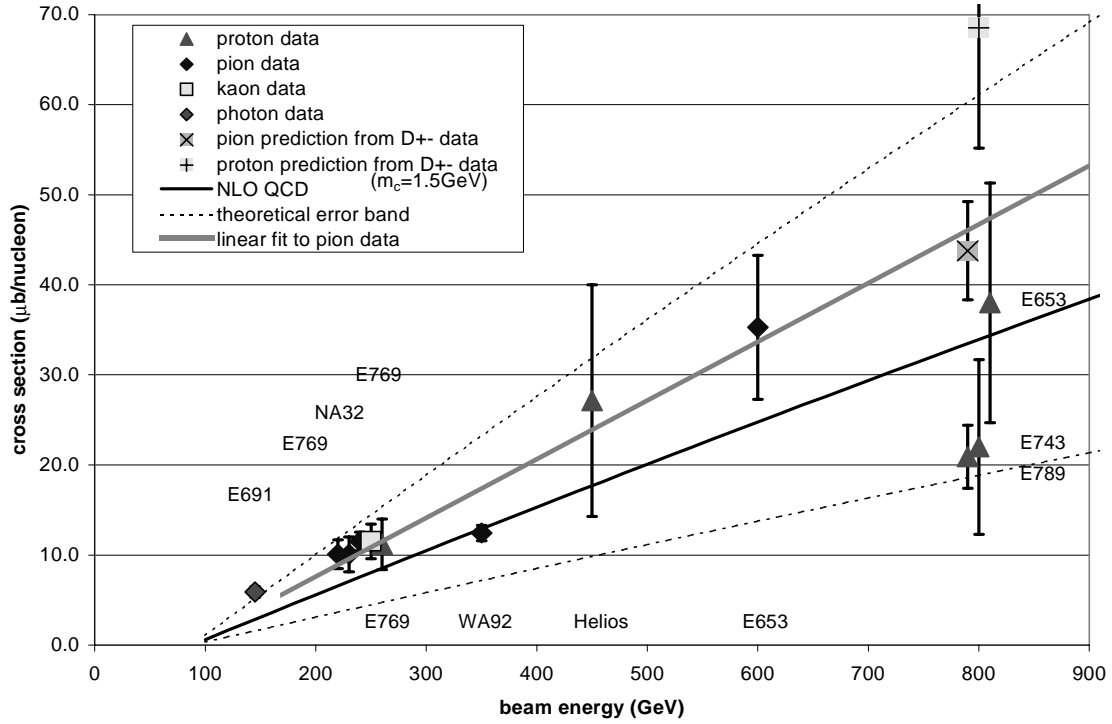


Figure A-1. D^0 production cross section for several different energies. The QCD prediction is from reference [68]. The theoretical error band is an underestimate of the actual theoretical uncertainty. It is obtained by varying the normalization scale [74].

The two figures show the data points together with a next-to-leading-order QCD calculation (NLOQCD) [68]. The uncertainty in the theoretical calculation is due mostly to the unknown charm quark mass m_c . Since it is small, the perturbative expansion in terms of the strong coupling constant α_s does not converge quickly and the contribution from the next-to-leading-order terms (order α_s^3) is comparable in size to the leading term (order α_s). The factorization and renormalization scales in the QCD calculations also depend on m_c . Altogether, a variation in m_c between 1.2GeV and 1.8GeV changes the theoretical calculation by a factor of eight [75]. Although the absolute scale of the theoretical calculation is not known very well, the shape of the curve in figure A-1 is the same for different values of

m_c . This makes it possible to compare cross section results at different energies by scaling them to a common energy.

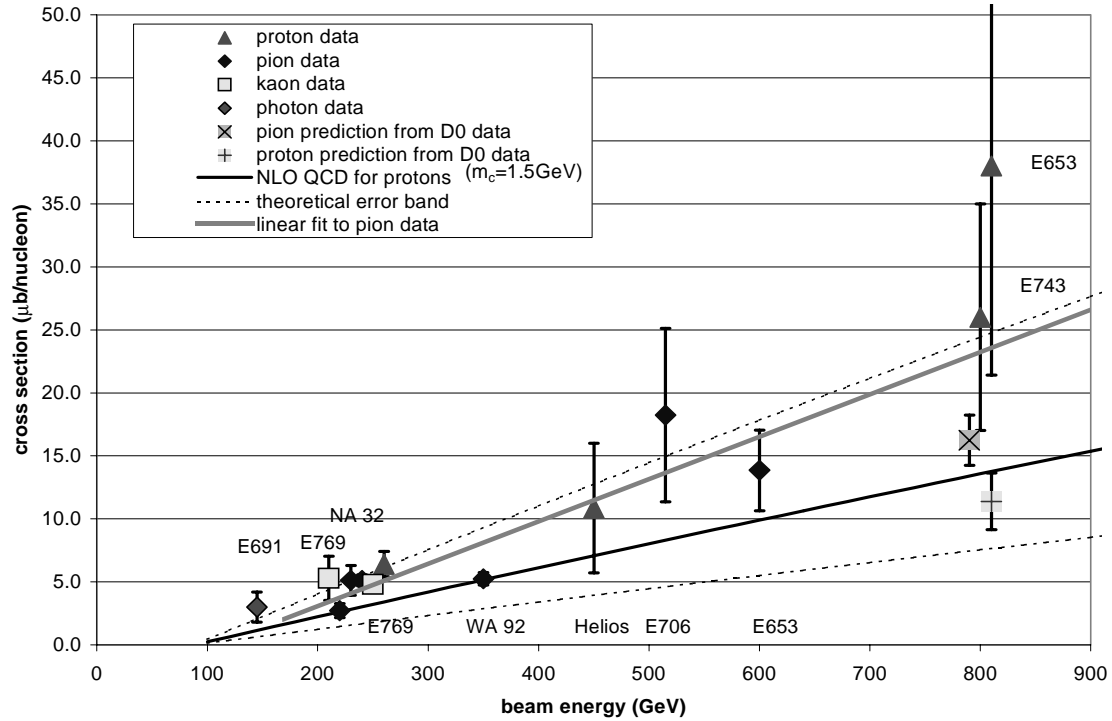


Figure A-2. Same as figure A-1, but for D^+ production cross section. The prediction from D^0 data is explained in the text.

The ratio of D^+ to D^0 production cross sections has also been measured by many experiments. The expected D^+ production cross section can then be obtained from the average D^0 production cross section and vice versa. The average is found by scaling the experimental values along the theoretical line in figure A-1 to an energy of 800 GeV. The experimental uncertainty is used for weighting the different experiments. The uncertainty quoted by E789 is so small that it would dominate the average; it has been doubled in the weighted average.

To estimate the accuracy of the proton data at 800 GeV, the ratio of D^+ to D^0 production is found for all experiments that measured both production cross sections. This ratio is

shown in figure A-3, it can be determined accurately by the experiments because systematic uncertainties that affect the total cross section cancel out in this measurement.

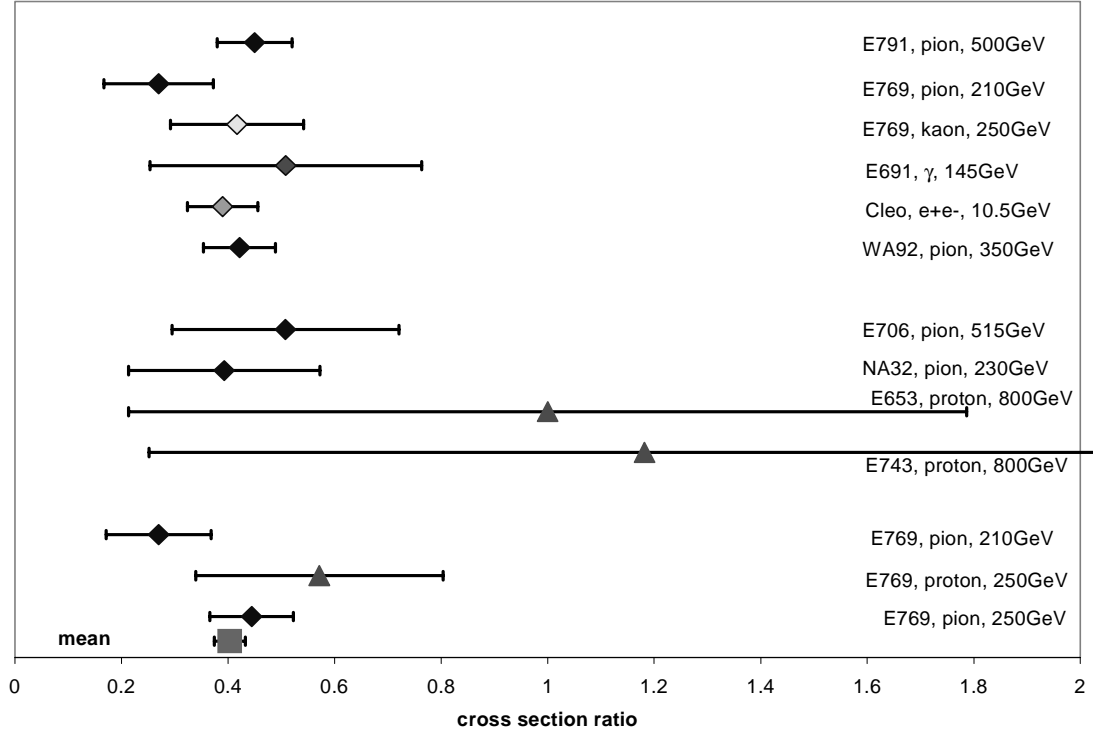


Figure A-3. Ratio of the production cross sections for D^{++} and D^0 .

Also included in figure A-3 is data from the CLEO e^+e^- collider [76], where charm quarks are produced in the QED process $e^+e^- \rightarrow c\bar{c}$. The cross section for this process can be calculated accurately. The ratio in figure A-3 depends only on details of the hadronization process. The CLEO experiment quotes the production cross section times branching ratio. The current branching ratios are used to calculate the cross section.

The D^{++} over D^0 production ratio can be estimated theoretically with a simple argument: It is assumed that each D particle state is produced equally likely, meaning that it is equally likely to produce isoscalars (D^{+-} and D^0) and three times more likely to produce isovectors (D^{*+-} and D^{*0}). These excited states decay to D^{+-} and D^0 with the following probabilities:

$$\begin{aligned}
D^{*-} &\rightarrow D^{*-} \pi^0, D^{*-} \gamma & 31.7\% \\
D^{*+} &\rightarrow D^0 \pi^{+-} & 68.3\% \\
D^{*0} &\rightarrow D^{+-} X & 0\% \\
D^{*0} &\rightarrow D^0 \pi^0, D^0 \gamma & 100\%
\end{aligned} \tag{A-1}$$

Adding up the individual contributions, the D^{+-} over D^0 production ratio is 0.32, which is consistent with the data in figure A-3. The higher angular momentum states are omitted in this calculation because their production cross section is small [77].

Combining the various measurements, the mean value for the ratio of the D^{+-} and D^0 production cross sections is 0.40 ± 0.03 . The various data points shown in figure A-3 agree within their error bars, which is not true for the individual cross sections for proton beams in figures A-1 and A-2. This indicates that the experiments underestimated their systematic uncertainties.

A comparison of the proton beam data to the pion beam data and the theoretical calculations gives an indication which production cross section to use. The proton production cross section for D^{+-} is higher than expected and the production cross section for D^0 is lower than expected. The point “prediction from D^{+-} data” in figure A-1 is significantly higher than all of the measurements, which indicates that the measurement of the D^{+-} production cross section was too high. The point “prediction from D^0 data” in figure A-2 is slightly lower than the other measurements, but inside the theoretical uncertainty band. This cross section is therefore used in further calculations rather than the measurements of figure A-1.

The proton production cross sections at 800GeV are $\sigma_p(D^{+-}) = (11.3 \pm 2.2)\mu\text{B/nucleon}$ and $\sigma_p(D^0) = (27.4 \pm 2.6)\mu\text{B/nucleon}$. All of the data points agree with these cross sections within their error bars.

The pion production cross section is understood better. The average cross section at 800GeV is $\sigma_\pi(D^{+-}) = (11 \pm 1)\mu\text{B/nucleon}$ and $\sigma_\pi(D^0) = (28 \pm 2.5)\mu\text{B/nucleon}$, which is consistent with the ratio in figure A-3. These values are calculated from the data points only since no inconsistencies were found for pion beams.

These pion and proton production cross sections are approximately equal in size, which is compatible with the J/Ψ production by pions and protons. The two are connected since the quark content of the J/Ψ meson is $c\bar{c}$ and all D mesons contain one c quark. The J/Ψ production cross section has been measured extensively [78], and the two curves are shown in figure A-4.

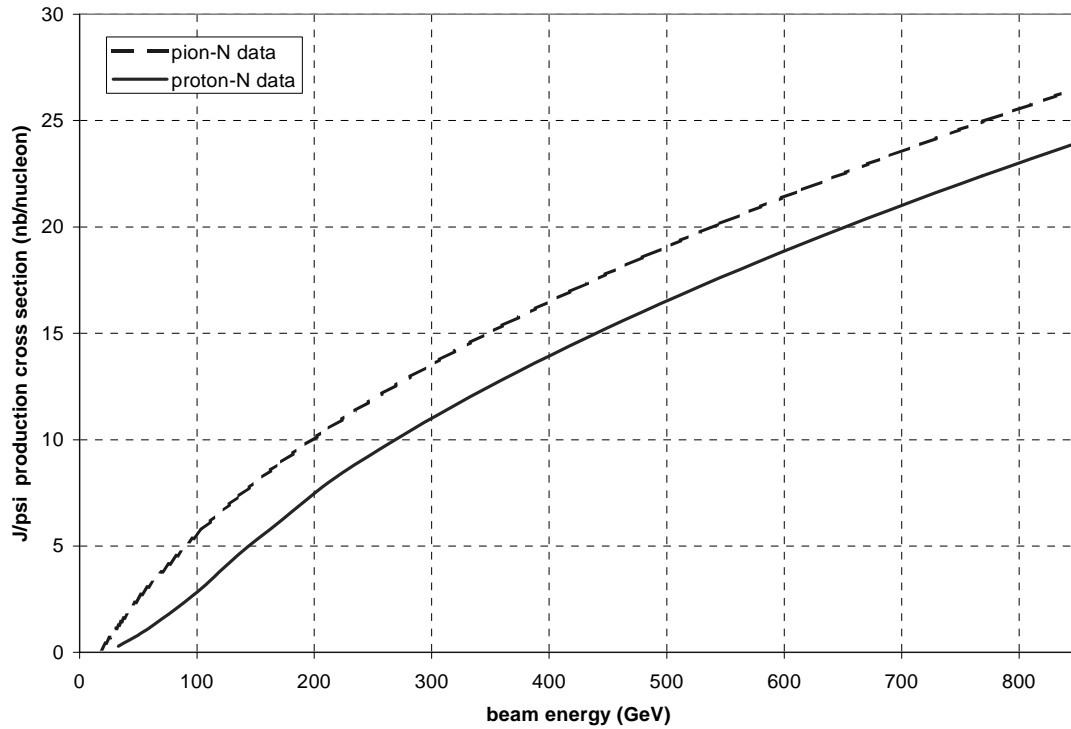


Figure A-4. J/ψ production cross section for pion and proton beams.

The production cross section is a factor of 1.1 times larger for pions than for protons at a beam energy of 800GeV.

The same comparison can be made for bottom production. Unfortunately, there is not enough experimental data to obtain the production cross sections for pions and protons. However, the large bottom mass makes the QCD calculation more accurate than for charm production. The calculated ratio for bottom production between pion and proton beams is about 1.5 in a next-to-leading order calculation [75].

All of the previous arguments support the result obtained for the D production cross section.

An asymmetry exists between D^+ and D^- production due to the leading particle effect. The D^- is leading in a proton beam experiment because it has a d quark in common with the beam. The D^+ is the non-leading particle in this case. There is an enhancement of the forward production of leading particles. This asymmetry has been measured in a pion beam [79]; it is negligible for small longitudinal momentum and small transverse momentum. This asymmetry therefore does not affect the total production rate of D^+ and D^- particles.

A.2 The D_s Production Cross Section

The D_s meson consists of a c quark and a s antiquark, making it heavier and its production cross section smaller than the D meson production cross section.

Many of the experiments mentioned in the previous section have also measured the cross section for D_s production, and the results are included in table A-1. The ratios of the D_s over D^0 and the D_s over D^{+-} production cross sections are shown in figures A-5 and A-6.

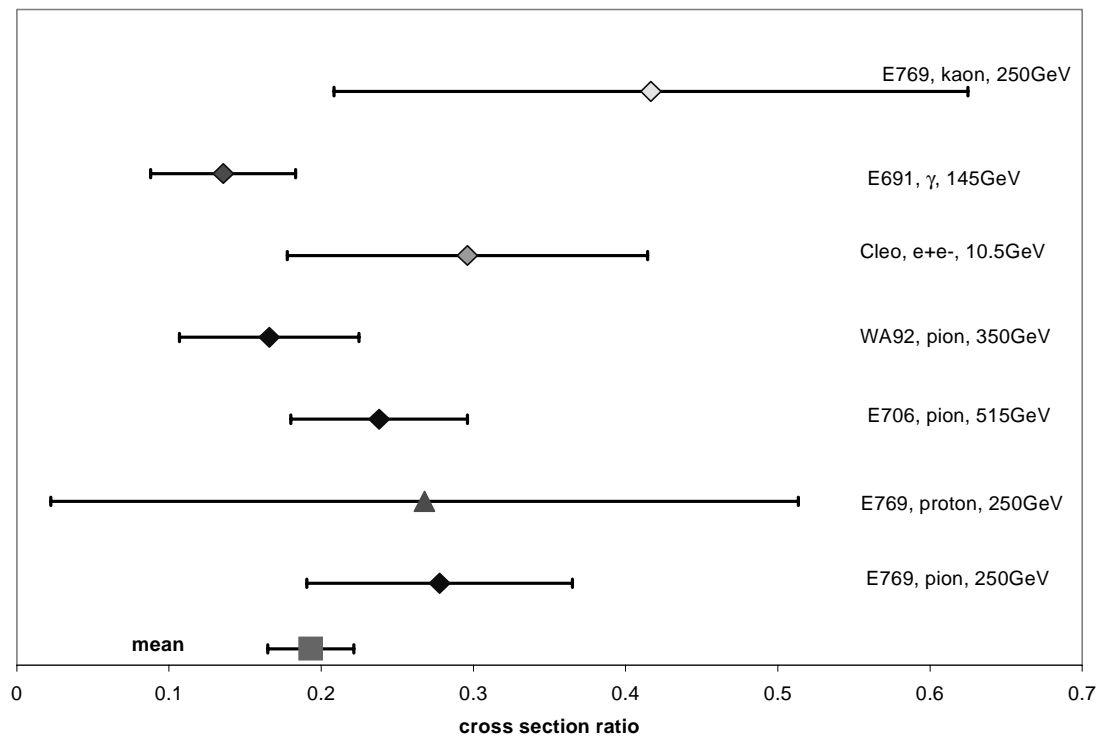


Figure A-5. Measured D_s over D^0 production cross section ratio from various experiments. The kaon data was not used to calculate the mean.

The experimental values for each of the two ratios agree within their error bars. The value for the D_s over D^{+-} ratio can be compared to the K^{+-}/π^{+-} production ratio, which has recently been measured to be about 0.1 for a proton beam with an energy of 450GeV [80]. However, since the D^{+-} and D^0 are not produced equally (see figure A-3), the K^{+-}/π^{+-} ratio has to be corrected to compare it to the D_s over D^{+-} ratio. When a strange quark is produced, it can not only end up as a K^{+-} but also as a neutral kaon. That is not true for D_s production, since that has no neutral state. The corrected result for the predicted D_s over D^{+-} ratio is therefore 0.5, which is consistent with the experimental values shown in figure A-6.

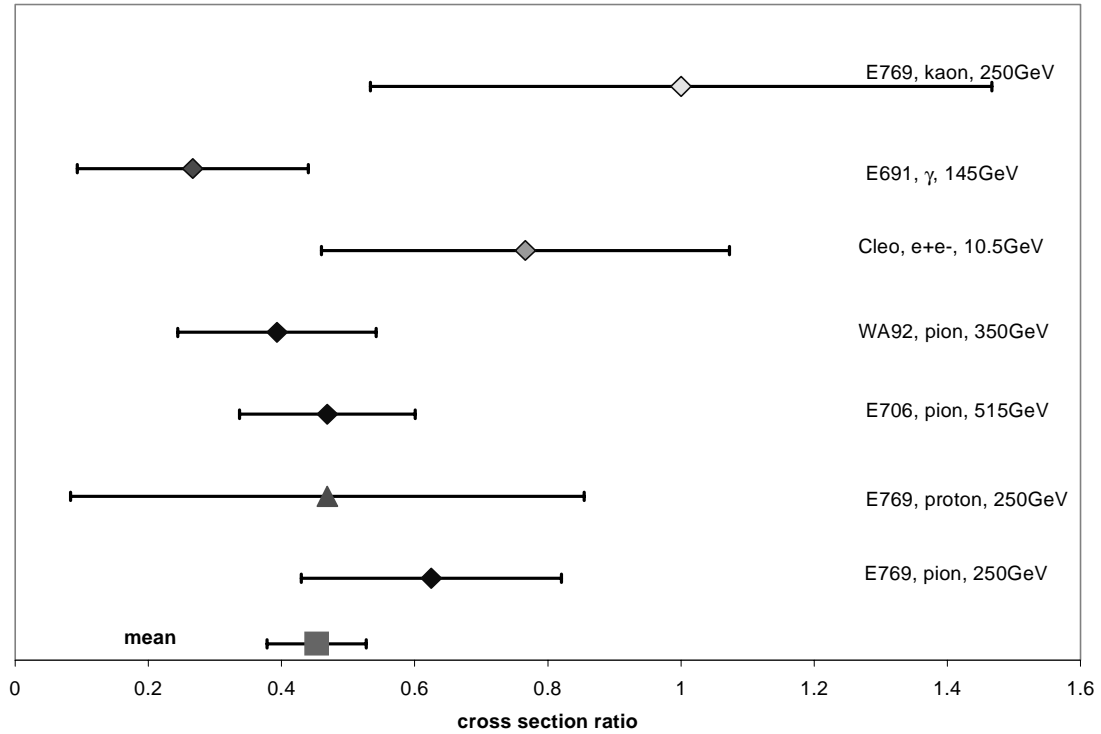


Figure A-6. D_s over D^{+-} production cross section ratio from various experiments. The kaon data was not used to calculate the mean.

The absolute D_s production cross section is calculated from the ratios and the D^{+-} and D^0 cross sections. The result for a proton beam is shown in figure A-7.

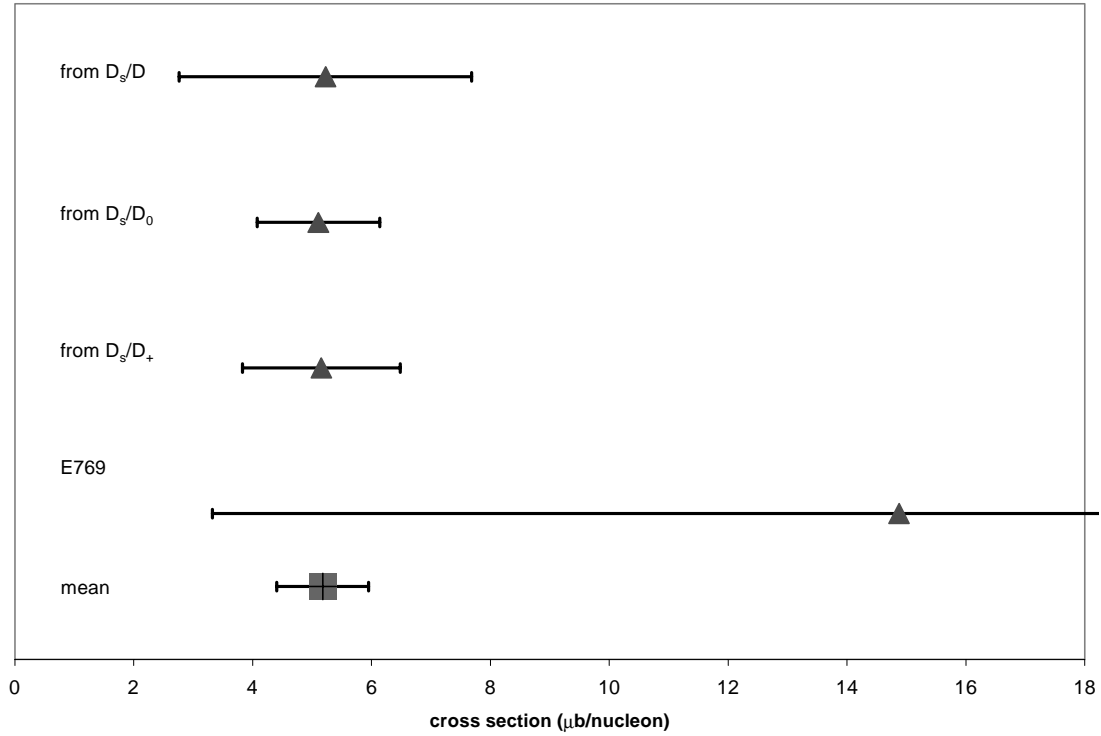


Figure A-7. D_s production cross section for a proton beam of 800 GeV. The D_s/D^0 value was found using only the experimental data for D^0 production, the D_s/D^{+-} value was found using the predicted value for D^{+-} production from D^0 data.

The three different calculations of the cross section give consistent results. However, using only the experimental D^{+-} results, the prediction for the D_s production cross section is a factor of two larger than the found mean. This is another indication that the measured D^{+-} production cross section is too large.

The mean value is for the D_s production cross section is $5.2 \mu\text{b/nucleon}$. The direct experimental result from experiment E769 has a large uncertainty and it can not be used to reduce the overall uncertainty.

Figure A-8 shows the D_s production cross section for pion beams.

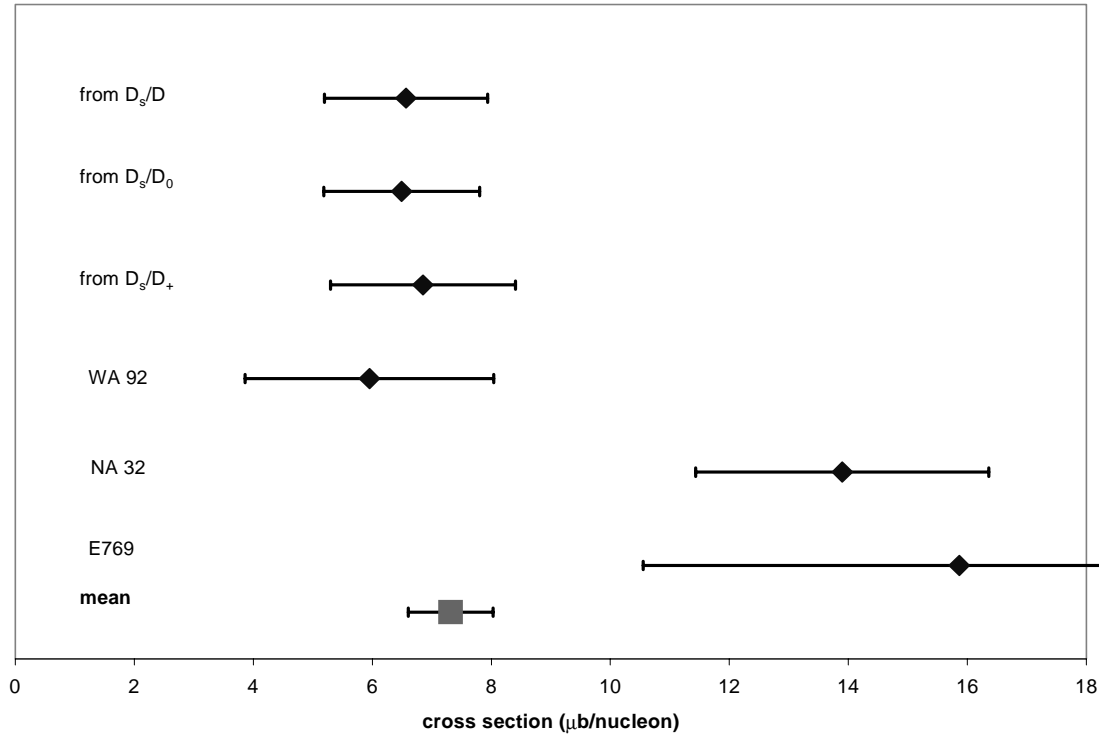


Figure A-8. D_s production cross section for a pion beam of 800 GeV.

Here, the values calculated from the D_s/D^{++} and D_s/D^0 ratios are consistent with each other, with the D_s/D ratio, and with the direct measurements. The mean value of $7.3\mu\text{b/nucleon}$ is comparable to the D_s/D value for a proton beam. The arguments that were presented for the D production cross section should still hold, and the value should be about the same for pion and proton beams.

There is also a leading particle effect in D_s production. Following the same argument as in section A.1 however, this asymmetry is small for the total production cross section.

A.3 The Nuclear Dependence of the Production Cross Section

The total production cross section depends also on the target material, which has been measured by several experiments. The nuclear dependence of the production cross section is written as

$$\sigma(A) = \sigma(1)A^\alpha, \quad (\text{A-2})$$

and the parameter α is found by experiments. From simple nucleon counting, it can be expected that the cross section is a linear function of A , the atomic mass. The experimental results show a similar behavior; the total inelastic cross section in pion-nucleon collisions is proportional to $A^{0.75}$, while the total inelastic cross section in proton-nucleon collisions is proportional to $A^{0.7}$ [81].

Experiment	beam, energy	α
WA 92 [70]	pion, 350GeV	0.95 ± 0.07
E789 [72]	proton, 800GeV	1.02 ± 0.04
E769 [82]	pion, 250GeV	1.0 ± 0.06
WA 82 [83]	pion, 340GeV	0.92 ± 0.06
mean		0.986 ± 0.027

Table A-2. Experimental values for the parameter α from equation A-2.

The measurements for D production are shown in table A-2. They are all consistent with a linear A dependence, and a value of $\alpha = 1$ is therefore used.

A.4 The x_F and p_T Dependence of the Production Cross Section

The energy- and momentum-distribution of the D mesons determines the energy spectrum of the neutrino beam. The longitudinal momentum fraction is given by x_F ; it can be calculated in the center of mass frame as

$$x_F = \frac{2p_z^{cm}}{\sqrt{s}}. \quad (\text{A-3})$$

Here p_z^{cm} is the particle momentum in the direction of the incoming beam and the Mandelstam variable s gives the total center of mass energy of the collision. The transverse momentum p_T is given by

$$p_T^2 = p_x^2 + p_y^2, \quad (\text{A-4})$$

where p_x and p_y are the momentum components perpendicular to the beam direction. They do not change in a Lorentz transformation to the center of mass frame of the system.

The dependence of the production cross section on x_F and p_T is typically written as

$$\frac{d\sigma}{dx_F dp_T^2} = \sigma_0 (1 - |x_F|)^n \exp(-bp_T^2), \quad (\text{A-5})$$

which is a phenomenological approximation to the observed spectrum [75]. The parameters n and b are determined experimentally; once they are found, the normalization σ_0 is calculated from the total cross section σ as

$$\sigma_0 = \frac{1}{2} b(n+1) \sigma. \quad (\text{A-6})$$

Equation A-5 describes the data well in the forward region of large x_F and small p_T that is important in this experiment.

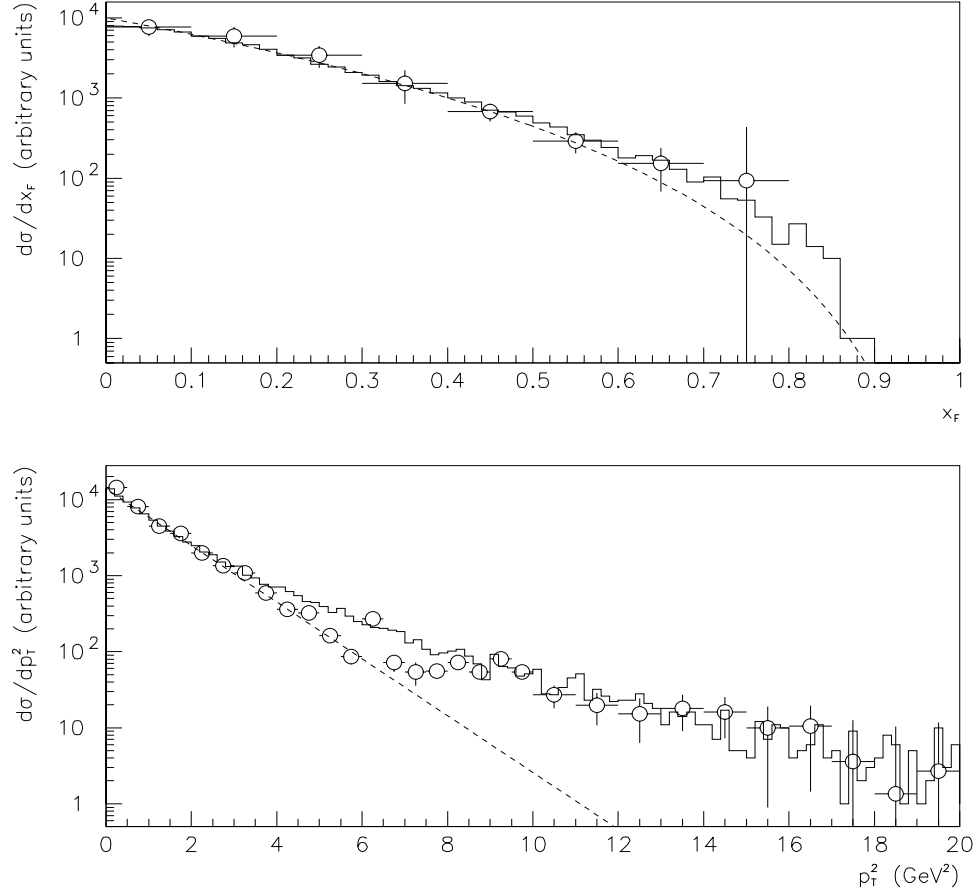


Figure A-9. x_F and p_T dependence of the differential cross section for charm production. The solid line is from a Pythia Monte Carlo run, the dashed line is from equation A-5 with $n=4.5$ and $b=0.86$. The data points are from experiment WA 92 [70].

The parameterization of equation A-5 is compared to data from a pion beam of 350GeV [70] and a Pythia Monte Carlo calculation (references [84], [85], and [86]) in figure A-9. The default parameters were used in the Monte Carlo calculation, except that the charm quark mass was set to 1.5GeV. The agreement between data, equation A-5, and Pythia is very good for the x_F dependence, but not for the p_T dependence. Data and equation A-5 agree for values of $p_T^2 < 5\text{GeV}^2$, but for larger transverse momenta, the approximation falls off too quickly. The Monte Carlo calculation conversely agrees with the data over the entire p_T range. It should also be noted that at $p_T^2 \approx 5\text{GeV}^2$, the differential cross section

is two orders of magnitude below its maximum value and the discrepancy between data and equation A-5 only has a very small effect on the total cross section. Moreover, since the emulsion target is 35m away from the proton beam target, only D mesons with a small transverse momentum will typically produce neutrinos that interact in the target.

Several experiments have measured the x_F and p_T dependence in pion beams (WA92 [70], E769 [68] and [87], WA82 [83], E653 [64], WA75 [88], NA32 [65] and [89]) and in proton beams (E769 [68], NA32 [89], E743 [66], E653 [63]). The experimental results for the parameters b and n are shown in figures A-10 and A-11.

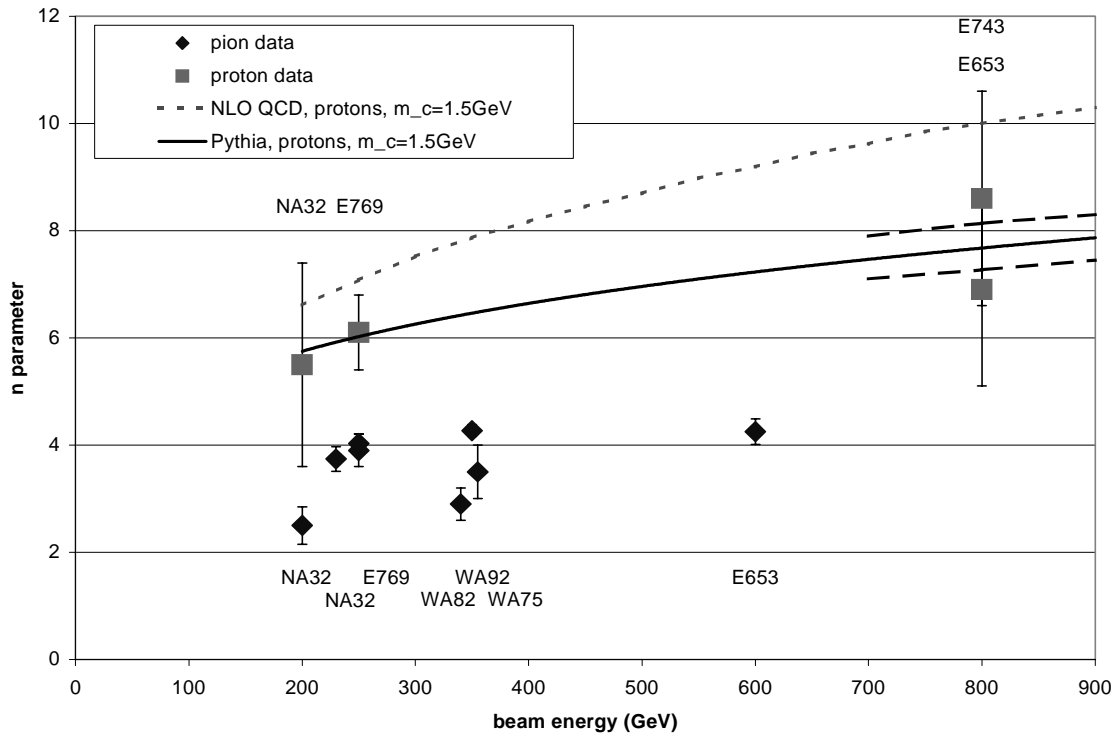


Figure A-10. Parameter n from equation A-5 versus beam energy for several different fixed target charm production experiments. The NLO QCD calculation is given by the short dashes. The solid line is the Pythia calculation for charm quarks. The dashed line on the right hand side of the figure shows the variation in n when the charm quark mass is changed between 1.2GeV and 1.8GeV in the Pythia calculation.

The default parameters were used in the QCD calculation, with a charm quark mass of 1.5GeV [90]. The calculation was done for a proton beam and the outgoing particle was the charm quark rather than the D meson. The parameter b was found from a fit to equation A-5.

Both Pythia and the NLO QCD calculation show the correct behavior: the parameter n increases slightly with increasing beam energy while the parameter b decreases. The QCD calculation gives results that are larger than Pythia for n and b .

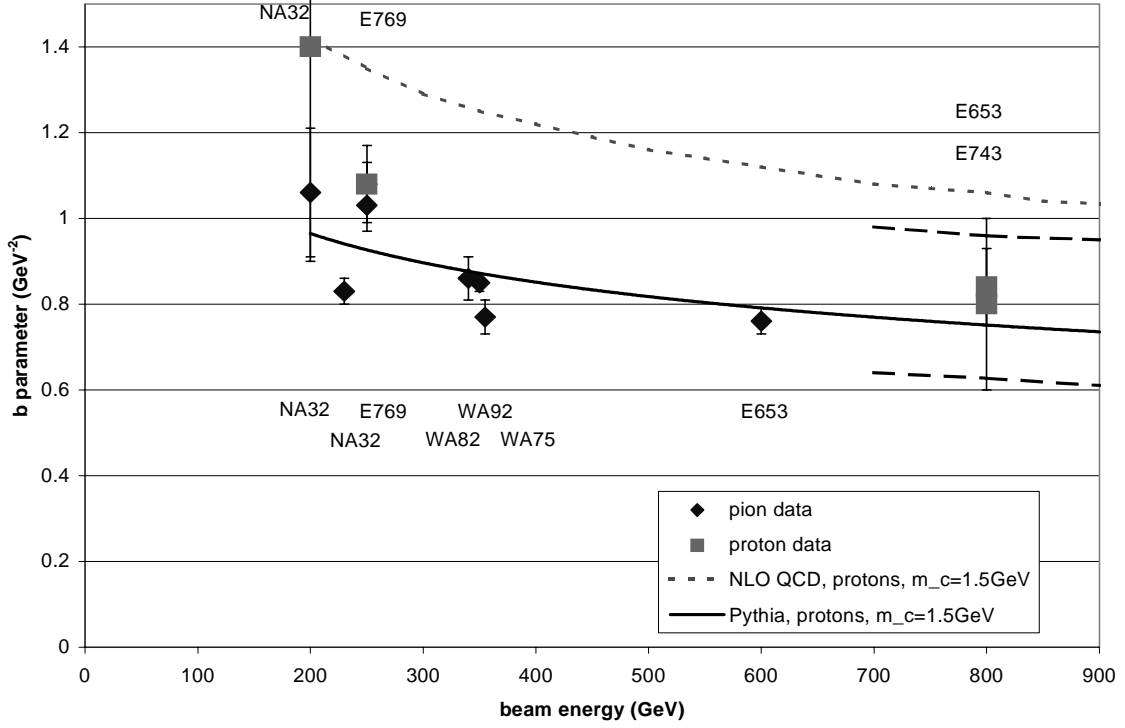


Figure A-11. Same as figure A-10, but for the parameter b .

The parameter b depends on the fit interval. In the figures, the interval for p_T^2 is $0-4\text{GeV}^2$, and a variation in the p_T^2 fit interval from $0-3\text{GeV}^2$ to $0-7\text{GeV}^2$ changes b from 0.83 to 0.64. The different experiments use fit intervals ranging between $0-4\text{GeV}^2$ and $0-10\text{GeV}^2$ and consequently obtain different values for b . Nevertheless, it is possible to correct for the different intervals by using the fit results from Pythia. For the proton data this correction does not influence the result very much since the error bars are comparatively large. For the pion data the correction is recognizable in figure A-13. The data points are much closer to the Pythia prediction.

The differences in the p_T^2 interval similarly affect the fit result for n , but only slightly. However, more variation is again caused by different fit intervals in x_F . The fit to the Pythia

curve for pions changes n between 4.44 and 3.82 when the fit interval is changed from $0 < x_F < 0.5$ to $0.1 < x_F < 0.7$.

The data points are also corrected for the different fit intervals in x_F and p_T^2 . The result is shown in figures A-12 and A-13.

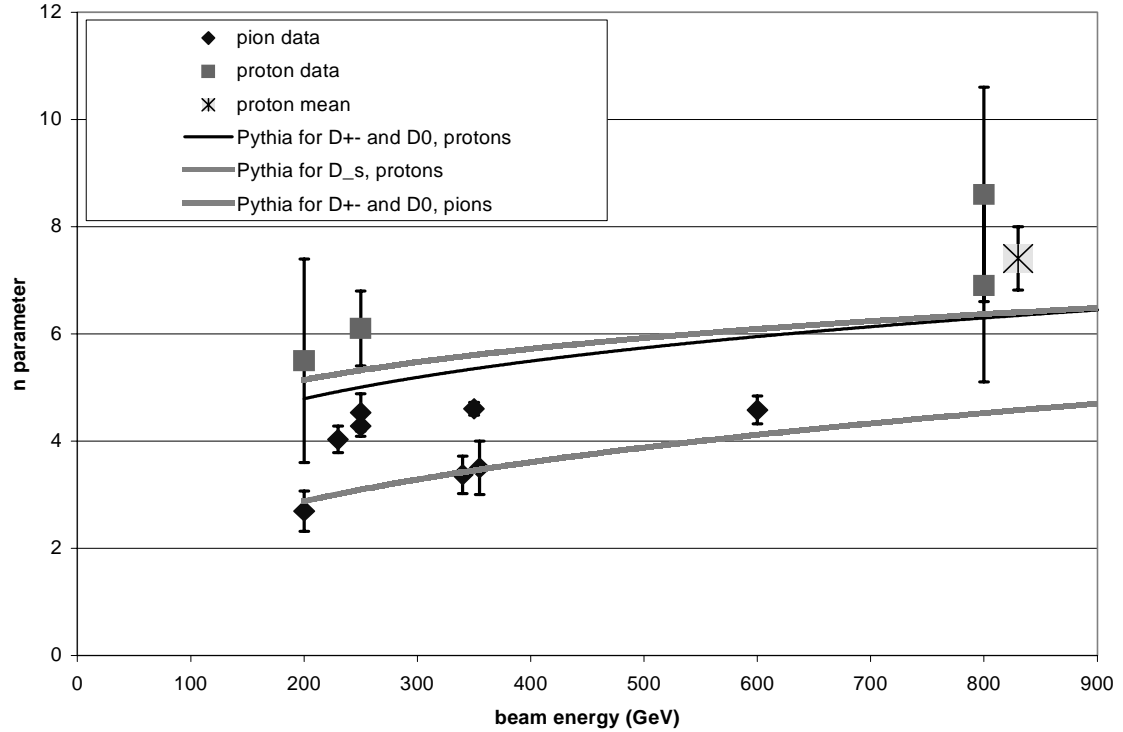


Figure A-12. Same as figure A-10. The lines show results for a Pythia calculation. The solid line shows the Pythia result for D^{++} and D^0 production. The long dashes are for D_s production. The short dashes give the result for a pion beam. The proton mean is explained in the text. The pion data points have been corrected for different fit intervals in x_F .

The Pythia curves are lower than for c quarks only, and they are slightly lower than the corrected data points in figure A-12, both for pion- and proton beams. Pythia and data agree

very well for b . Also shown in the figures is the difference between D_s and D production for protons, which is small at a beam energy of 800GeV.

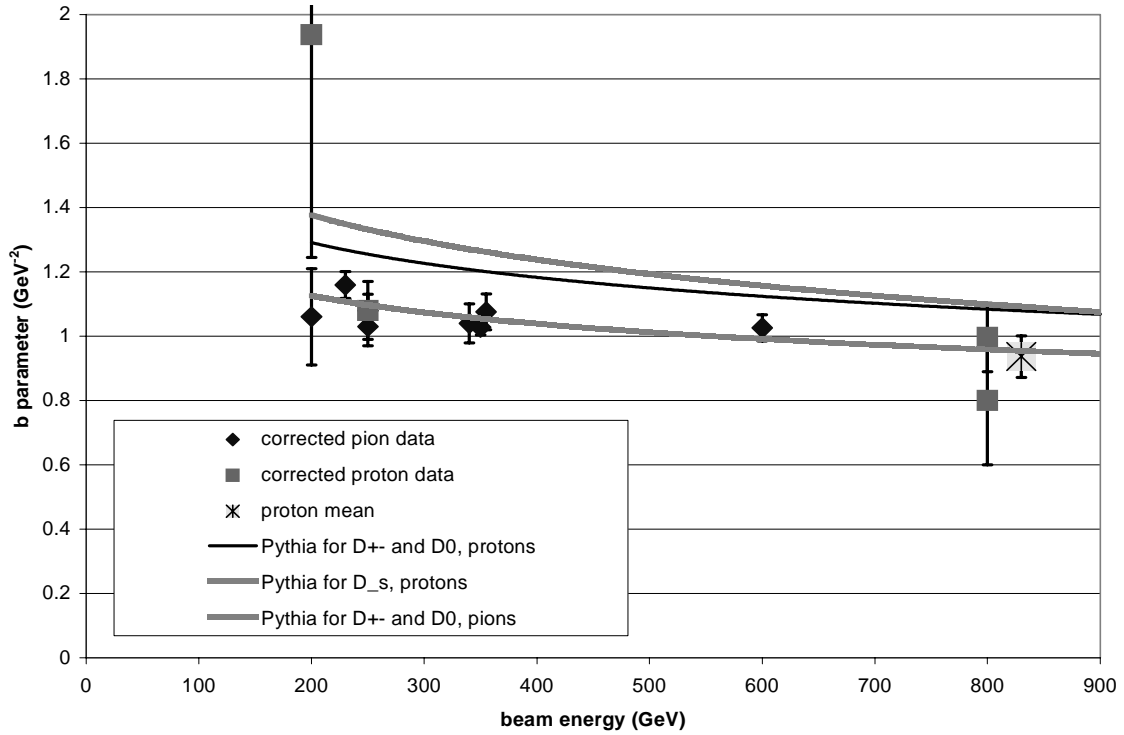


Figure A-13. Same as figure A-12 for the parameter b . The data points have been adjusted for different p_T^2 intervals.

To calculate the parameters for a proton beam at 800GeV, the results from the different experiments are shifted along the Pythia curve for D production in figures A-12 and A-13. Then the average is found by weighting the individual experiments by their measurement uncertainty. The result is shown as proton mean in figures A-12 and A-13. For the pion beam, the same procedure is used, only with the Pythia curve for a pion beam for D production from figures A-12 and A-13.

There are more measurements with a pion beam than a proton beam, and the pion beam measurements agree with the Pythia prediction. One can therefore also use Pythia to predict the parameters for a proton beam from the results from the pion beam. This value is com-

pared to the direct measurement in table A-3. The prediction from pion data to proton data is consistent for both n and b .

beam particle	n	b (GeV ⁻²)
proton	7.4 ± 0.6	0.94 ± 0.06
pion	5.34 ± 0.08	0.929 ± 0.015
proton (from pion)	7.51 ± 0.03	1.033 ± 0.016

Table A-3. Average fit parameters for 800GeV beams. The last row is obtained by multiplying the pion number by the ratio of the Pythia predictions for protons and pions at 800GeV.

The values used in this thesis for D_s production are $n = (7.4 \pm 0.6)$ and $b = (0.94 \pm 0.06)\text{GeV}^{-2}$.

A.5 The D Decay

Although D mesons decay predominantly into kaons and neutrinos, this section will focus only on D^{+-} and D^0 decays that contain a neutrino in the final state since they comprise the prompt neutrino beam. Table A-4 lists the D^+ decay modes with a neutrino in the final state.

decay products	branching ratio (%)	comment
$\overline{K}^0 e^+ \nu_e$	6.7 ± 0.9	
$\overline{K}^{*0} (892) e^+ \nu_e$	4.8 ± 0.5	
$\phi e^+ \nu_e$	1.0 ± 1.0	
$\pi^0 e^+ \nu_e$	0.3 ± 0.05	
$\rho e^+ \nu_e$	0.3 ± 0.05	
e^+ anything	17.2 ± 1.9	includes the previous decays
$\overline{K}^0 \mu^+ \nu_\mu$	7.0 ± 2.5	
$\overline{K}^{*0} (892) \mu^+ \nu_\mu$	4.4 ± 0.6	
$\phi \mu^+ \nu_\mu$	1.0 ± 1.0	
$\pi^0 \mu^+ \nu_\mu$	0.3 ± 0.05	

Table A-4. D^+ decay modes that include a neutrino in the final state [14].

decay products	branching ratio (%)	comment
$\rho\mu^+\nu_\mu$	0.3 ± 0.05	
μ^+ anything	16.0 ± 3.0	estimate based on the $c\bar{c} \rightarrow \mu\text{anything}$ BR [14] and the e^+ anything BR

Table A-4. D^+ decay modes that include a neutrino in the final state [14].

Since lepton number is conserved, each decay channel with an electron also produces an electron neutrino. Table A-5 shows the decay modes for D^0 mesons.

decay products	branching ratio (%)	comment
$K^-e^+\nu_e$	3.66 ± 0.18	
$K^-\pi^0e^+\nu_e$	$1.6^{+1.3}_{-0.5}$	
$K^{*-}(892)e^+\nu_e$	2.02 ± 0.33	
e^+ anything	6.75 ± 0.29	includes the previous three decays
$K^-\mu^+\nu_\mu$	3.23 ± 0.17	
$K^{*-}(892)\mu^+\nu_\mu$	2.0 ± 0.4	
$K^-\pi^0\mu^+\nu_\mu$	$1.6^{+1.3}_{-0.5}$	
μ^+ anything	6.6 ± 0.8	includes the previous three decay

Table A-5. D^0 decay modes that include a neutrino in the final state [14].

About 20% of the D mesons decay into electron- or muon-neutrinos.

A.6 The D_s Decay

The D_s leptonic decay is similar to the pion decay in that it is a fundamental process in electroweak theory [12]. The Feynman diagram is shown in figure A-14.

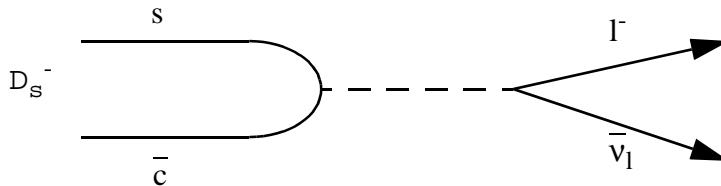


Figure A-14. Feynman diagram for the leptonic D_s decay. l stands for tau, muon, or electron.

The two quarks forming the D_s^- decay to a lepton and the corresponding anti-neutrino. The decay width is given by

$$\Gamma(D_s^- \rightarrow l^- \bar{\nu}_l) = \frac{G_F^2}{8\pi} f_{D_s}^2 m_l^2 M_{D_s} \left(1 - \frac{m_l^2}{M_{D_s}^2}\right) |V_{cs}|^2, \quad (\text{A-7})$$

where G_F is the Fermi coupling constant, f_{D_s} is the decay constant, m_l is the mass of the final state lepton, M_{D_s} is the mass of the D_s^- , and V_{cs} is the CKM matrix element. The numerical values are well known except for the decay constant [14], and the different values for f_{D_s} are shown in table A-6.

experiment (year)	decay channel	f_{D_s} (MeV)	corrections or comments
CLEO (1998) [91]	μ	280 ± 45	none
WA 75 (1993) [92]	μ	238 ± 70	corrected for D^0 and D_s branching ratios (see [91])
BES (1995) [93]	μ/τ	430 ± 160	none
E653 (1996) [94]	μ	280 ± 40	none
L3 (1997) [95]	τ	309 ± 80	from the branching fraction
DELPHI (1997) [96]	τ	330 ± 95	from the branching fraction
mean		285 ± 25	

Table A-6. D_s decay constant measurements.

All measurements agree within their error bars, but the calculation of the mean decay constant is dominated by the high precision measurements of CLEO and E653. Several theoretical predictions have also been done; they include lattice calculations [97] and calculations based on sum rules [98]. They give decay constants between 200MeV and 250MeV with an uncertainty of 50MeV.

The measurements give a decay width for the channel $D_s \rightarrow \tau \nu_\tau$ of $\Gamma = (8.8 \pm 0.7) \times 10^{-11} \text{ MeV}$.

The total decay width of the D_s meson is $\Gamma_{\text{tot}} = (1.41 \pm 0.05) \times 10^{-9} \text{ MeV}$ [14]. The resulting branching fraction for the decay $D_s \rightarrow \tau \nu_\tau$ is therefore $\text{BR}\left(\frac{D_s \rightarrow \tau \nu_\tau}{D_s \rightarrow X}\right) = (6.3 \pm 0.5)\%$.

The leptonic decay to an electron- or muon-neutrino is suppressed by the lepton mass factor in equation A-7. However, there are semileptonic modes that produce neutrinos [14]. The dominant ones are $D_s^+ \rightarrow \phi l^+ \nu_l$ with a branching ratio of $(2.0 \pm 0.5)\%$ and $D_s^+ \rightarrow (\eta \text{ or } \eta') l^+ \nu_l$ with branching ratios of $(2.5 \pm 0.7)\%$ and $(0.9 \pm 0.3)\%$, respectively. Here, l stands for a muon or an electron.

A.7 The Tau Decay

The tau produced in the D_s decay is short lived and it produces another tau neutrino in its weak decay. The modes that also produce electron- and muon neutrinos are listed in table A-7.

decay products	branching ratio (%)
$e^- \bar{\nu}_e \nu_\tau$	17.81 ± 0.07
$\mu^- \bar{\nu}_\mu \nu_\tau$	17.37 ± 0.09

Table A-7. Tau decay modes that include an electron- or muon-neutrino in the final state [14].

The different semileptonic decays leading to a tau neutrino are listed in table A-8.

decay products	branching ratio (%)
$\pi^- \nu_\tau$	11.08 ± 0.13
$K^- \nu_\tau$	0.71 ± 0.05
$\rho^- \nu_\tau$	25.32 ± 0.15
$K^- \pi^0 \nu_\tau$	0.52 ± 0.05
$\pi^- 2\pi^0 \nu_\tau^a$	9.15 ± 0.15
$\pi^- \pi^+ \pi^- \nu_\tau^a$	9.56 ± 0.11
$\pi^- \pi^+ \pi^- \pi^0 \nu_\tau$	4.35 ± 0.10
$\pi^- 3\pi^0 \nu_\tau^a$	1.11 ± 0.14
$K^*(892)^- \nu_\tau$	1.28 ± 0.08

Table A-8. Semileptonic τ branching ratios [14].

a. via $a_1^- \rightarrow 3\pi$ and $\pi^- \omega \rightarrow 3\pi$.

The decay to three pions is dominated by the a_1 resonance and the ω resonance; both of these decay channels are included in this calculation.

A.8 Prompt Neutrino Rates

The total prompt neutrino flux for the different neutrino types is given by the product of D production cross section for the beam and target configuration and the D meson to neutrino branching ratio. The individual contributions have been presented in the preceding sections and the calculation is done in the following steps:

1. The number of open charm particles per proton on target (POT) is calculated from the production cross section and the target dependence. Every proton interacts in the target, which consists of 98% tungsten and 2% iron and has an effective number of nuclei of 181. The total inelastic cross section per nucleon for nuclear targets is $\sigma_{\text{tot}}^{\text{inelastic}} = 37.6 \text{ mb/nucleon}$, see references [81] and [99]. The A dependence is also given in reference [99].

$$N(X)/\text{POT} = \frac{\sigma(X) \times A^\alpha}{\sigma_{\text{tot}} \times A^{0.71}}$$

- a. The number of D^{+-} and D^0 mesons is:

$$N(D^{+-})/\text{POT} = \frac{(11.3 \pm 2.2) \mu\text{B/nucleon} \times 181^1}{37.6 \text{ mB/nucleon} \times 181^{0.71}} = 1.36 \pm 0.25 \times 10^{-3} / \text{POT}$$

$$N(D^0)/\text{POT} = \frac{(27.4 \pm 2.6) \mu\text{B/nucleon} \times 181^1}{37.6 \text{ mB/nucleon} \times 181^{0.71}} = (3.29 \pm 0.34) \times 10^{-3} / \text{POT}$$

- b. The number of D_s mesons is:

$$N(D_s)/\text{POT} = \frac{(5.2 \pm 0.8) \mu\text{B/nucleon} \times 181^1}{37.6 \text{ mB/nucleon} \times 181^{0.71}} = (6.25 \pm 1.06) \times 10^{-4} / \text{POT}$$

2. The number of neutrinos is given by the number of D mesons times the branching ratio to a neutrino final state:

$$N(\nu) = N(D^{+-}) \times \text{BR}(D^{+-} \rightarrow \nu) + N(D^0) \times \text{BR}(D^0 \rightarrow \nu) \\ + N(D_s) \times \{ \text{BR}(D_s \rightarrow \nu) + \text{BR}(D_s \rightarrow \tau) \times \text{BR}(\tau \rightarrow \nu) \}$$

This includes the possibility of a tau decay.

- a. The number of electron neutrinos:

$$N(\nu_e) = (1.36 \pm 0.29) \times 10^{-3} / \text{POT} \times (17.2 \pm 1.9) \% + \\ (3.29 \pm 0.34) \times 10^{-3} / \text{POT} \times (6.75 \pm 0.29) \% + \\ (6.25 \pm 1.06) \times 10^{-4} / \text{POT} \times \{ 0 + (6.3 \pm 0.5) \% \times (17.81 \pm 0.07) \% \} \\ = (4.6 \pm 0.8) \times 10^{-4} \nu_e / \text{POT}$$

b. The number of muon neutrinos:

$$\begin{aligned}
N(\nu_\mu) &= (1.36 \pm 0.29) \times 10^{-3} / \text{POT} \times (16.0 \pm 3.0)\% + \\
&\quad (3.29 \pm 0.34) \times 10^{-3} / \text{POT} \times (6.6 \pm 0.8)\% + \\
&\quad (6.25 \pm 1.06) \times 10^{-4} / \text{POT} \times \{ 0 + (6.3 \pm 0.5)\% \times (17.37 \pm 0.09)\% \} \\
&= (4.4 \pm 1.0) \times 10^{-4} \nu_\mu / \text{POT}
\end{aligned}$$

c. The number of tau neutrinos:

$$\begin{aligned}
N(\nu_\tau) &= (1.36 \pm 0.29) \times 10^{-3} / \text{POT} \times 0 + \\
&\quad (3.29 \pm 0.34) \times 10^{-3} / \text{POT} \times 0 + \\
&\quad (6.25 \pm 1.06) \times 10^{-4} / \text{POT} \times \{ (6.3 \pm 0.5) + (6.3 \pm 0.5) \times 1 \} \\
&= (7.9 \pm 1.3) \times 10^{-5} \nu_\tau / \text{POT}
\end{aligned}$$

The individual uncertainties have been added in quadrature to obtain the final uncertainty. The number of neutrinos does not include neutrinos generated in pion and kaon decays; these form a nonprompt component that will be presented in section A.11. Also, it is assumed that an equal number of neutrinos and anti-neutrinos is produced.

A.9 The Target Acceptance

Only a small fraction of the neutrinos produced in the proton beam target actually pass through the emulsion modules because the most upstream module is located 36.5m downstream of the proton beam target and each module has dimensions of 0.5m by 0.5m perpendicular to the beam.

The Monte Carlo simulation was used to determine the fraction of neutrinos that pass through the target. It depends on the momentum distribution of the produced D mesons found in section A.4 and the result is shown in table A-9.

neutrino type	target acceptance
ν_e	6.8%
ν_μ	6.8%
ν_τ	6.7%

Table A-9. Target acceptance and interacted neutrino energy for the different neutrino types.

The acceptance for ν_τ given in table A-9 is the average over the two neutrinos produced in each D_s decay.

The tau-neutrino flux used in the magnetic moment search is the product of the target acceptance and the total number of tau-neutrinos calculated in appendix A.8. This analysis does not depend on the neutrino-nucleon cross section and the number of expected neutrino-nucleon interactions, which will be discussed in the following sections.

A.10 The Interaction Probability

The number of neutrino-nucleon interactions can be calculated from the neutrino flux and the neutrino-nucleon interaction cross section σ_v^{CC} [12], which is given by

$$\sigma_v^{CC} = \alpha E_\nu K_F \times 10^{-43} \text{ m}^2 / \text{GeV}. \quad (\text{A-8})$$

The cross section is proportional to the neutrino energy E_ν . The factor α takes the difference between neutrinos and anti-neutrinos into account; for neutrinos $\alpha = 6.34$, and for anti-neutrinos $\alpha = 3.15$. The kinematic factor K_F is approximately one for electron- and

muon neutrinos. It depends on the neutrino energy for tau neutrinos; the dependence is shown in figure A-15.

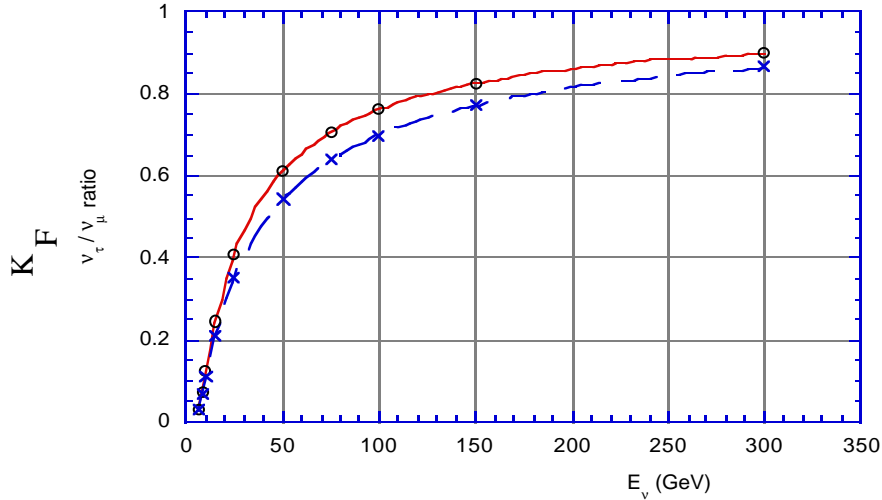


Figure A-15. Energy dependence of the kinematic factor K_F from equation A-8 [100]. The solid line shows K_F for neutrinos; the dashed line shows K_F for anti-neutrinos.

The figure was created in a calculation of the integrated cross section [100]. The kinematic factor is zero at neutrino energies smaller than the tau neutrino mass because these neutrinos cannot interact in a charged current interaction. It increases with increasing neutrino energy and approaches one at energies larger than 400GeV. The average factor for the neutrino energy spectrum calculated above and weighted by the interacted cross section is $K_F = 0.666 \pm 0.005$.

The number of neutrino-nucleon interactions for each kg of target material and for each proton on target (POT) is shown in table A-10.

neutrino type	number of neutrinos/POT/m ²	interacted neutrino energy	average charged current cross section	number of interactions/kg/POT
ν_e	$(1.26 \pm 0.2) \times 10^{-4}$	88.5	$4.9 \times 10^{-41} \text{ m}^2$	$(3.7 \pm 0.7) \times 10^{-18}$
ν_μ	$(1.20 \pm 0.3) \times 10^{-4}$	85.7	$4.8 \times 10^{-41} \text{ m}^2$	$(3.4 \pm 0.8) \times 10^{-18}$
ν_τ	$(2.11 \pm 0.4) \times 10^{-5}$	111.8	$4.1 \times 10^{-41} \text{ m}^2$	$(5.2 \pm 0.8) \times 10^{-19}$

Table A-10. Number of charged current neutrino interactions from prompt neutrinos. The average neutrino energy is weighted by the energy.

The table also shows the average interacted neutrino energy, weighted by the neutrino-nucleon interaction cross section. This average charged current cross section includes equal parts of neutrinos and anti-neutrinos and is corrected for the kinematic factor K_F .

The energy spectrum of neutrinos that interact in the emulsion targets is shown in figure A-16 for all three neutrino flavors. About 10% of the interacting prompt neutrinos are ν_τ .

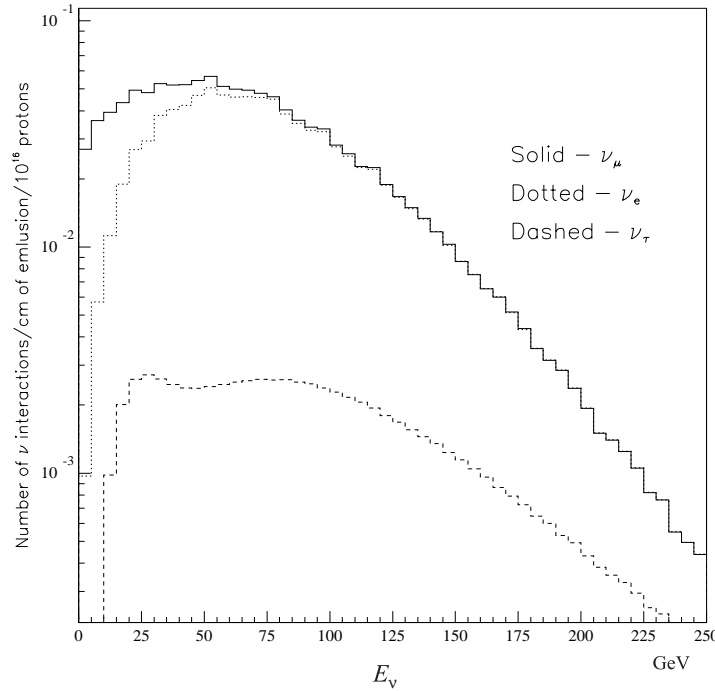


Figure A-16. Interacted prompt neutrino spectrum.

A.11 Other Sources of Neutrinos

Charmed mesons are not the only short-lived particles and not all of the pions and kaons decay before they interact, providing additional sources of neutrinos.

Other Sources of Prompt Neutrinos

Particles heavier than D mesons are also produced in the proton beam target, and some of them decay to neutrinos. Mesons containing the bottom quark, for example, can decay to

neutrinos or D mesons [14]. However, the production of prompt neutrinos other than through D meson decays adds less than 10% to the total number of prompt neutrinos [74]. Secondary interactions of the particles produced in the proton beam target also produce more prompt neutrinos. The average energy of these secondary particles is smaller than the energy of the proton beam and consequently, the average energy of the D mesons and the average neutrino energy is also smaller. The number of neutrino interactions increases by 7.5% as found in a FRITIOF [101] Monte Carlo simulation [49].

These contributions increase the total number of prompt neutrino interactions from table A-10 by 10%.

Nonprompt Neutrinos

Some of the pions and kaons produced in the interaction of protons and nuclei decay to muons and muon neutrinos before they interact in the proton beam target. The fraction of particles that decay depends on the target material. This process has been studied in detail, and the nonprompt neutrino production cross section was determined in a Monte Carlo study [36]. Pion and Kaon decays produce only muon neutrinos because the tau lepton is too heavy to be produced in such a decay and the electron neutrino production is suppressed because the electron is much lighter than the muon [12].

The number of nonprompt muon neutrino interactions was obtained by comparing the muon production rates from the full-density target and the half-density target [100]; the estimated number of neutrino interactions is $(1.3 \pm 0.2) \times 10^{-18}$ interactions/kg/POT.

A.12 The Expected Number of Interactions

The number of neutrino-nucleon interactions is the product of cross section (equation A-8), average neutrino energy (table A-10), target weight, and number of protons on target (POT)

shown in table 4-1. The resulting number of neutrino interactions for all target configurations is shown in tables A-11 through A-15.

period	1	2	3	4
module 0	58.2	47.4	111.0	167.0
module 1	20.0	16.3	38.2	39.2
module 2			25.6	38.5
module 3	20.0	16.3	25.0	37.6
module 4		10.5	24.5	32.1
all modules	98.2	90.5	224.2	314.3

Table A-11. Number of expected prompt electron-neutrino charged-current interactions.

period	1	2	3	4
station 0	53.7	43.8	102.5	154.2
station 1	22.1	15.1	35.3	36.2
station 2			23.6	35.5
station 3	18.5	15.1	23.1	34.7
station 4		9.7	22.6	29.6
all stations	90.7	83.6	207.0	290.3

Table A-12. Number of expected prompt muon-neutrino charged-current interactions.

period	1	2	3	4
station 0	8.2	6.7	15.6	23.5
station 1	2.8	2.3	5.4	5.5
station 2			3.6	5.4
station 3	2.8	2.3	3.5	5.3
station 4		1.5	3.5	4.5
all stations	13.8	12.8	31.6	44.3

Table A-13. Number of expected prompt tau-neutrino charged-current interactions.

period	1	2	3	4
station 0	20.5	16.7	39.1	58.8
station 1	7.1	5.7	13.5	13.8
station 2			9.0	13.6
station 3	7.1	5.7	8.8	13.2
station 4		3.7	8.6	11.1
all stations	34.6	31.9	79.0	110.7

Table A-14. Number of expected nonprompt muon-neutrino charged-current interactions.

period	1	2	3	4
station 0	40.0	32.6	76.4	114.9
station 1	13.8	11.2	26.3	27.0
station 2			17.6	26.5
station 3	13.8	11.2	17.2	25.9
station 4		7.2	16.9	22.1
all stations	67.6	62.3	154.3	216.3

Table A-15. Number of expected neutral-current neutrino interactions.

An estimated total of 2351 neutrino interactions occurred in the target, about half of them in the emulsion.

A.13 Neutrino-Flux Check

Two different data samples were used to compare the calculated number of neutrino-nucleon interactions to the data.

The number of events selected for the neutrino interaction sample from the data is consistent with the calculated number of Monte Carlo events. Figure A-17 shows a comparison by emulsion module type (see section 3.2).

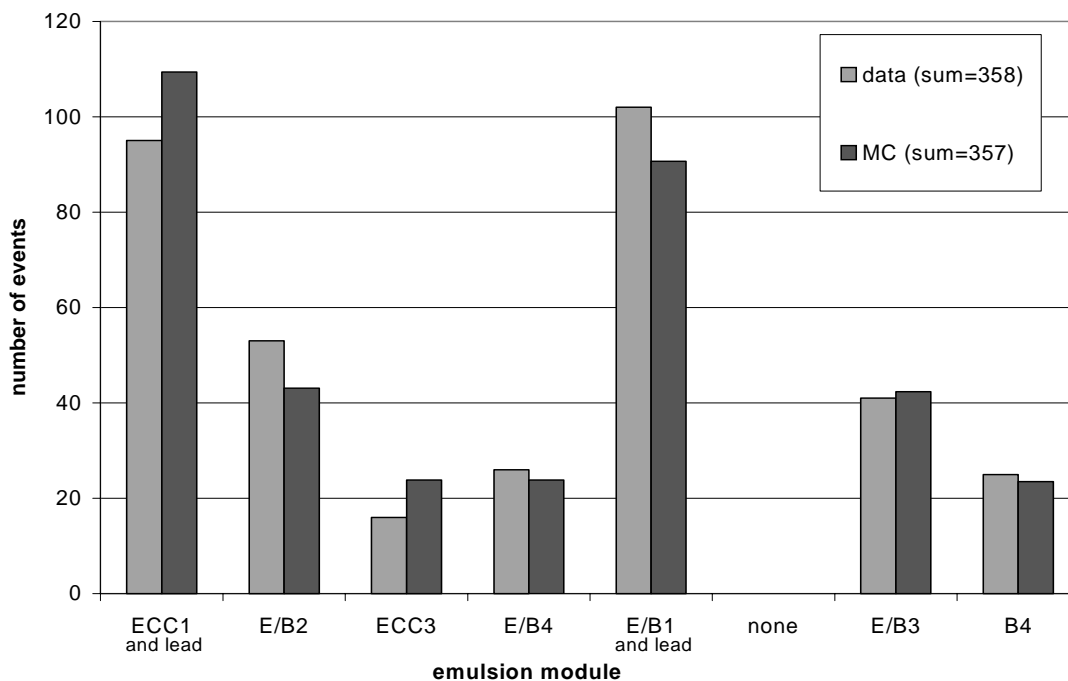


Figure A-17. Number of neutrino interaction events with a muon identified in the muon ID. Comparison of data and Monte Carlo.

The simulation reproduced the number of events observed in the data within the statistical uncertainty.

The second cross-check sample consisted of events with a large signal in the calorimeter. Two cuts have been applied to the data: At first, events that had a signal of more than 5GeV in the calorimeter and more than 2GeV in the central region of small blocks were selected. The calorimeter was most reliable in period four, and for that period, 159 events have been selected in the data. Applied to Monte Carlo events, the cut selected 186.4 events. The uncertainty in the energy calibration is about 20% at a signal of 5GeV [44], and within this uncertainty MC and data give the same result.

The second cut required more than 20GeV in the calorimeter and more than 5GeV in the central region. This cut selected 80 events in the data and 87.2 in the Monte Carlo. The

uncertainty in the calibration of the calorimeter response is smaller at larger energies, and data and Monte Carlo again agree within statistical uncertainty.

Appendix B The Control Events

The Monte Carlo simulation was designed to generate neutrino interactions that mirrored the data, to reproduce the energy spectrum and momentum distribution of the particles produced in these interactions, and to mirror the detector response to charged particle hits. However, the Monte Carlo simulated neither non-neutrino background events nor background tracks in neutrino events. Both of these situations occurred in the data, and the results (cut parameters, selection efficiencies) obtained in the analysis of Monte Carlo events were therefore not directly applicable to data events.

The calibration between data and Monte Carlo events was achieved by analyzing control events that could be simply and unambiguously selected from the data and the Monte Carlo events. Two sets of these control events were analyzed: Muon neutrino charged current interactions comprise the first set, which was used to ensure that the magnetic moment event selection efficiencies were correct for rejected events. These events were also used to determine the total number of neutrino interactions and the neutrino energy spectrum.

Electromagnetic showers produced in the interactions of high-energy muons with electrons comprise the second set, which was used to ensure that the magnetic moment event selection efficiencies were correct for accepted events.

B.1 The Event samples

The first control sample consisted of neutrino interactions that contained a reconstructed muon. These events could be easily extracted from the data because unlike any background process, they contained a reconstructed and identified muon. The same requirement of a reconstructed muon was also applied to the Monte Carlo generated neutrino-nucleon inter-

action sample, providing a sample of Monte Carlo events that should be equivalent to the sample selected from the data.

The second control sample of knock-on electrons that were extracted from the muon calibration runs. The Monte Carlo did not generate these electromagnetic showers, but since the electron-energy spectrum is similar to the spectrum in magnetic moment interactions, the knock-on electron sample was compared directly to the Monte Carlo magnetic moment sample.

Muon Neutrino Charged Current Interactions

Muon neutrino charged current interactions made up about one third of the neutrino interaction data set. They were extracted from the data with high efficiency because the muon was easily identified with the following cuts:

- There had to be one and only one muon identified in the muon ID system. Specifically, the event had to have one reconstructed track associated with at least four muon ID hits and no other reconstructed track associated with more than two muon ID hits.
- The reconstructed muon had to have an impact parameter of less than 0.4m to the center of the last emulsion module.
- The reconstructed neutrino interaction vertex had to be less than 0.24m from the center of an emulsion module.
- The event had to pass a visual check in which events with out-of-time muons, events with muons scattering in the shielding or in the magnet steel, and events in which the muon was not reconstructed in the scintillating fiber planes were removed.

Applying these cuts to Monte-Carlo events selected 56% of the muon neutrino charged current interactions and 10% of the neutral current interactions.

Electromagnetic Showers Produced by Muons

The interaction of a muon passing through the emulsion modules with target atoms occasionally produces a knock-on electron. The distribution of these secondary electrons is given by

$$\frac{d^2N}{dTdx} \cong \frac{1}{\beta^2} \frac{const}{T^2}, \quad (B-1)$$

where T is the electron energy, x is the distance traversed by the muon (in g cm^{-2}), β is the speed of the electron, and $const$ is a constant depending on the material [102]. The energy of knock-on electrons drops off as $1/T^2$, which is comparable to magnetic moment interactions, in which the energy of the electrons drops off as $1/T$ (see equation 2-8). The two spectra are not identical but similar enough to compare the two event samples under the various cuts.

Several runs with muons produced upstream of the experimental area were recorded, and each event in these runs corresponded to one or more muons passing through the detector. Events in which a muon produced an electromagnetic shower were identified as follows:

1. It was required that one and only one track was reconstructed in both views of the scintillating fiber system and in the drift chambers and that it was identified as a muon.
2. It was required that the event contained a shower in the scintillating fiber system behind station 4. A shower was characterized by at least two more reconstructed tracks in each view than there were reconstructed muon tracks.
3. It was required that the muon angle was less than 0.2rad with respect to the neutrino direction.

A total of 100000 muon events from periods 1, 3, and 4 were analyzed with this method. There were not enough muon events in period 2 (with the analysis magnet on) to extract electrons.

In period 1, 15000 muon events were analyzed and 17 events with showers were extracted; in period 3, 40000 events were analyzed and 92 events were extracted; while in period 4,

45000 events were analyzed and 142 events were extracted. A histogram of the measured electromagnetic energy of the selected events is shown in figure B-1.

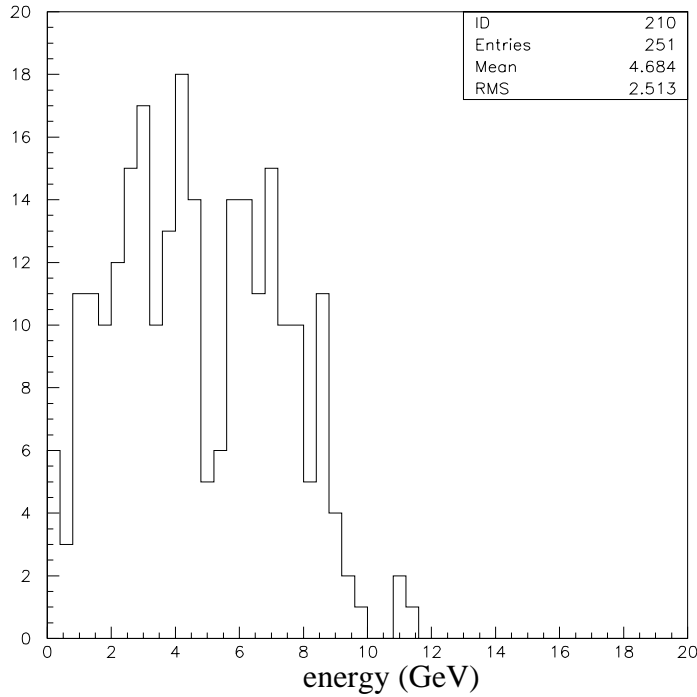


Figure B-1. Histogram of the electromagnetic energy of knock-on electron events selected from muons passing through the spectrometer.

The average measured energy of knock-on electrons was 5GeV, and the functional dependence of $1/T^2$ is not visible due to several factors:

- The selection mechanism removed the lowest energy electrons because they did not produce a shower behind station four.
- The energy measurement has a large uncertainty at small energies.
- Events that occurred in station one or two had a higher average energy than events that occurred in station three or four.

These effects cut off the low energy part of the histogram and smeared out the energy over many bins.

B.2 Comparison between Data and Monte Carlo

The parameters for each of the magnetic moment selection cuts were determined in the analysis of Monte Carlo files. The cut parameters were then adjusted for data files by comparing the effect of each cut on the control samples between data and Monte Carlo. This comparison is shown in figure B-2 for control sample one, neutrino interactions with a reconstructed muon. Each of the cuts was applied to the complete control sample to get the largest statistical significance possible.

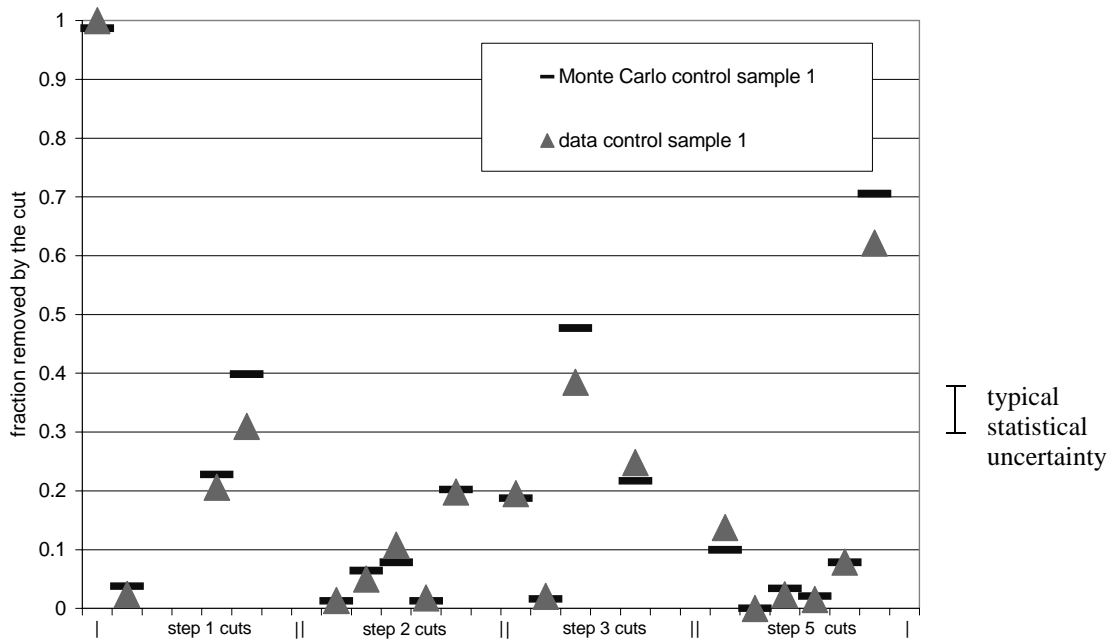


Figure B-2. Plot of the fraction of events removed from control sample one by each of the magnetic moment selection cuts. In the step one cuts, the first point is for the muon identification, the second point for the electromagnetic energy, the third point for vertex tracks, and the fourth point for non-showering tracks. In the step two cuts, the first point is for out-of-time events, the second point for vertex location, the third point for backwards triggers, the fourth point for trigger hits, and the fifth point for slow hadrons. In the step three cuts, the first point is for tracks from the side, the second point is for tracks in one view, the third point is for downstream tracks, and the fourth point is for track angles. In the step five cuts, the first point is for slow hadrons, the second point for shower development, the third point for upstream tracks, the fourth point for single tracks, the fifth point for the shower profile, and the sixth point for non-showering tracks. The error bar next to the figure shows the typical statistical uncertainty in the data.

Each of the cuts removed about the same fraction of events from the data and from the Monte Carlo, within statistical uncertainty. The first cut removed almost all of the events because the muon was reconstructed correctly in the muon ID system, and the last cut removed a large fraction also because the muon was reconstructed in the scintillating fibers.

The same plot for the second control sample is shown in figure B-3.

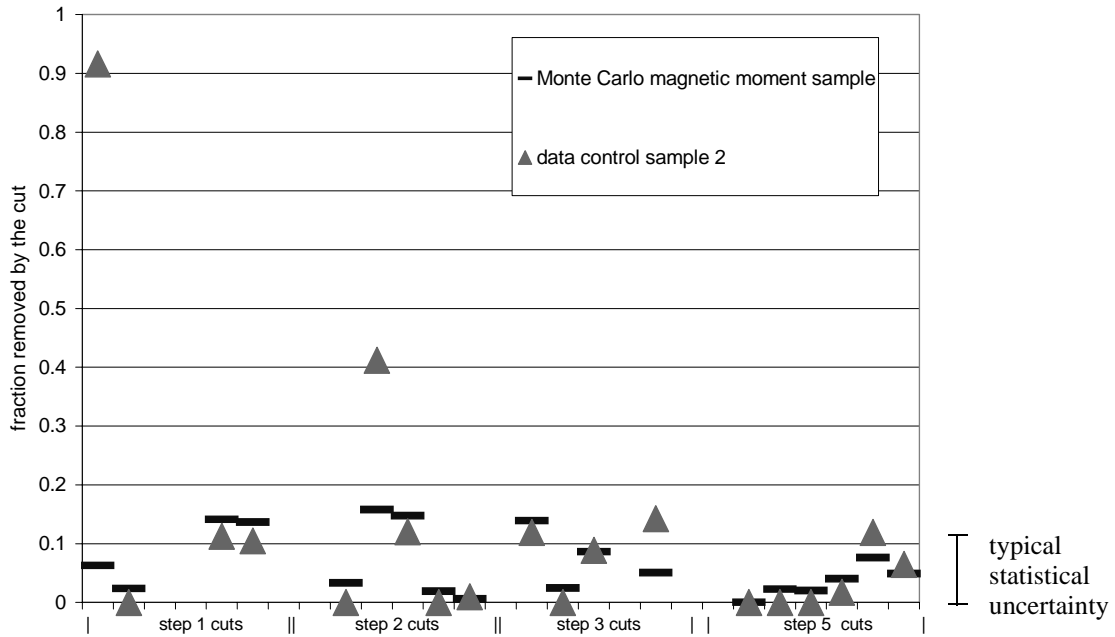


Figure B-3. Same as figure B-2 for the second control sample of electromagnetic showers.

Since there were fewer events in the data sample of electromagnetic showers, the statistical uncertainty is increased. Once again, the selection efficiencies agree between data and Monte Carlo, except for the muon cut which correctly identifies the muon in the data events. Also, the vertex location cut removes a large fraction of the data events. This was expected also since most of the muons pass by the target area on the two sides and the muon flux is smallest at the center of the emulsion modules.

Most of the selection cuts remove less than 10% of the electromagnetic showers in both samples while they remove a larger fraction of events from the neutrino-nucleon interaction samples, which is the desired behavior and demonstrates that the cut parameters were adjusted properly.

Bibliography

- [1] Y. Fukuda *et al.*, the Super-Kamiokande collaboration, Phys.Rev.Lett. **81**: 1562-1567 (1998)
- [2] W. W. M. Allison *et al.*, the Soudan-2 collaboration, Phys. Lett. **B 449**: 137-144 (1999)
- [3] F. Reines, C. L. Cowan, Phys. Rev. **92**: 830-831 (1953) and
C. L. Cowan *et al.*, in Kropp, W.R. (ed.) *et al.: Neutrinos and other matters* 57-58 (1956)
- [4] G. Danby *et al.*, Phys. Rev. Lett. **9**: 36-44 (1962)
- [5] G. J. Feldman *et al.* Mark II collaboration, Phys. Lett. **B 109**: 119 (1982)
- [6] R. Barate *et al.*, Eur. Phys. J. **C 2**: 395-406 (1998)
- [7] S. N. Gninenko, Phys. Lett. **B 452**: 414-417 (1999)
- [8] A. M. Cooper-Sarkar, S. Sarkar, J. Guy, W. Venus, P. O. Hulth and K. Hultqvist
Phys. Lett **B 280**: 153-158 (1992)
- [9] B. Lundberg *et al.*, FERMILAB proposal P-872 (1994)
- [10] S. Weinberg, Phys. Rev. Lett **19**: 1264 (1967)
- [11] A. Salam, in *Elementary Particle Theory*, ed. N. Svartholm (Almquist and Forlag 1968)
- [12] F. Halzen and A. D. Martin, *Quarks and Leptons*, John Wiley & Sons, USA (1984)
- [13] V. B. Berestetskii, E. M. Lifshitz and L. P. Pitaevskii, *Quantum Electrodynamics* (Pergamon 1980)
- [14] C. Caso *et al.*, Particle Data Group, Eur. Phys. J. **C 3** (1998)
- [15] W. Grimus and P. Stockinger, Phys. Rev. **D 57**:1762-1768 (1998)

- [16] The LEP collaboration, Phys. Lett. **B 276**: 243 (1992)
- [17] C. Athanassopoulos *et al.*, the LSND collaboration, Phys. Rev. Lett. **75**: 2650 (1995)
- [18] B. Armbruster *et al.*, the KARMEN collaboration, Nucl. Phys. Proc. Suppl. **38**: 235-239 (1995)
- [19] T.A. Kirsten, Rev. Mod. Phys. **71**: 1213-1232 (1999)
- [20] R. N. Mohapatra and P. B. Pal, *Massive Neutrinos in Physics and Astrophysics* (World Scientific, Singapore, 1991)
- [21] R. N. Mohapatra, hep-ph/9808236 (1998)
- [22] R. Davis, D. S. Harmer, K. C. Hoffman, Phys. Rev. Lett **20**: 1205 (1968)
- [23] J. N. Abdurashitov, *et al.*, the Sage Collaboration, in Proceedings, Fourth International Solar Neutrino Conference, ed. W. Hampel, p 109 (1997)
- [24] M. B. Voloshin, Sov. J. Nucl. Phys. **48**: 512 (1988)
- [25] A. V. Derbin, Phys. Atom. Nucl. **57**: 222-226 (1994)
- [26] D. A. Krakauer *et. al.*, Phys. Lett. **B 252**: 177-180 (1990)
- [27] J. Morgan, Phys. Lett. **102B**, 247 (1981)
- [28] M. Fukugita and S. Yazaki, Phys. Rev. **D36**, 3817-3819 (1987)
- [29] R. Barbieri, R. N. Mohapatra, Phys. Rev. Lett. **61**, 27-30 (1988)
- [30] J.N. Bahcall, M.H. Pinsonneault, S. Basu, J. Cristensen-Dalsgaard, Phys. Rev. Lett.**78**: 171 (1997)
- [31] J. Pulido, Z. Phys. **C70**: 333-338 (1996)

- [32] M. Gell-Mann, P. Ramond, R. Slansky, in *Supergravity*, eds. P. van Nieuwenhuizen and O. Freedman (North-Holland, Amsterdam, 1979) p 317
- [33] G. C. McLaughlin, J. N. Ng, hep-ph/9909558v2 (1999)
- [34] C.-K. Chua, W.-Y.P. Hwang, Phys. Rev. **D 60**: 073002 (1999)
- [35] G. Domogatskii, D. Nadezhin, Sov. J. Nucl. Phys **12**: 678 (1971)
- [36] P. Berghaus, PhD thesis, Kansas State University (2000, *in preparation*)
- [37] M. Skender, Masters thesis, Tufts University (1997)
- [38] J. Sielaff, PhD thesis, University of Minnesota (2000, *in preparation*)
- [39] C. Erickson, PhD thesis, University of Minnesota (2000, *in preparation*)
- [40] FERMILAB E-12 collaboration, Nucl. Instr. Meth. 100:237 (1972)
- [41] KEK-242 experiment, S. Aoki, Nucl. Phys. **A547**: 211c-216c (1992)
- [42] K. Okada, PhD thesis, Nagoya University (2000)
- [43] M.R. Adams *et. al.*, Nucl. Instr. Meth. **A 291**:533 (1990)
- [44] N. Saoulidou, PhD thesis, University of Athens (2000)
- [45] DART Data Aquisition Project, www-dart.fnal.gov and FERMILAB-Conf-94-103 (1994)
- [46] R. Schwienhorst, E872 analysis note AN-011, June 1998
- [47] B. Lundberg, *Visual Scanning with the E872 Event Display*, (<http://fn872.fnal.gov/an/vs/VScan.html>) (1996)
- [48] B. Baller, E872 analysis note *E872 Vertexing Info*, (http://www.hep.umn.edu/~schwier/new/e872/e872code/baller/E872_Vertexing.htm), April 1999

- [49] Byron Lundberg, *private communication* (1996)
- [50] G. Ingelman, J. Rathsmann, A. Edin, *LEPTO - The Lund Monte Carlo for Deep Inelastic Lepton-Nucleon Scattering*, Comp. Phys. Comm. **101**: 108-134 (1997)
- [51] Application Software Group, Computing and Networks Division, *GEANT - Detector Description and Simulation Tool*, CERN Geneva, Switzerland (1998)
- [52] G. Rädcl and R. Beyer, Mod. Phys. Lett. **A8**: 1067-1088 (1993)
- [53] R. Schwienhorst, *The E872 Monte Carlo Version 4*, E872 analysis note from April 9, 1999
- [54] R. Schwienhorst, E872 analysis note from 7 December 1999
- [55] R. Schwienhorst, E872 analysis note from 20 July 1999
- [56] G. Cowan, *Statistical Data Analysis*, Oxford University Press, Oxford, England (1998)
- [57] G. J. Feldman and R. D. Cousins, Phys. Rev. **D 57**, 7: 3873-3889 (1998)
- [58] R. D. Cousins and V. L. Highland, Nucl. Instr. Meth. **A 320**, 331-335 (1992)
- [59] G. D'Agostini, *Bayesian reasoning in High-Energy Physics*, CERN Yellow Report 99-03 (1999)
- [60] MINOS collaboration, FERMILAB-PROPOSAL-P-875 (1995)
- [61] K2K collaboration, KEK-PREPRINT-97-266 (1997)
- [62] ICANOE collaboration, CERN/SPSC 99-25 (1999)
- [63] K. Kodama *et al.*, Phys. Lett. **B 263**: 573-578 (1991)
- [64] K. Kodama *et al.*, Phys. Lett. **B 284**: 461-470 (1992)

- [65] S. Barlag *et al.*, Z. Phys. **C 49**: 555-562 (1991)
- [66] R. Ammar R. *et al.*, Phys. Rev. Lett. **61**, 19: 2185-2188 (1988)
- [67] J. C. Anjos *et al.*, Phys. Rev. Lett. **62**, 5: 513-516 (1989)
- [68] G. A. Alves *et al.*, Phys. Rev. Lett. **77**: 2388-2395 (1996)
- [69] L. Apanasevich *et al.*, Phys. Rev. **D 53**, 3: 1391-1406 (1997)
- [70] M. Adamovich *et al.*, Nucl. Phys. **B 495**: 3-34 (1997)
- [71] D. M. Kaplan *et al.*, Int. J. Mod. Phys. **A 12**: 3827-3836 (1997)
- [72] M. J. Leitch *et al.*, Phys. Rev. Lett. **72**: 2542-2545 (1994)
- [73] T. Akesson *et al.*, Z. Phys. **C 72**: 429-436 (1996)
- [74] M. Mangano, P. Nason, G. Ridolfi, Nucl. Phys. **B 405**: 507 (1993)
- [75] S. Frixione, M. L. Mangano, P. Nason and G. Ridolfi, in *Heavy Flavours II*, eds. Buras A. J., World Scientific Publishing Co., Singapore (1998)
- [76] D. Bortoletto *et al.*, Phys. Rev. **D 37**, 7: 1719-1743 (1988)
- [77] P. Avery *et al.*, Phys. Lett. **B 331**: 236-244 (1994)
- [78] V. Abramov *et al.*, Fermilab-PUB-91-62-E (1991)
- [79] E. M. Aitala *et al.*, Phys. Lett. **B 371**: 157 (1996)
- [80] G. Ambrosini *et al.* submitted to Phys. Lett. **B**, CERN-EP-98-018 (1998)
- [81] S. Fredriksson *et al.*, Phys. Rep. **144**: 187-320 (1987)
- [82] G. A. Alves *et al.*, Phys. Rev. Lett. **70**: 722-725 (1993)

- [83] M. Adamovich *et al.*, Phys. Lett. **B 284**: 453-456 (1992)
- [84] H.-U. Bengtsson and T. Sjöstrand, Comp. Phys. Comm. **46**: 43 (1987)
- [85] T. Sjöstrand and H.-U. Bengtsson, Comp. Phys. Comm. **43**: 367 (1987)
- [86] T. Sjöstrand, Comp. Phys. Comm. **39** 347 (1986)
- [87] G. A. Alves *et al.*, Phys. Rev. Lett. **69**: 3147-3150 (1992)
- [88] S. Aoki *et al.*, Prog. Theor. Phys. **87**: 1315-1322 (1992), Erratum *ibid.* **88**: 621 (1992)
- [89] S. Barlag *et al.*, Z. Phys. **C 39**: 451 (1988)
- [90] P. Mangano, P. Nason and G. Ridolfi, Nucl. Phys. **B 373** 295 (1992)
- [91] M. Chada *et al.*, Phys. Rev. **D 58**: 032002 1-10 (1998)
- [92] S. Aoki *et al.*, Prog. Theor. Phys. **89**: 131 (1993)
- [93] J. Z. Bai *et al.*, Phys. Rev. Lett. **74**: 4599 (1995)
- [94] K. Kodama *et al.*, Phys. Lett. **B 382**: 299 (1996)
- [95] M. Acciarri *et al.*, Phys. Lett. **B 396**: 327-337 (1997)
- [96] F. Parodi *et al.*, in HEP'97 Conference Jerusalem, 1997, paper 455
- [97] A. X. El-Khadra *et al.*, Phys. Rev. **D 58**: 014506 (1998)
- [98] S. Narison, QCD'98 Euroconference Montpellier PM-98/36 hep-ph/9811208 (1998)
- [99] W. M. Geist, Nucl. Phys. **A 525**: 149c-164c (1991)
- [100] B. Lundberg, E872 note from January 11, 2000

[101] H. Pi, *FRITIOF - Simulations of interactions between hadrons and nuclei*, Comp. Phys. Comm. **71** 173 (1992)

[102] B. Rossi, *High Energy Particles*, Prentice-Hall, Inc., Englewood Cliffs, NJ, 1952